Carbon Nanomaterials for Energy Storage, Actuators and Environmental Applications

by

Chengwei Wang

A Dissertation Presented in Partial Fulfillment
of the Requirements for the Degree
Doctor of Philosophy

Approved September 2015 by the
Graduate Supervisory Committee:

Candace K. Chan, Chair
Sefaattin Tongay
Qing Hua Wang
Dong Seo

ARIZONA STATE UNIVERSITY

December 2015

ABSTRACT

Carbon nanomaterials have caught tremendous attention in the last few decades due to their unique physical and chemical properties. Tremendous effort has been made to develop new synthesis techniques for carbon nanomaterials and investigate their properties for different applications. In this work, carbon nanospheres (CNSs), carbon foams (CF), and single-walled carbon nanotubes (SWNTs) were studied for various applications, including water treatment, energy storage, actuators, and sensors.

A facile spray pyrolysis synthesis technique was developed to synthesize individual CNSs with specific surface area (SSA) up to 1106 m^2/g. The hollow CNSs showed adsorption of up to 300 mg rhodamine B dye per gram carbon, which is more than 15 times higher than that observed for conventional carbon black. They were also evaluated as adsorbents for removal of arsenate and selenate from water and displayed good binding to both species, outperforming commercial activated carbons for arsenate removal in pH > 8. When evaluated as supercapacitor electrode materials, specific capacitances of up to 112 F/g at a current density of 0.1 A/g were observed. When used as Li-ion battery anode materials, the CNSs achieved a discharge capacity of 270 mAh/g at a current density of 372 mA/g (1C), which is 4-fold higher than that of commercial graphite anode.

Carbon foams were synthesized using direct pyrolysis and had SSA up to 2340 m^2/g. When used as supercapacitor electrode materials, a specific capacitance up to 280 F/g was achieved at current density of 0.1 A/g and remained as high as 207 F/g, even at a high current density of 10 A/g.

A printed walking robot was made from common plastic films and coatings of SWNTs. The solid-state thermal bimorph actuators were multifunctional energy transducers powered by heat, light, or electricity. The actuators were also investigated for photo/thermal detection. Electrochemical actuators based on MnO_2 were also studied for potential underwater applications.

SWNTs were also used to fabricate printable electrodes for trace Cr(VI) detection, which displayed sensitivity up to 500 nA/ppb for Cr(VI). The limit of detection was shown to be as low as 5 ppb. A flow detection system based on CNT/printed electrodes was also demonstrated.

ACKNOWLEDGEMENTS

I would like to thank my advisor, Prof. Michael J. O'Connell, for his instruction, encouragement, and full support. Instead of an advisor, Mike was more like a friend who always wanted to share generously. Mike's enthusiasm and patience never decreased when he taught me knowledge and skills. I really appreciate his encouragement and trust for letting me keep trying new things. I really value the time working with Mike and his friendship during the early stage of my graduate career.

I would also like to thank my advisor, Prof. Candace K. Chan, for her guidance and help during those hard times in the last two years. I really admire Candace's strong will, which also kept encouraging me to move forward. Her excellent writing skills have always done magic to my manuscripts and benefited me a lot in improving my English. I feel very fortunate to have been one of Candace's first Ph.D. students. And as a smart and diligent person, I am sure she will have a great success in her faculty career.

I would like to thank my dissertation committee, Prof. Sefaattin Tongay, Prof. Qing Hua Wang, and Prof. Don Seo, for their valuable suggestions on my research and their generous time for my comprehensive exam and dissertation defense.

I would like to thank the Fulton Schools of Engineering, the Salt Research Project (SRP)/ASU Joint Research Program, and the School for Engineering of Matter, Transport and Energy University Graduate Fellowship for funding support during my Ph.D.

I would like to thank all the collaborators in my research. Thanks to Prof. Kwai S. Chan from Southwest Research institute for his help with the calculation in the printed active origami project. Thanks to Prof. Vilas G. Pol and Dr. Vinodkumar Etacheri from Purdue University for their help with the Li-ion battery test in CNS for Li-ion battery project. I

would also like to thank Prof. Terry L. Alford and Pai Liu for their assistance with ink jet printer and Kelsey M. Keberle for her assistance with laser cutting stencils. I would like to thank Man Li for her work on Se/As removal with CNSs and Ran Zhao for her help with XPS measurement. I would also like to thank Chengchen Guo for his assistance with Raman and TGA measurements.

I gratefully acknowledge the use of facilities within the LeRoy Eyring Center for Solid State Science, the Goldwater Environmental Laboratory at Arizona State University. I would like to thank Karl Weiss, Dr. Jun Wu, David Wright, Timothy Karcher, Kenneth Mossman, Sisouk Phrasavath, Thomas Colella, and Sara Ryan for their help with equipment training and sample tests.

I would like to thank my classmates and group members for their friendship, help, and support. It has been my pleasure to work with my group members: Takayuki Nosaka, Brett Yost, Benjamin Zimmerman, Emily D. Sutton, Eric Kincaid, Katelyn Keberle, Rodrigo Mendez, Sivan Markowitz, Heeman Ham, Jake Graser, Yuan Wang, Sijie Yang, Ting Yang, Qian Cheng, Ran Zhao, Man Li, and Dr. Ying Li. They helped and taught me a lot for my research. I would also like to thank my other ASU classmates: Ruohan Zhang, Chengchen Guo, Shuoxing Jiang, Jie Ding, Shengke Zhang, Evan Chen, Jia Xu, Hongen Xie, Xinhao Zhao, Jing Lu, Desai Zhang, Yuanyu Ma, Minglu Liu, Lei Ying, and Datong Yuchi, who helped me a lot and made my four years in ASU memorable.

Finally, I would like to express my most gratitude to my parents for their endless unconditional love and support. I would also like to thank my sister, Shanyun, for taking care of our parents when I was absent. Special thanks to Tandy for her love and support.

TABLE OF CONTENTS

Page

CHAPTER Page

LIST OF TABLES

Table Page

LIST OF FIGURES

Figure Page

Figure Page

Figure Page

Figure Page

Figure Page

Figure Page

LIST OF PUBLICATIONS

CHAPTER 2

(1) Wang, C.; Wang, Y.; Graser, J.; Zhao, R.; Gao, F.; O'Connell, M. J. Solution-Based Carbohydrate Synthesis of Individual Solid, Hollow, and Porous Carbon Nanospheres Using Spray Pyrolysis. ACS Nano 2013, 7, 11156–11165.

(2) Li, M.; Wang, C.; O'Connell, M. J.; Chan, C. K. Carbon Nanosphere Adsorbents for Removal of Arsenate and Selenate from Water. Environ. Sci. Nano 2015, 2, 245–250.

(3) Etacheri, V.; Wang, C.; O'Connell, M. J.; Chan, C. K.; Pol, V. Porous Carbon Sphere Anodes for Enhanced Lithium-Ion Storage. J. Mater. Chem. A 2015, 3, 9861–9868.

CHAPTER 3

(4) Wang, C.; O'Connell, M. J.; Chan, C. K. Facile One-Pot Synthesis of Highly Porous Carbon Foams for High-Performance Supercapacitors Using Template-Free Direct Pyrolysis. ACS Appl. Mater. Interfaces 2015, 7, 8952–8960.

CHAPTER 4

(5) Wang, C.; Nosaka, T.; Yost, B.; Zimmerman, B.; Sutton, E. D.; Kincaid, E.; Keberle, K.; Iqbal, Q. A.; Mendez, R.; Markowitz, S.; Liu, P.; Alford, T. L.; Chan, C. K.; Chan, K. S.; O'Connell, M. J. Printed Carbon Nanotubes on Polymer Films for Active Origami. Mater. Res. Lett. 2012, 1–6.

1 INTRODUCTION

1.1 Carbon Nanomaterials

Since fullerenes were discovered by Rick Smalley and coworkers in 1985,[1] two more carbon nanomaterials, carbon nanotubes (CNTs) and graphene, have attracted tremendous attention from researchers of many fields in the last three decades. Fig. 1.1 gives us a clear vision regarding the interest in carbon nanomaterials,[2,3] which shows that the article numbers on this topic have increased almost exponentially.

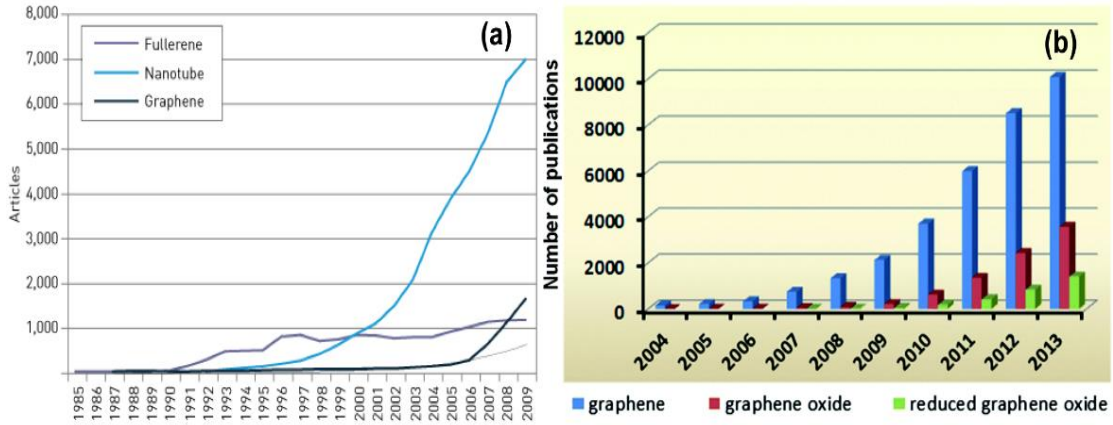

Figure 1.1 Number of articles published in different years about carbon nanomaterials.[2,3]

Moreover, due to their unique optical, electrical, and other properties, carbon nanomaterials have multidisciplinary applications throughout biology, chemistry, physics, materials science, and engineering. The high surface area of carbon nanostructures such as CNTs and graphene have made them attractive for a variety of applications such as electrode materials in supercapacitors,[4–8] fuel cells,[9,10] batteries,[11,12] solar-energy conversion,[13] catalyst supports,[14] sensors[15,16] and adsorbents.[17,18] For example, single-walled carbon nanotube (SWNTs) and single layer graphene have theoretical specific surface areas of 1315 m^2/g and 2630 m^2/g,[19] respectively. However,

in many cases, the effective surface area is much smaller once the carbon nanostructures are deposited onto a substrate due to agglomeration, roping (in the case of nanotubes), or stacking (in the case of graphene). Currently, it is still difficult and expensive to synthesize carbon nanotubes and graphene at large-scales.[20] Hence, there is still a need for the development of low-cost and facile synthesis techniques for carbon nanostructures with highly accessible surface areas. Two promising candidates, carbon nanospheres and carbon foam (porous carbon with foam-like structure) have caught a lot of attention, since they can be synthesized cheaply at large scales and their effective specific surface area (SSA) could easily reach as high as 1000-3000 m^2/g.[21–26] A great deal of effort has been made to develop many approaches for their synthesis. Carbon nanospheres and carbon foam have also been widely used in many fields such as lithium-ion battery electrode materials,[21,27,28] supercapacitors,[22,23,29–32] oil removal,[17,33] catalyst supports,[34,35] and bio-related applications.[36]

Carbon nanospheres are carbon nanoparticles that can be designed with mesoporous or hollow morphologies.[17,26,37,38,39] There are a multitude of different methods for synthesizing carbon nanospheres such as laser ablation,[40] high temperature transformation of nanodiamond,[32,41] arc-discharge in water,[42] combustion synthesis,[43] hydrothermal reaction[44,45] and separation from soot.[46] Mesoporous and hollow carbon nanospheres are often synthesized by using templates such as silica[26,37,38] or polymer nanospheres.[17,39,44,47] Some template-free methods typically result in hollow structures that are interconnected with each other,[28] which are difficult to suspend in solution for bio-applications like drug delivery. Many of the aforementioned methods for

synthesizing carbon nanospheres still suffer from low product yields, which can limit their use in these applications.

Carbon foam can be synthesized in large quantities simply by direct pyrolysis of carbon precursors such as polymers[48–50] or sugars.[21,29,51] Using direct pyrolysis of sugar in the presence of inorganic catalysts, the SSA of carbon foams is usually below 1000 m^2/g.[29,51,52] However, with further activation, the SSA can reach as high as 1500-3000 m^2/g.[21,48,52] For example, Wang *et al.*[29] used the decomposition of ammonium salt to generate gas bubbles, which created a blowing effect on melted sugar to form carbon with a strutted graphene structure and SSA of 1005 m^2/g. However, this reaction needed to be done at a relatively slow heating rate (4 ^oC/min), making it time consuming. By using ZnO nanoparticles as hard template and etchant at high temperature, Strubel *et al.*[21] synthesized porous carbon foam with SSA up to 3060 m^2/g, which demonstrated very impressive performance as an electrode in a lithium-sulfur battery. 3D aperiodic hierarchical porous carbon was also synthesized by carbonization of resin with $Ni(OH)_2$ as catalyst.[25] However, these techniques required multiple steps to synthesize the template or catalyst in advance of the carbon foam synthesis.

Considering the drawbacks in the synthesis techniques mentioned above and the strong demands from the wide applications, large-scale and easier synthesis methods are still needed. In this work, new pyrolysis methods were developed for the large-scale synthesis of both carbon nanospheres and carbon foam with high specific surface area. These porous carbon materials were also studied for several different applications such as dye adsorption, the removal of toxic ions from water, supercapacitors, and lithium-ion batteries. This work will be presented in Chapters 2-3.

Benefitting from their outstanding physical and chemical properties, SWNTs were also studied for applications as actuators and electrochemical sensors in this work. Specifically, SWNT/polymer composite films were used to develop printed active origami (PAO) devices that can be powered by electricity, heat, or light to walk, vibrate, or rotate (Chapter 4). For electrochemical sensors, SWNTs were integrated with multiple substrates and studied for sensitive trace chromium(VI) (Cr(VI)) detection, which will be addressed in Chapter 5. Figure 1.2 summarizes the structure of this dissertation.

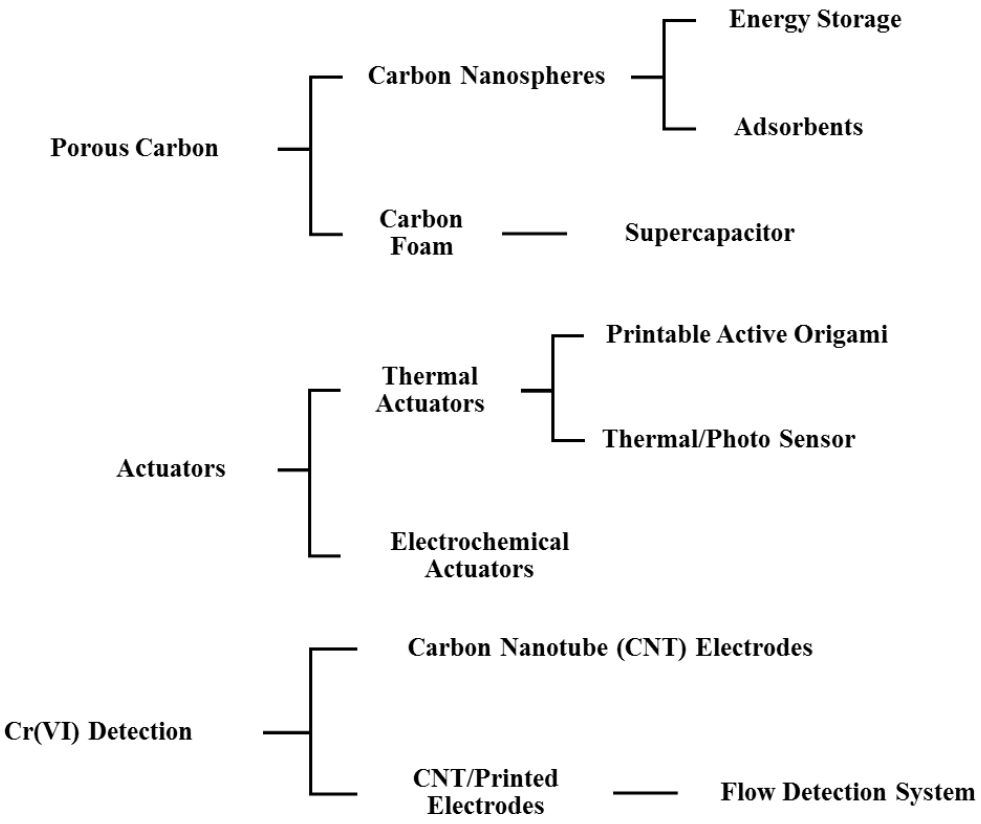

Figure 1.2 Structure of this dissertation.

1.2 Introduction to the Applications

1.2.1 Dye Adsorption

To make products more colorful, dyes have been widely used in many industries, especially textiles, paper, and food. However, as a side-effect, the environmental pollution caused by dyes could cause serious damage to the health of human beings and animals. As the colorful compounds, most dyes have aromatic structures, which are hard to degrade in normal conditions and could be toxic or carcinogenic to human beings.[53,54] Therefore, for environmental and legal reasons, the removal of dyes from wastewater is necessary. Currently, many techniques are developed to treat dye-polluted water. Among these methods, the physical adsorption of dyes with porous materials is low cost and feasibly operational.[54–57] To be used as an absorbent, the high specific surface area (SSA) is a critical property of the material. In this work, high SSA carbon nanospheres were investigated as adsorbents for the removal of rhodamine B from water and compared to commercially available carbon black.

1.2.2 Removal of Arsenate and Selenate

It is well known that arsenic has toxic and carcinogenic properties.[58] Although arsenate (As(V)) is less toxic than arsenite (As(III)), it is the predominant form of arsenic in oxygen rich and oxidizing environments such as drinking and surface waters.[59] While selenium is an essential element, excessive levels can lead to toxicity in humans and wildlife, particularly in aquatic environments where bioaccumulation can be quite rapid. For example, only 2 – 5 ppb of waterborne selenium species can cause reproductive failure in fish.[60] Moreover, compared to the lower oxidation state species, selenate (Se(VI)) is more difficult to remove and there are few effective adsorbents available.

Therefore, in order to remove these harmful contaminants from drinking and industrial waste water, new sorbent materials are greatly needed. As common adsorbents, activated carbons have been widely used for water treatment applications, including the removal of harmful organic compounds[61,62] and metals,[63–65] such as chromium, lead, and mercury. However, the removal of these harmful species normally requires activated carbon containing microporous structure as well as suitable surface functional groups for binding.[66,67] This can be challenging to control due to the wide range of preparation conditions for activated carbon, which can give different structures, porosity, surface chemistry, and surface area.[65] As an easily synthesized and morphology controlled porous carbon nanomaterial, in this work carbon nanospheres were demonstrated as good sorbents for the removal of arsenate (As(V)) and selenate (Se(VI)) with batch adsorption experiments in water spiked with 1 ppm Na_2SeO_4 and 1 ppm $Na_2HAsO_4 \cdot 7H_2O$.

1.2.3 Supercapacitors

Nowadays, with the rapid development of portable electronic devices and electric cars, the demand for high energy and power density energy storage devices becomes stronger and stronger. However, the traditional high energy density storage devices, lithium-ion batteries, suffer from low cycle numbers and long charging times. As a high power density and high cycle number energy storage device, electrochemical supercapacitors have gained more and more attention from researchers. A supercapacitor can charge and discharge in less than 1 second and can also cycle greater than 1 million times, whereas the state of the art for lithium-ion batteries take at least several minutes to charge and discharge and can only cycle around 1000 times.[68]

The traditional capacitors consist of two conducting parallel plates separated by a dielectric layer. Its capacitance can be easily calculated with the equation:

$$C = \frac{\varepsilon \varepsilon_0 A}{d} \quad [1]$$

where ε is the dielectric constant of the dielectric, ε_0 is a constant corresponding to the permittivity of free space (8.85 pF/m), A is the area of each plate, and d is the separation distance between the two plates. When a potential difference, V, is applied between the plates, the amount of charge induced on each plate, Q, can be calculated by:

$$Q = CV \quad [2]$$

After rearranging, the capacitance can be calculated as:

$$C = \frac{Q}{V} = \frac{I}{(V/t)} = \frac{I}{v} \quad [3]$$

Where t is time and v is the scan rate of the voltage.

So, when the capacitor is charged and discharged at a constant current I, the capacitance can be easily calculated from the slope of the discharge voltage curve (Fig. 1.3a). In a cyclic voltammetry measurement, where the voltage is scanned at a constant rate, v, the capacitance can be determined by obtaining the current from the cyclic voltammetry curve (Fig. 1.3b), where the ideal capacitor has a constant capacitance so that the current is constant with potential, while the actual measurement may have deviation from the ideal case. From the galvanostatic voltage profile, a voltage drop due to the inner resistance (IR) of the active materials, electrical contact, and electrolyte can also be observed in the actual measurement.

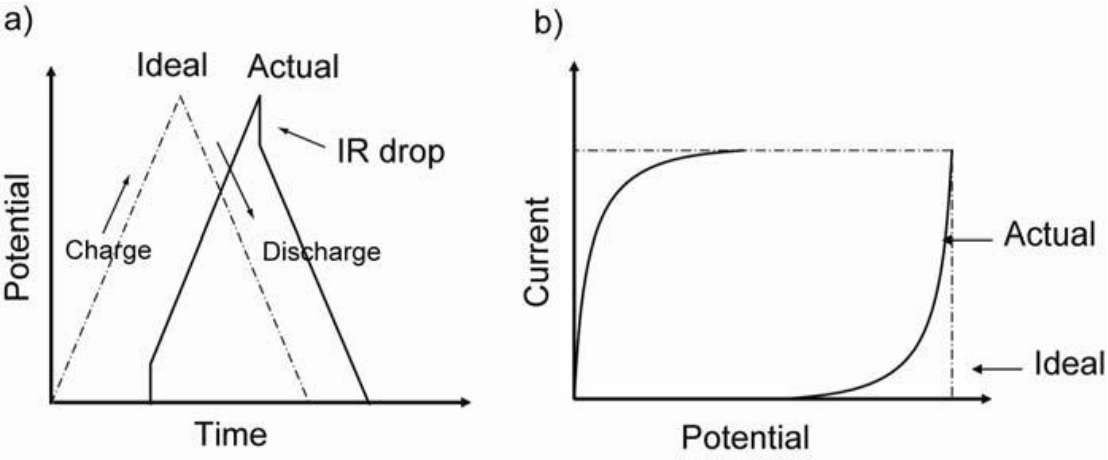

Figure 1.3 Electrochemical characteristics of capacitors. (a) Galvanostatic voltage profile, (b) Cyclic voltammetry.[68]

Due to the limited surface area of the plates, traditional electrostatic capacitors can only achieve from pF to μF of capacitance. The electrochemical double-layer supercapacitors, however, can have capacitance as high as F to kF, since the spacing *d* between the double-layer of the opposite charges forming at the interface between solid electrodes and liquid electrolyte can be small on the order of nm (Fig. 1.4), while the specific surface area of electrodes fabricated from porous materials, like activated carbon black, carbon nanotubes, and graphene, could be on the order of 1000 m^2/g. These unique properties make the supercapacitors have much higher energy density than traditional electrostatic capacitors and much higher power density than batteries.

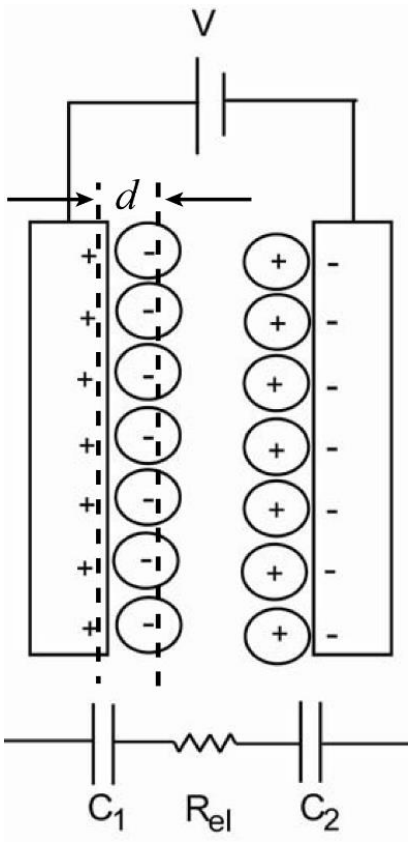

Figure 1.4 Schematic of electrochemical double-layer capacitor and equivalent circuit. Rel is the resistance of the electrolyte.

In this work, a two-electrode configuration[69] in coin cells with 6 M KOH electrolyte was used to measure the performance of the supercapacitors with a BioLogic VMP3 potentiostat from -0.5 V to 0.5 V. The specific capacitance was calculated from the 4 galvanostatic charge-discharge curves with equation:[69]

$$C = 4I/(m\Delta V/\Delta t) \qquad [4]$$

where I is the current used, m is the total mass of carbon nanospheres for both electrodes, and $\Delta V/\Delta t$ was calculated from the slope of the straight part of discharge curve.

1.2.4 Lithium-Ion Batteries

Despite many issues, such as low charge-discharge rate, low cycle times, and safety problems, Li-ion batteries are still the best energy storage devices for portable electronic devices. Just like any other batteries, the Li-ion battery works based on the difference in redox potentials between its two electrodes. As the lightest element having the lowest standard reduction potential (-3.04 V),[68] lithium is one of the best anode materials for high energy density energy storage devices. However, due to dendrite growth during the charge-discharge process, lithium metal electrodes could cause serious safety problems, such as fire and explosion. Fortunately, the layered structure graphite can reversibly intercalate lithium ions without forming any dendrites. During the lithiation process, a maximum of one lithium ion can be stored per every six carbon atoms in between the graphite planes, which gives graphite a theoretical capacity of 372 mAh/g. However, the rate performance for graphite is not very good. Particularly at high charge-discharge rates of 1C (372 mA/g), the charge storage capacity of graphite can drop dramatically. With the increasing demand of portable electronics and electric vehicles, faster charge rates are more and more desired. Therefore, a lot of new anode materials with better capacity and rate performance have been investigated for last two decades. Among the new anode materials, amorphous and turbostratic carbons are promising alternatives for graphite due to their low volume change during lithiation and better rate performance. In this work, the electrochemical properties of porous carbon spheres prepared using a novel spray pyrolysis method[70] were studied for Li-ion storage applications and the materials were found to show very good rate performance.

1.2.5 Actuators

Origami-inspired devices are attractive because a single sheet can be folded into the desired shape, rather than trying to individually fabricate and attach together different components. With the help of geometric folding algorithms and computational tools to determine the folding patterns,[71,72] complex 3-D structures can be realized from 2-D forms,[73] essentially allowing for robots with any form, dimension, and feature to be designed. However, in order to make functional robots, or "active origami", actuation must be engineered into the origami structures.

Of the many different strategies for actuation, the thermal bimorph actuator is attractive. Actuators that operate on electrochemical double-layer capacitance[74,75] require an electrolyte, including ionic electroactive polymers (EAPs)[76] and molecular switches.[77–79] Dielectric elastomers and piezoelectric actuators[80] need high electric fields and voltages. Pneumatically-driven soft robots[81] require the use of compressed gas. A thermal bimorph actuator exploits the differences in thermal expansion coefficients between two materials, as shown in the classical example of a bimetal thermostat.[82] Such electrothermally driven actuation has been demonstrated in microelectromechanical systems (MEMS),[83] carbon nanotube/polymer composites,[84–86] self-folding sheets[87] and has recently been used to impart mobility (e.g. crawling) in a simple worm-like robot through the use of NiTi shape memory springs.[88] However, being able to integrate the actuator with the origami is advantageous from a cost and fabrication perspective, and can also make it easier to produce different robot designs to suit each particular need. To this end, in this work, active origami driven by electrothermal actuation was developed from bilayers comprised of easily obtained carbon nanotube (CNT) materials printed onto common off-the-shelf

plastic. As a potential application, it was demonstrated that a series of inexpensive, all solid-state, printed active origami (PAO) devices can be powered by electricity, heat, or light to walk, open/close, or rotate. The micro scale actuators that based on same materials and mechanism were also demonstrated for photo/thermal detection applications. Using the electrochemical active material, the electrochemical actuators that can be potentially used for underwater applications were also studied and fabricated.

1.2.6 Chromium(VI) Detection

Due to the high toxicity (100-1000 times more toxic than Cr(III)),[89] the detection of trace levels of hexavalent chromium, Cr(VI), has attracted much interest in analytical chemistry. Several sensitive techniques have been developed for the determination of Cr(VI), including spectroscopic[90–93] and electrochemical techniques.[94–97] However, due the influence of Cr(III), which is typically found in much higher concentrations than Cr(VI), the sensitivity and detection limit for Cr(VI) still needs to be improved. Because of the different electrochemical reduction potentials for the different oxidation states of chromium, Cr(VI) can be selectively detected without interference from Cr(III) using electrochemical methods, with also much better sensitivity and detection limits.

For electrochemical detection of Cr(VI), mercury electrodes have demonstrated high sensitivity, but the potential toxicity of mercury electrodes limits their practical application. As another good option, gold has become more and more popular, and gold electrodes have demonstrated to be more electrochemically reversible and stable than carbon electrodes.[89] However, considering the price and fabrication feasibility for gold, carbon electrodes are still of interest due to the lower price and easy assembly.

Recently, Hallam, *et al.*[94] developed graphite screen printed electrodes for the electrochemical detection of Cr(VI). However, the sensitivity was only ~0.8 nA/ppb, while the detection range of 100 to 1000 ppb Cr(VI) with detection limit of 19 ppb, are much less than those of gold electrodes.[95,97]

In this work, a facile printable carbon nanotube (CNT) based electrode was developed. The sensitivity is as high as 100 times that of graphite screen printed electrodes,[94] and even more than twice that of some noble metal electrodes[97], while the detection limit was improved to 5 ppb Cr(VI). Moreover, the electrodes are flexible, enabling them to be integrated inside water tubing or pipes for potential real time monitoring. A flow detection system based on commercial available printed electrodes was also demonstrated to make the detection easier and very promising for practical application.

1.3 Materials Characterization

1.3.1 Electron Microscopy

Due to the shorter wavelength of electrons, the electron microscope has much higher resolution than a light microscope and can be used to characterize the morphology and structure of materials at the nanoscale. When a high energy electron beam interacts with a specimen, many secondary signals are generated, which are used in electron microscopy analysis.[98] The electron microscopes used in this work were scanning electron microscope (SEM) and transmission electron microscope (TEM).

In TEM,[98] the image is created by the high voltage electron beam that produced by the electron gun. After being accelerated by around 200 kV voltage, the electron beam is focused by electrostatic and electromagnetic lenses and then interacts with the sample, during which part of electrons transmits through the sample, while part of them is

scattered back. By magnifying the electrons that transmit through the sample with the objective lens system of the microscope, the images containing information about the structure of the sample can be obtained with a CCD (charge-coupled device) camera. High-resolution transmission electron microscopy (HRTEM) can have a resolution below 1 angstrom, which makes it possible for imaging the lattice fringes of the crystallographic planes of the specimen. In this research, the TEM was used for determining the degree of crystallinity of the carbon after different calcination conditions. The TEM images in this work were obtained with a Philips CM200 operating at 200 kV.

Unlike the TEM, the image in SEM[99] is produced by scanning a focused electron beam across the sample. When the electron beam interacts with the sample, it will lose energy and the sample will emit secondary electrons, back scattered electrons, or radiation like X-rays. By collecting and analyzing the secondary electrons, an image that includes morphology information and a vision of the three-dimension shape of the sample can be generated. Due to the different mechanism with TEM, SEM is able to characterize bulk samples, while TEM requires very thin samples. The SEM images shown in this work were obtained with FEI NOVA 200 Nanolab or FEI XL30 Environmental FEG.

1.3.2 X-Ray Diffraction

Since the wavelength of X-rays has a similar order of magnitude as the spacing between the planes of the crystals, the X-ray wave will be scattered and produce diffraction in specific directions that follow Bragg's law ($2d\sin\theta = n\lambda$), where *d* is the spacing between diffracting planes, θ is the incident angle, n is any integer, and λ is the wavelength of the X-ray beam. Knowing the wavelength of the X-ray (typically Cu Kα-radiation),[100] the crystallographic information of the samples can be deduced by

recording the intensity distribution at different angles. Unlike electron diffraction in TEM which requires ultra-high vacuum, X-ray diffraction (XRD) is usually operated in atmosphere and the samples could be powder or bulk. A PANalytical X'Pert Pro high resolution X-ray diffractometer was used to collect the XRD data in this work.

1.3.3 X-Ray Photoelectron Spectroscopy

X-ray photoelectron spectroscopy (XPS)[101] is a technique used to analyze the elemental composition and their chemical state on the sample surface by photoionizing electrons from the surface with a monochromatic X-ray source. The amount of each element in the sample can also be calculated from the intensity of the binding energy peaks. Since the photoexcited electrons from deeper regions will be trapped or recaptured, only the top 10 nm of the materials can be really sampled. Therefore, XPS is a surface characterization method. The XPS data in this work were obtained with a VG ESCALAB 220i-XL equipped with Al K-α anode X-ray radiation with 1486.6 eV.

1.3.4 Raman Spectroscopy

When monochromatic light is scattered by molecules, the elastically scattered radiation is called Rayleigh scattering, while the inelastically scattered radiation is called Raman scattering, which includes Stokes Raman scattering and anti-Stokes Raman scattering.[102] In Stokes Raman scattering, the scattered photon has less energy than the incident photon. On the contrary, in anti-Stokes Raman scattering the energy of the scattered photon is higher than that of the incident photon. Because they correspond to the energy difference between the same vibrational energy states, the Stokes and anti-Stokes Raman frequency shifts are symmetric around the frequency of the incident photon. Raman spectroscopy can be used to analyze and identify materials like fingerprints, since it highly depends on

the molecular constituents and state. For carbon nanomaterials, Raman spectroscopy is commonly used to identify sp^2 bonds using the G band at ~1588 cm^{-1} and to characterize the defect quality with the D band at around 1350 cm^{-1}.[103–105] In this work, a homemade Raman spectrometer with a 532 nm excitation laser and triple-grating monochromator (SpectraPro 300i, Acton Research) was used. The laser beam was focused with a Mitutoyo M Plan Apo 50x objective lens onto the sample and the measuring power was 10 mW with exposure time of 30 s.

1.3.5 Ultraviolet–Visible Spectroscopy

Ultraviolet–visible spectroscopy (UV-Vis) is absorption or reflection spectroscopy in the ultraviolet-visible spectra region. It measures the electron transition from the ground state to the excited state. According to the Lambert-Beer Law:

$$A = \log_{10}(I_0/I) = \varepsilon CL$$

The technique can be used to quantitatively determine the concentration of the sample in solution, where A is the measured absorbance, I_0 is the intensity of the incident light at a given wavelength, I is the transmitted intensity, L the path length through the sample, and C the concentration of the absorbing species, and ε is a constant known as the extinction coefficient for each species and wavelength. In this work, UV-Vis spectroscopy was used to determine the concentration of dye in water with a StellarNet, BLACK-Comet C-SR-50 spectrometer.

1.3.6 Thermal Gravimetric Analysis

As a thermal analysis method, thermal gravimetric analysis (TGA) can be used to study chemical phenomena like decomposition, solid-gas reaction, chemisorption, and dehydration, *etc.* through measuring the mass change as a function of increasing

temperature. By differentiating the mass loss curve with corresponding temperature, a differential thermogravimetric (DTG) can be obtained to show the rate of mass loss, with the peaks on the DTG curve normally revealing the reaction happening. The basic instruments for TGA are simply a precision balance and a programmable furnace, which makes it very easy to operate and acquire useful data. In this work, a Setaram TG-DTA92 was used to obtain the TGA data, which was used to study the carbothermal reduction of ZnO by carbon at high temperature.

1.3.7 Gas Adsorption-Desorption Isotherms for Surface Area and Porosity Analysis

Gas adsorption-desorption measurements are widely used for studying the surface area and pore size distribution (PSD) of porous materials.[106] The gas adsorption-desorption isotherms could be classified into six types by Union of Pure and Applied Chemistry (IUPAC) in 1985, as Fig. 1.5 shows.[107,108] The type I isotherm is normally observed in microporous solids, where the accessible micropores are occupied at low relative pressure. The type II isotherm changes from concave to convex to the p/p^o axis as the relative pressure increases. It indicates that the adsorption layer changes from a monolayer to multilayer. The Point B, indicating the beginning of the almost linear middle part, is normally considered the completion of the monolayer coverage and the starting of the multilayer adsorption. The type II isotherm is normally obtained in nonporous or macroporous materials. The type III isotherm is always convex to the p/p^o axis over the whole range and has no Point B, which indicates a weak adsorbent-adsorbate interaction. The type III isotherm is not very common. The Type IV isotherm has a hysteresis loop associated with the capillary condensation in mesopores. Other than that, Type IV has the similar initial part with Type II. Like Type III, which is convex to the p/p^o axis initially,

Type V also indicates a weak adsorbent-adsorbate interaction and is very uncommon. The Type VI isotherm is also very rare and has unique step features, which indicate the layer-by-layer adsorption on a non-porous uniform surface.

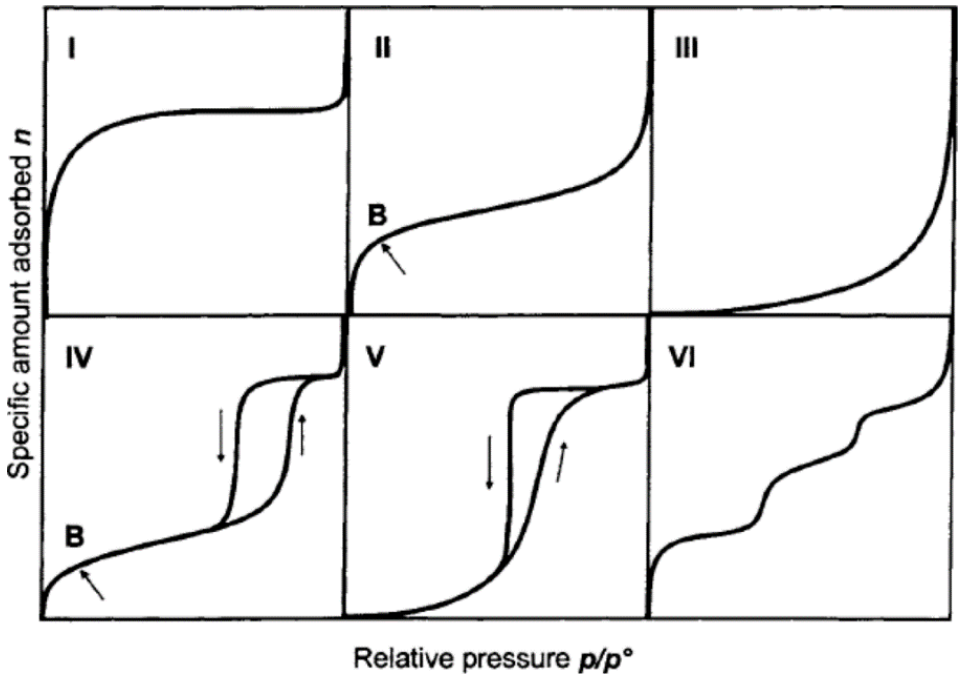

Figure 1.5 Types of physisorption isotherms.[106]

Based on the physisorption isotherms, much information about the material's surface area and pores can be obtained. For the determination of surface area, the Brunauer–Emmett–Teller (BET) surface area analysis technique, one of the most widely used procedures, was first developed by Stephen Brunauer, Paul Hugh Emmett, and Edward Teller in 1938,[109] as an extension of Langmuir theory about molecular adsorption. The measurement is usually conducted at liquid nitrogen temperature, where nitrogen multilayer adsorption is measured as a function of relative pressure. According to the theory, the BET plot is applied only in the linear range of $0.05 < P/P_o < 0.35$ (P and P_o are

the equilibrium and the saturation pressure, respectively, of nitrogen at the temperature of adsorption), where the specific surface area is calculated from the plot.

For pore size distribution, many methods were proposed based on the Kelvin equation, which relates the pore size with the equilibrium vapor pressure. By further introducing a correction cause by the adsorbed film on pore walls, Barrett-Joyner-Halenda (BJH) method[110] was developed for the actual pore size distribution.[111] However, BJH method only works in the mesopore size range. As a more universal method, density functional theory (DFT) was first used to determine the pore size distribution of porous carbon with nitrogen adsorption isotherms by Seaton *et al.* in 1989.[112] Since then, many kinds of calculation methods based on different pore structure models were developed.[113] Since this technique can be used for predicting PSD in different pore geometries over a wide range of pore sizes (micropores to mesopores),[114] it has become more and more popular for the PSD calculation.

In this work, BET, BJH, and DFT were used to study the SSA and PSD changes in porous carbon materials treated with different conditions using nitrogen adsorption isotherms. All of the measurements were conducted with a Micromeritics Tristar II at liquid nitrogen temperature.

2 SYNTHESIS OF POROUS CARBON NANOSPHERES AND THEIR APPLICATIONS

2.1 Introduction to Spray Pyrolysis

Spray pyrolysis has been used for the continuous synthesis of many different types of inorganic nanoparticles[115–117] and can be easily scaled. In this technique, the precursor solution was first atomized with sonicator or air brush, then the mist of the precursor was carried by a carrying gas into the tube furnace and pyrolyzed. Spray pyrolysis was recently applied to the synthesis of carbon nanomaterials. Sohn *et al.*[17] used spray pyrolysis to synthesize graphene capsules, but the method still required the use of polystyrene nanosphere templates. The direct pyrolysis of hydrocarbons[118] has been used to demonstrate the large scale synthesis of carbon spheres. However, this method requires vapor phase or pre-evaporated hydrocarbon solvents and did not demonstrate good particle size control.

Here a solution-based, spray pyrolysis synthesis technique was developed to create individual carbon nanospheres with a high yield and controllable size from precursors consisting of organic carbon precursors and metal salts. The carbon nanosphere diameter distribution was changed by varying the concentration of the precursors. The method also enables the ability to make hollow carbon nanospheres directly without the use of templates by simply adjusting the ratio of precursors. Furthermore, this technique also allows for heteroatom doping of the carbon nanospheres by adding different precursors to the solution. Different metal salts were tested to show the generality for this method and were found to alter the carbon nanosphere structure. Different annealing processes were

used to control the structure and specific surface area (SSA) up to 1106 m^2/g were demonstrated in hollow carbon nanospheres. The dye and toxic ions sorption and electrochemical tests showed that these high surface area carbon nanospheres could be used as materials with high sorption capacity and also for energy storage applications.

2.2 Experimental Details of Spray Pyrolysis and Post Treatment

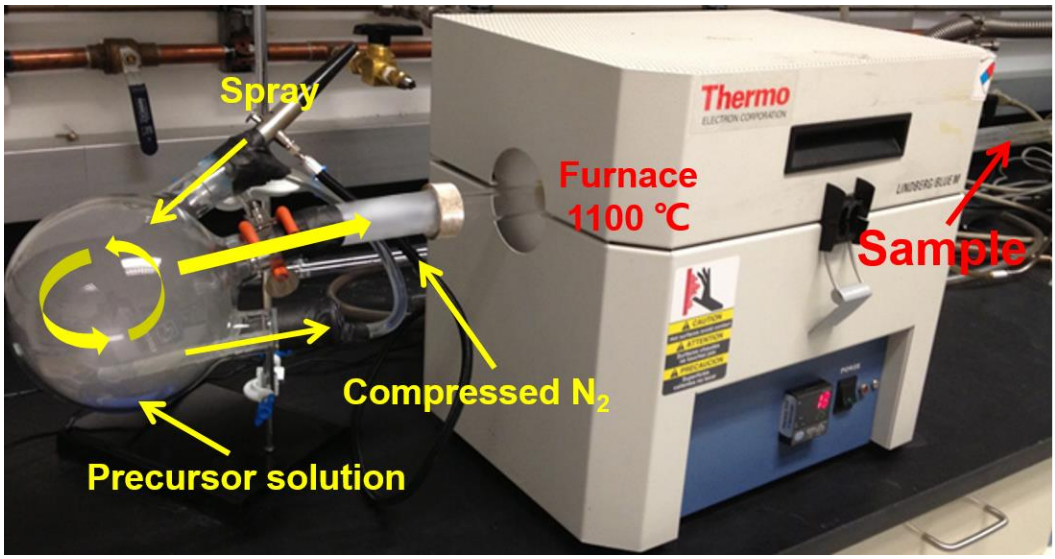

Figure 2.1 Picture of the experimental setup for spray pyrolysis.

The setup for performing spray pyrolysis in a typical experiment is shown in Fig. 2.1. The precursor solutions were prepared by dissolving sugar (sucrose, Alfa Aesar) and $Zn(NO_3)_2.6H_2O$ (Alfa Aesar) in 100 mL de-ionized (DI) water, which was placed in a 250 mL 3-neck round bottom flask. The 3-neck flask was attached to a tube furnace through its middle ground glass joint. An airbrush was fitted to the top ground glass joint such that the nozzle was aimed into the flask to create a swirling mist of the aqueous precursor solution. The swirling mist returned larger droplets to the bottom of the flask to be recirculated and injected smaller droplets into the tube furnace. This gave a rough means to control the droplet size. Nitrogen was used as the carrier gas with a flow rate of

5~8 L/min, while the air brush (Crescendo, Model 175) was adjusted to supply the feedstock at 10~15 mL/h into the tube furnace. In order to increase the residence time of the precursors at high temperature, two 1 inch tube furnaces (Lindberg, HTF55322C and TF55035A-1) were placed in series with a 120 cm long quartz tube connecting the furnaces. The furnaces were heated to 900 and 1000 ^{o}C, respectively. The exit flange was equipped with a 6.35 mm stainless steel tube that was placed into a 250 mL beaker filled with DI water to collect the products. The carbon nanospheres were recovered by vacuum filtration (Millipore FSLP, 0.2 μm filter). Some samples were treated with acid post-synthesis by placing the powders in 1 M HCl and sonicating for 5 min followed by vacuum filtration and washing with DI water. Carbon nanospheres were also synthesized using 3,4-dihydroxybenzaldehyde (Acros), polyethyleneimine (PEI; branched, M_w ~25000, Sigma-Aldrich), manganese (II) nitrate hydrate (Alfa Aesar), ferric chloride (Spectum), and thiourea (Sigma-Aldrich) as precursors. High temperature annealing experiments were performed by heating several tens of milligrams of as-prepared carbon nanospheres at 1000-1200 ^{o}C under N_2 gas flowing at 150 sccm for 0.5-2 h. For some samples, a graphite furnace (GT Thermal Technologies Inc, Model: 1050CG) was used to anneal the samples at 2300 ^{o}C for 1 h in Ar.

2.3 Effect of Precursor Concentration on Particle Size

Typical scanning electron microscopy (SEM) images of carbon nanospheres synthesized from three different concentrations of sugar and $Zn(NO_3)_2$ precursors are shown in Fig. 2.2 (a)-(c). In each case, the sugar to $Zn(NO_3)_2$ weight ratio was maintained at 1:1, corresponding to 0.1 g, 1 g, and 10 g each of sugar and $Zn(NO_3)_2$ in 100 mL DI water, respectively. All of the samples showed a wide particle size

distribution. However, as the concentration of precursors increased, the size distribution was shifted towards larger particle sizes, as shown in the histograms in Fig.2.2 (d)-(f). In the 0.1g:0.1g case, most of the particle sizes were smaller than 100 nm. When the precursor ratio was changed from 1g:1g, the median particle size shifted from ~30 nm to ~70 nm while the largest particle size was still below 1 μm. When the precursor ratio was further increased to 10g:10g, the median particle size increased to ~300 nm, and the largest particle diameter was more than 5 μm. These results show that the carbon nanosphere size distribution can be adjusted by changing the concentration of reagent precursors.

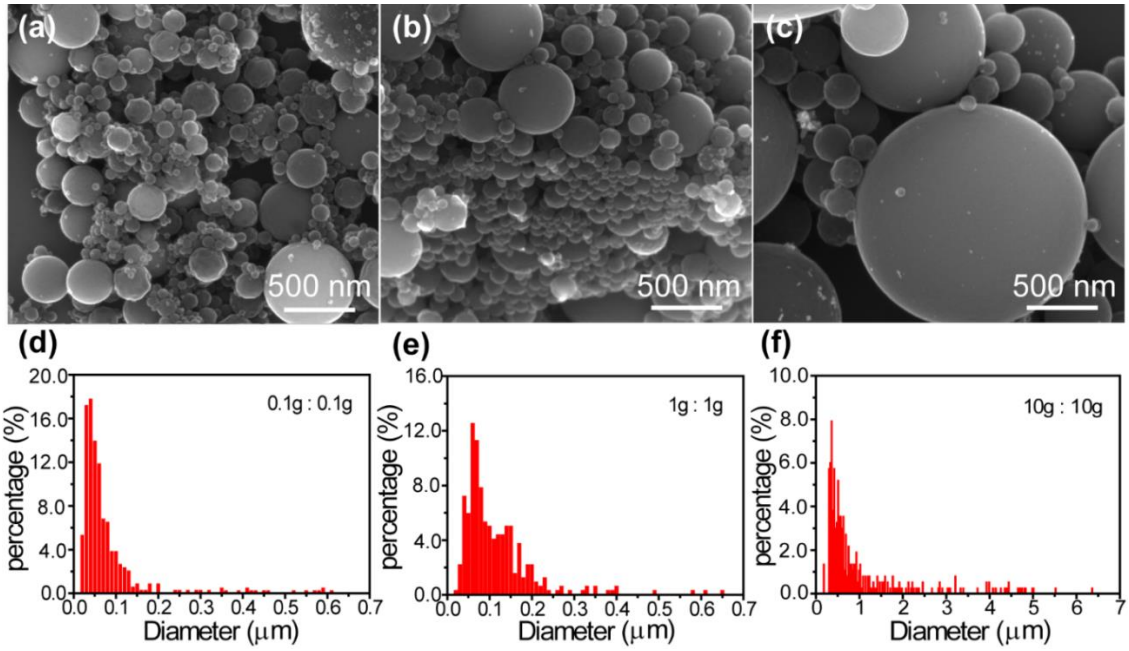

Figure 2.2 SEM image and size distribution of carbon nanospheres synthesized using spray pyrolysis from different ratios of $Zn(NO_3)_2$ to sugar in 100 mL DI water. (a), (d) 0.1g : 0.1g; (b),(e) 1g : 1g; (c),(f) 10g : 10g.

X-ray diffraction (XRD) measurements were performed on carbon nanospheres prepared using a precursor ratio of 1g:1g. As shown in Fig. 2.3a, the as prepared sample only showed a few reflections, which matched to ZnO (PDF 01-079-0208 in the ICDD database). This suggests that the as-prepared carbon nanospheres have an amorphous carbon structure and that the $Zn(NO_3)_2$ transformed to ZnO during the spray pyrolysis. The XRD pattern after HCl etching showed that the ZnO peaks were no longer visible, suggesting that the ZnO was dissolved during the treatment. Annealing the as-made carbon nanospheres in the tube furnace at 1200 ^oC for 1 h under Ar（flowing at 100 sccm) resulted in a featureless XRD pattern, indicating that the carbon remained amorphous. The ZnO peaks were absent as well. Since it is known that ZnO can be reduced by carbon at high temperatures,[119] it is possible that the ZnO nanoparticles were reduced to Zn and then evaporated, since the boiling point of Zn is only 907 ^oC.

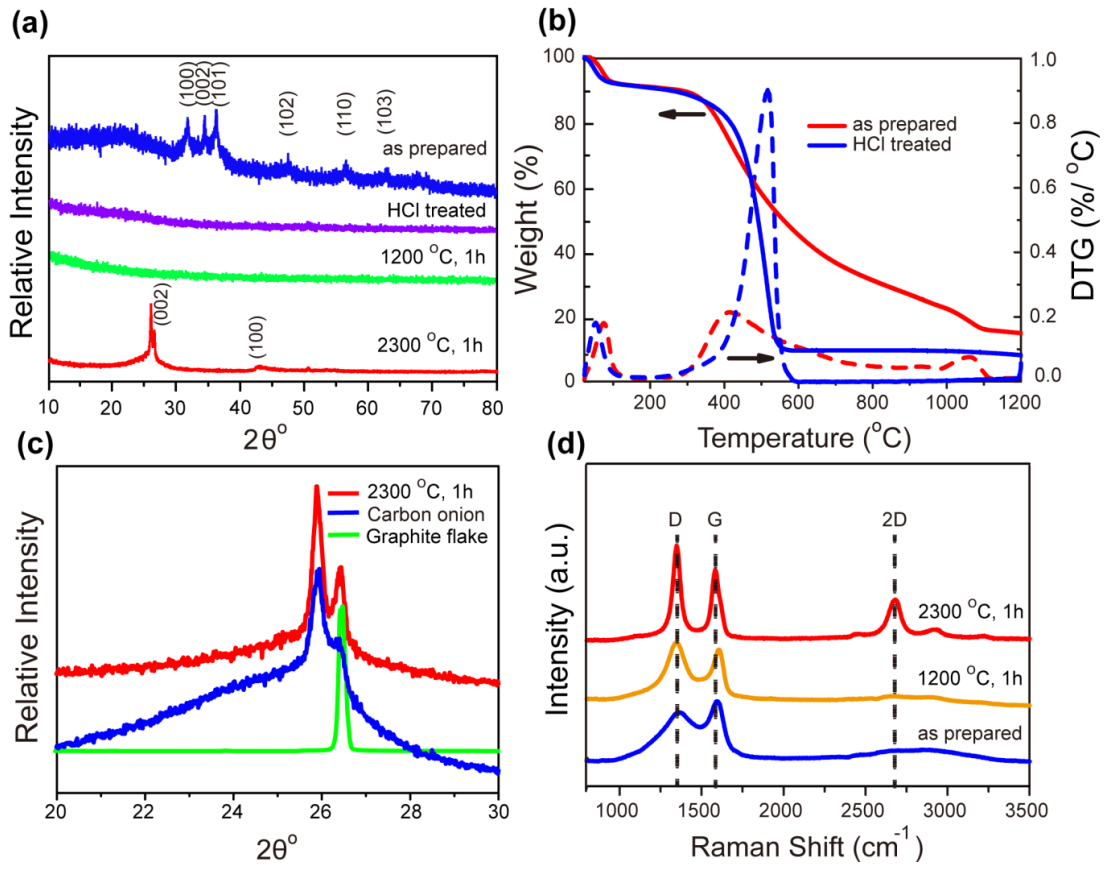

Figure 2.3 Characterization of carbon nanospheres from 1g:1g precursors. (a) XRD results of products as-prepared (blue), after HCl treatment (purple), after annealing as-prepared products at 1200 ℃ for 1 h (green), after annealing as-prepared products at 2300 ℃ for 1 h (red). (b) TGA results for as prepared carbon nanospheres (red) and after HCl treatment (blue). (c) Zoomed-in XRD pattern around the d-spacing for (002) plane of graphite of carbon nanosphere products annealed at 2300 ºC for 1 h (red) compared to carbon onions prepared from nanodiamond annealed at same condition (blue) and graphite flake (green). (d) Raman spectra using 532 nm excitation of carbon nanospheres as prepared (blue) and after annealing at 1200 ºC (orange) and 2300 ºC (red) for 1 h.

To better understand these results, thermogravimetric analysis (TGA) (Fig. 2.3b) was performed on the as-prepared 1g:1g carbon nanospheres (which still contained ZnO nanoparticles) and samples after HCl etching (ZnO removed). The initial weight loss for both samples below 200 ^{o}C was due to desorption of water and air. The carbon nanosphere sample treated with HCl lost the most weight between 400-600 ^{o}C, likely due to further carbonization of the remaining organics. For the as-prepared sample, however, the weight kept decreasing even at 1200 ^{o}C, while the derivative thermogravimetric (DTG) curve showed another weight loss peak at ~1050 ^{o}C, likely due to the evaporation of zinc. Gravimetric measurements performed after annealing ~100 mg of carbon nanosphere sample showed a ~20 wt% weight loss after heating at 700 ^{o}C for 30 min, attributed to the carbonization reactions. After treating the sample with HCl and drying, ~30% of the mass was further lost. This was attributed to the removal of ZnO. Therefore about 50-60% of the original mass remained as pure carbon.

After annealing the as-made samples at 2300 ^{o}C for 1 h, the amorphous carbon nanospheres changed to graphitic structures. This structure change was reflected in the XRD pattern (Fig. 2.3a, c) and confirmed using Raman spectroscopy (Fig. 2.3d). In the XRD pattern, the peak at $2\theta = 43^{o}$ was indexed to the (100) plane for graphite (PDF 00-041-1487). Two peaks were observed very close together at $2\theta = 25.88^{o}$ and 26.45^{o}, with the latter being close to the reflection for the (002) plane of graphite (Fig. 2.3c). This two-peak phenomenon was observed in other literature[120] before but without clear explanation. A peak with the former spacing and a broad shoulder near the (002) plane was observed in carbon onions derived from high temperature annealed nanodiamond.[121] The XRD pattern corresponding to these carbon onions is shown in Fig. 2.3c as

comparison. When overlaying the XRD pattern of the carbon nanosphere sample annealed at 2300 ^{o}C with that for nanodiamond-derived carbon onion, as well as pure natural graphite flake, the relationship of these peaks can be clearly observed. Hence the peak at $2\theta = 25.88^{o}$ likely corresponds to the high curvature graphitic faces similar to those found in carbon onions while the peak at $2\theta = 26.45^{o}$ may come from the low curvature graphitic faces found in graphite. The reason that the (002) peak splits into two peaks in the carbon nanospheres might correspond to different types of nanoscale curvature inside the nanospheres. This was confirmed with high resolution transmission electron microscopy (TEM) on the carbon onions (Fig. 2.4a) and carbon nanospheres (Fig. 2.4b).

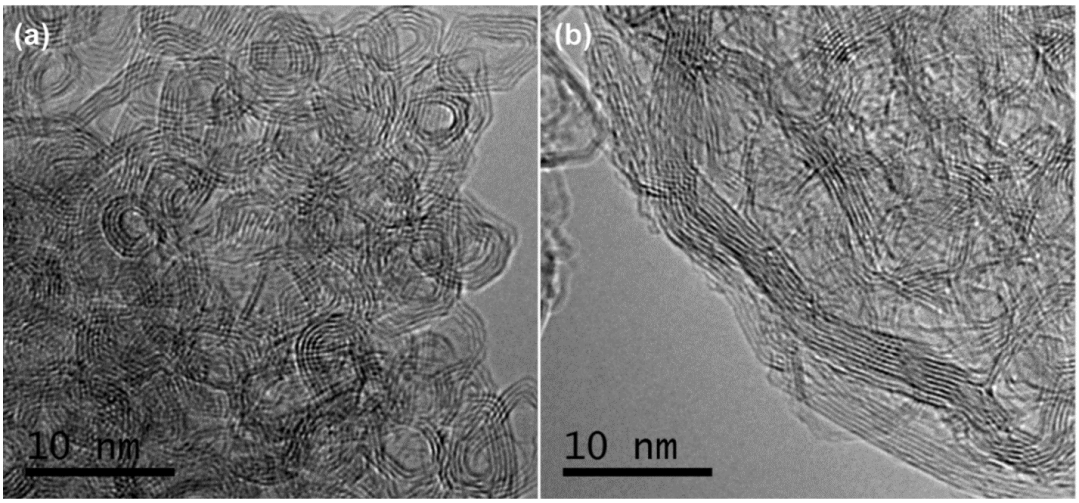

Figure 2.4 HRTEM of (a) nanodiamond-derived carbon onions and (b) carbon nanospheres annealed at same condition, 2300 ^{o}C, 1h.

The Raman spectra of the carbon nanospheres with different heat treatments are shown in Fig. 2.3d. The D band at ~1360 cm^{-1} is attributed to defect and disorder-induced modes of disordered or glassy carbon.[122] The peak at ~1590 cm^{-1} is indexed to the G band

corresponding to the phonon mode with E_{2g} symmetry of graphite.[104] Other than the sample annealed at 2300 ^{o}C for 1 h, none of the samples have the 2D band at ~2680 cm^{-1}, while D and G bands were broad and weak, indicating the presence of significant amounts of disordered carbon. For the sample treated at 2300 ^{o}C, the ratio of the intensities of the 2D and G bands (I_{2D}/I_G) was equal to 0.57, which reflects a multilayer graphene structure. This is consistent with the XRD (Fig. 2.3c) and TEM results (Fig. 2.4b) showing graphitization of the carbon nanospheres after annealing at 2300 ^{o}C.

2.4 The Role of Metal Salt on Carbon Nanospheres Formation and Morphology

In order to study the role of the $Zn(NO_3)_2$ during the formation of the carbon nanospheres, the weight ratio of $Zn(NO_3)_2$ to sugar was varied. In all cases 1 g sugar and 100 mL of DI water were used. Fig. 2.5 shows some typical TEM images of different as-prepared carbon nanospheres using different amounts of $Zn(NO_3)_2$. Fig. 2.6 shows the high-magnification TEM images of individual carbon nanospheres prepared using precursor ratios of 1g:1g, 3g:1g, and 10g:1g. Fig. 2.6a shows the high-magnification TEM image of as-prepared carbon nanospheres using 1g:1g. The particles <10 nm in diameter on the carbon nanosphere surface correspond to ZnO. As shown in the high resolution TEM image in Fig. 2.5b, the ZnO nanoparticles were crystalline, with the measured d-spacing of 0.28 nm matching the ZnO (100) plane while the carbon was amorphous, consistent with the XRD results. Fig. 2.6b shows a high magnification TEM image of carbon nanospheres prepared from a precursor solution with 3 g of $Zn(NO_3)_2$ to 1 g of sugar (3g:1g). Most of the carbon nanospheres appeared to be covered with larger particles about 20 nm in diameter. When the $Zn(NO_3)_2$ to sugar ratio was increased to 10g:1g, the nanoparticles on the surface of the carbon nanospheres also had large

diameters greater than 50 nm (Fig. 2.6c). No carbon nanospheres were made when performing spray pyrolysis of sugar solutions without $Zn(NO_3)_2$, indicating that the ZnO nanoparticles may play an important role as nucleation sites for the carbonization reactions and promote formation of the carbon nanospheres.

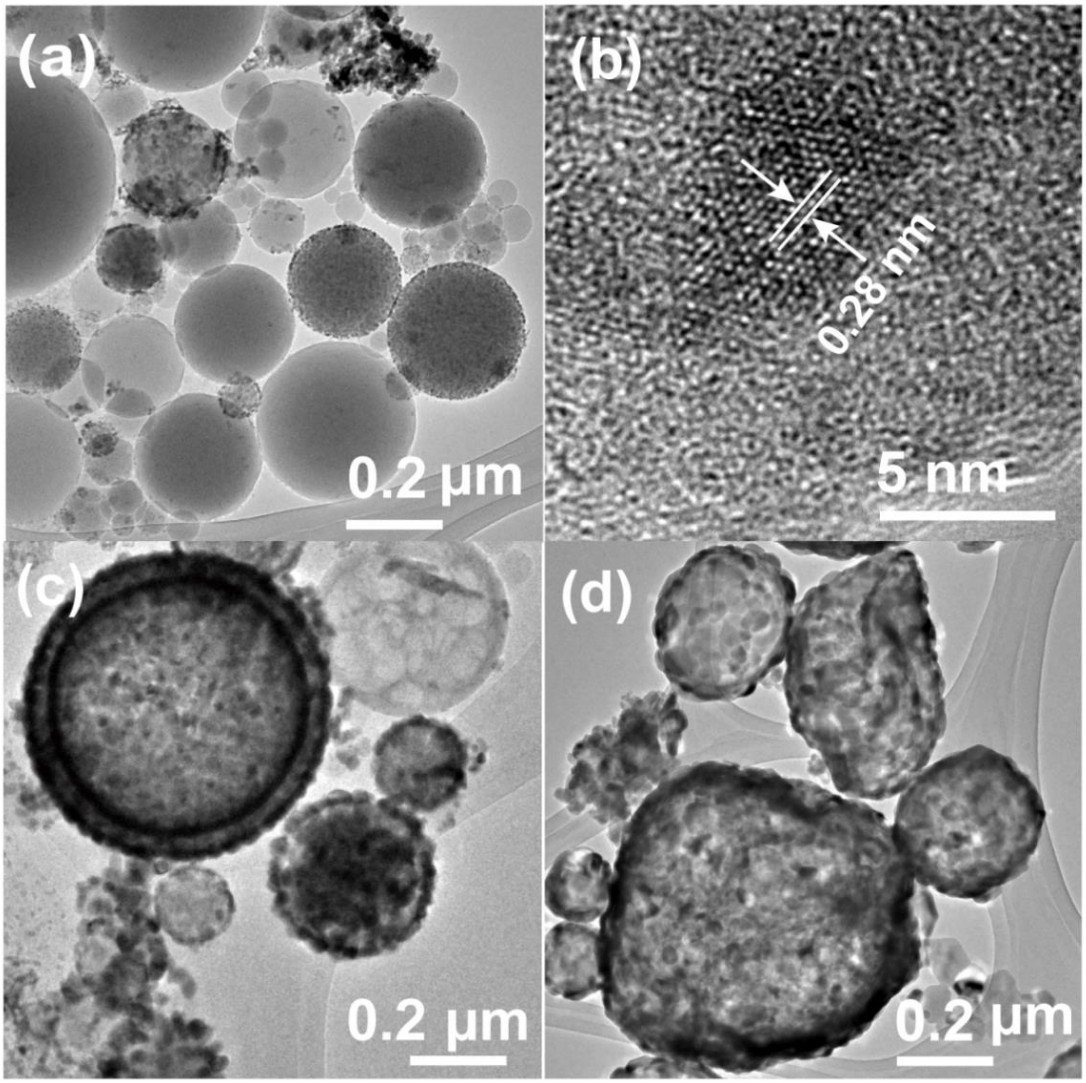

Figure 2.5 TEM images of as-prepared carbon nanospheres synthesized from $Zn(NO_3)_2$ to sugar ratios of (a),(b) 1g: 1g; (c) 3g: 1g; (d) 10g: 1g. (b) HRTEM image of ZnO

nanoparticle inside the carbon nanospheres from 1g:1g sample with d-spacing of 0.28 nm matching ZnO

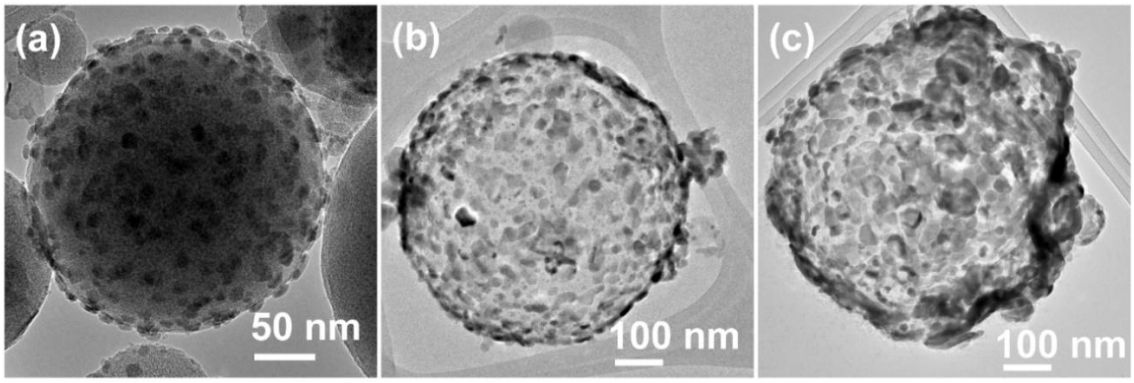

Figure 2.6 TEM images of carbon nanospheres from $Zn(NO_3)_2$ to sugar ratios of (a) 1g : 1g; (b) 3g : 1g; (c) 10g : 1g.

TEM images of carbon nanospheres after HCl treatment are shown in Fig. 2.7 for the different $Zn(NO_3)_2$:sugar ratios. The nanoparticles observed in the as-prepared samples were absent after HCl etching, confirming that they were composed of ZnO (Fig. 2.7a-b). In contrast, the as-prepared samples annealed at 2300 ^oC showed a graphitic structure, consistent with the XRD and Raman results (Fig. 2.3). The ZnO nanoparticles were also absent, confirming the proposed evaporation at the higher annealing temperature, as suggested by the TGA data (Fig. 2.3b). As Fig. 2.6a-b show, the 1g:1g dots are mostly solid. The 3g:1g products after HCl etching (Fig. 2.7d) consisted of some smaller, solid amorphous carbon nanospheres (Fig. 2.7e) while others appeared to be hollow, "balloon"-like nanospheres with highly porous structures (Fig. 2.7f). After HCl treatment of the samples prepared from the 10g:1g precursor solutions, the resulting carbon nanospheres were highly porous (Fig. 2.7g) and large carbon particles with "balloon"

morphology dominated the product (Fig. 2.7i). The smaller carbon nanospheres were also observed to have a highly porous structure (Fig. 2.7h).

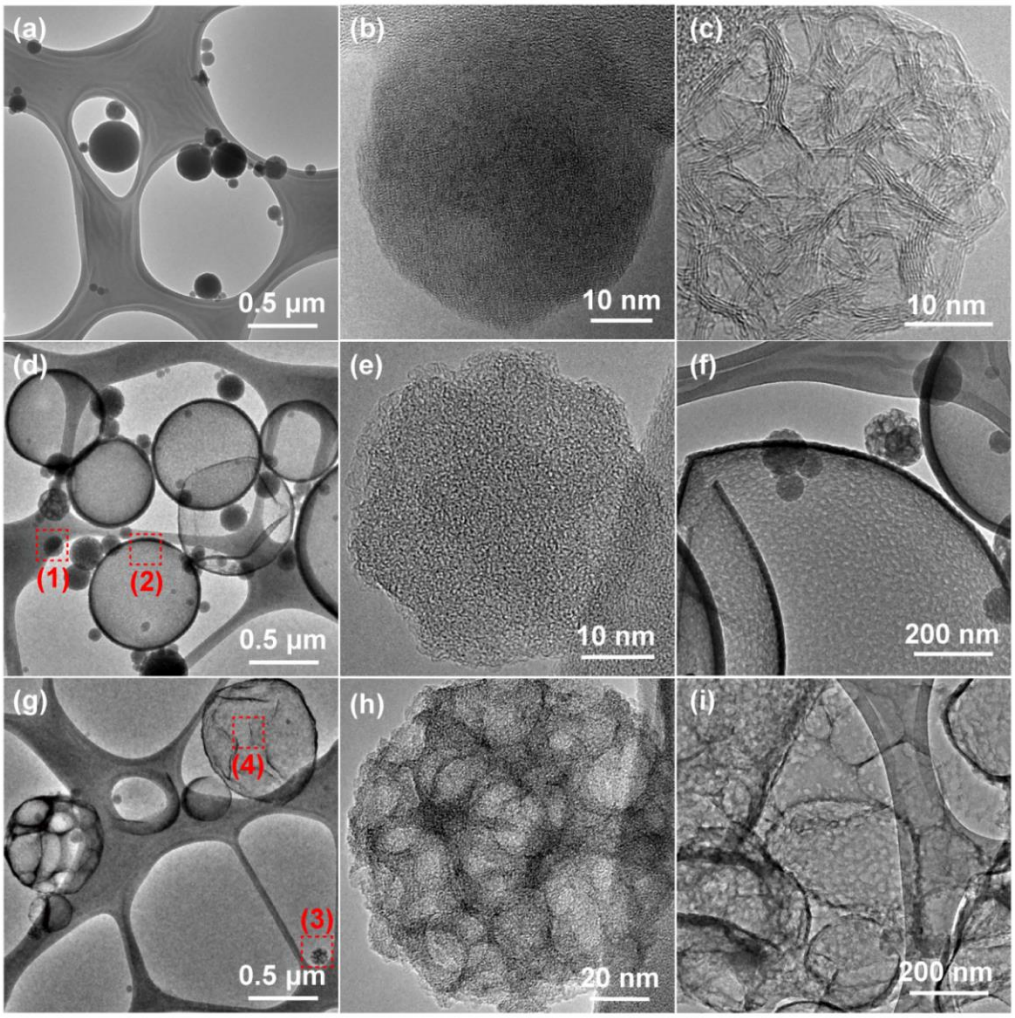

Figure 2.7 TEM images of carbon nanospheres from different $Zn(NO_3)_2$ to sugar ratios after HCl etching. (a)-(c) were prepared using 1g:1g, (a) and (b) are after HCl etching whereas (c) shows the as-prepared product after annealing at 2300 ^{o}C. (d)-(f) are prepared using 3g:1g. (e) and (f) show the zoomed in images of particles (1) and (2) in (d), respectively. (g)-(i) were prepared using 10g:1g. (h) and (i) show the zoomed in images of particles (3) and (4), respectively.

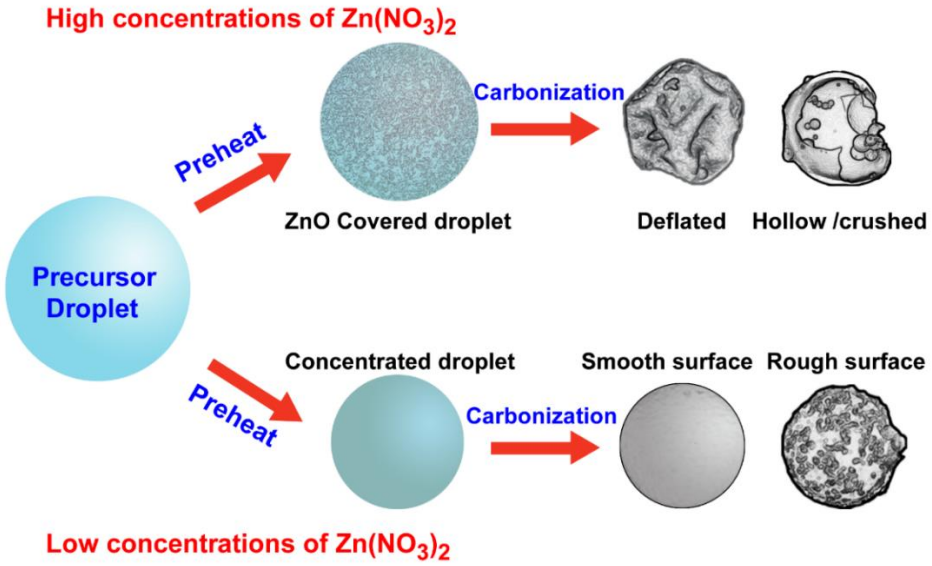

Figure 2.8 Illustration of the carbon nanospheres formation mechanism.

From the observed morphology dependence on the $Zn(NO_3)_2$ concentration, the formation mechanism for the carbon nanospheres is proposed as follows. ZnO nanoparticles formed during heating of $Zn(NO_3)_2$ at high temperature act as nucleation sites for carbonization of sugar to form carbon nanospheres. When high concentrations of $Zn(NO_3)_2$ were used, without much water evaporating from the droplet surface, enough $Zn(NO_3)_2$ will accumulate at the surface and reach the critical concentration, at which ZnO nanoparticles were made to form a shell, where inside precursors diffuse to and pyrolysis to form carbon "balloon" (High concentration of $Zn(NO_3)_2$ case in Fig. 2.8). With lower concentration of $Zn(NO_3)_2$, however, the droplets have to evaporate and shrink enough before $Zn(NO_3)_2$ reaches the critical concentration to pyrolysis and form ZnO nuclei, which make the precursors have enough time to diffuse inside and form solid nanospheres finally (Low concentration of $Zn(NO_3)_2$ case in Fig. 2.8). No carbon nanospheres were made by direct pyrolysis of pure sugar solutions at same conditions,

which suggests that the ZnO plays the role seed or nucleus for the formation of carbon nanospheres. The observed morphology dependence of the carbon nanospheres on the $Zn(NO_3)_2$ concentration offers another way to control the nanosphere features for different purposes. For instance, high surface area nanomaterials can be produced and used for water purification and drug delivery, *etc*.

To better understand the growth mechanism of the carbon nanospheres, different metal salts and carbon precursors were also investigated. The carbon nanospheres synthesized using $Zn(NO_3)_2$ and 3,4-dihydroxybenzaldehyde (1g:1g) and treated with HCl are shown in Figure 2.9a and showed similar morphologies as those prepared using sugar. Figure 2.9b-c shows the SEM images of carbon nanospheres prepared using sugar as the carbon source and manganese (II) nitrate hydrate and ferric chloride, respectively, in place of $Zn(NO_3)_2$. Using the manganese salt resulted in carbon nanospheres with a rough surface (Fig. 2.9b). The carbon nanospheres prepared with ferric chloride showed large holes on their surfaces after HCl etching (Fig. 2.9c). XRD of the as-prepared samples showed that the materials were amorphous, suggesting crystalline iron or manganese oxides did not form during the pyrolysis but that they may be amorphous oxides (Fig. 2.9d). The broad reflections observed in the sample prepared with the manganese salt are likely from the carbon, since they did not match reflections for MnO_2. Carbon nanospheres were also synthesized using $Zn(NO_3)_2$ and polyethyleneimine (PEI) (1g:1g). When PEI was used as the carbon source, the carbon nanospheres showed a deflated shape (Fig. 2.10a). The ability to use PEI as the carbon source provides the opportunity for preparing nitrogen doped carbon nanospheres. Thiourea was also added to the precursor solution along with the PEI. Fig. 2.10b shows the X-ray photoelectron spectroscopy (XPS) wide scan result

for as-prepared carbon nanospheres synthesized from 2 g $Zn(NO_3)_2$, 1 g PEI and 1 g thiourea. The peaks from N 1s and S 2p showed that these species were incorporated into the carbon nanospheres from the PEI and thiourea, respectively. The composition determined from XPS was about 55 at% C, 12 at% N, 19 at% S, with the balance being ZnO. These results show that different carbon sources and salts can be used to make the carbon nanospheres, but more studies are required to fully understand their formation mechanism compared to the $Zn(NO_3)_2$/sugar case.

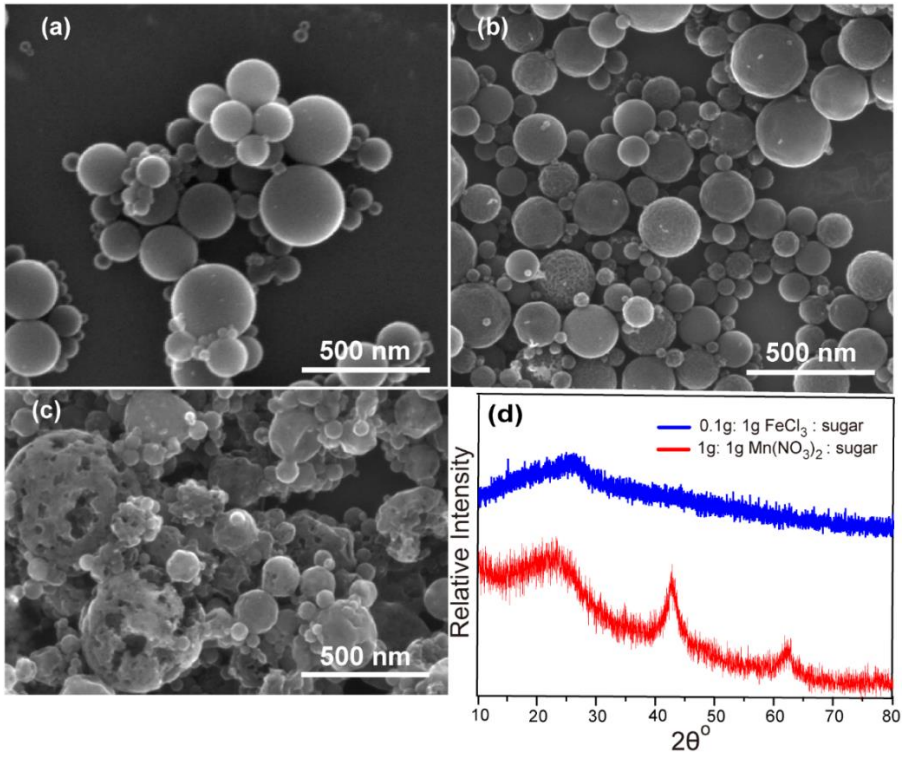

Figure 2.9 SEM images and XRD of carbon nanospheres synthesized from different carbon and metal salt precursors after HCl treatment. (a) $Zn(NO_3)_2$ and 3,4-dihydroxybenzaldehyde (1g:1g); (b) $Mn(NO_3)_2$ and sugar (1g:1g); (c) $FeCl_3$ and sugar (0.1g:1g); (d) XRD of as-prepared samples from 0.1g: 1g $FeCl_3$: sugar (blue) and 1g: 1g $Mn(NO_3)_2$: sugar (red).

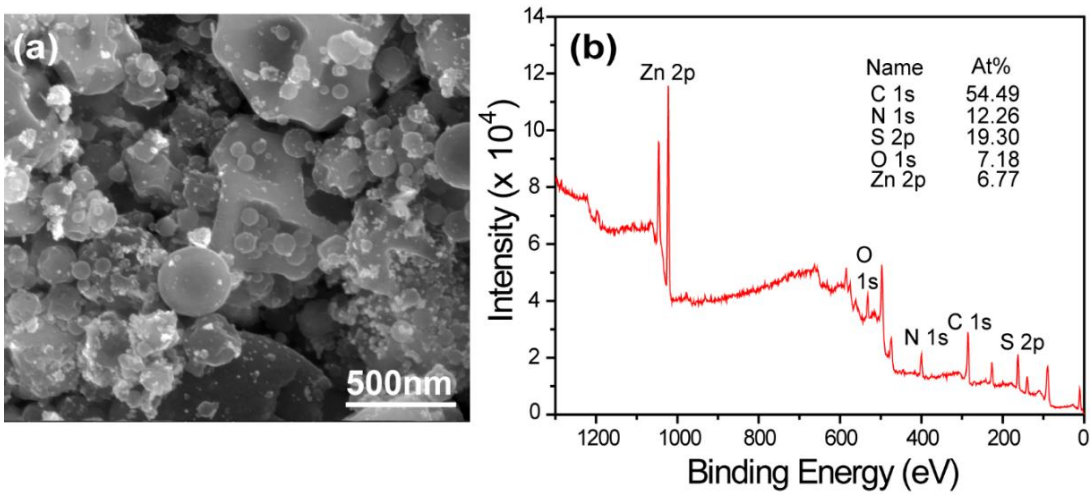

Figure 2.10 (a) SEM image of as-prepared carbon nanospheres synthesized from 1g:1g $Zn(NO_3)_2$ and PEI; (b) XPS wide scan and elemental analysis for carbon nanospheres prepared from 2 g $Zn(NO_3)_2$, 1g PEI and 1g thiourea.

2.5 Characterization and Applications of Carbon Nanospheres from Higher Precursor Concentrations

2.5.1 The Characterization of Carbon Nanospheres

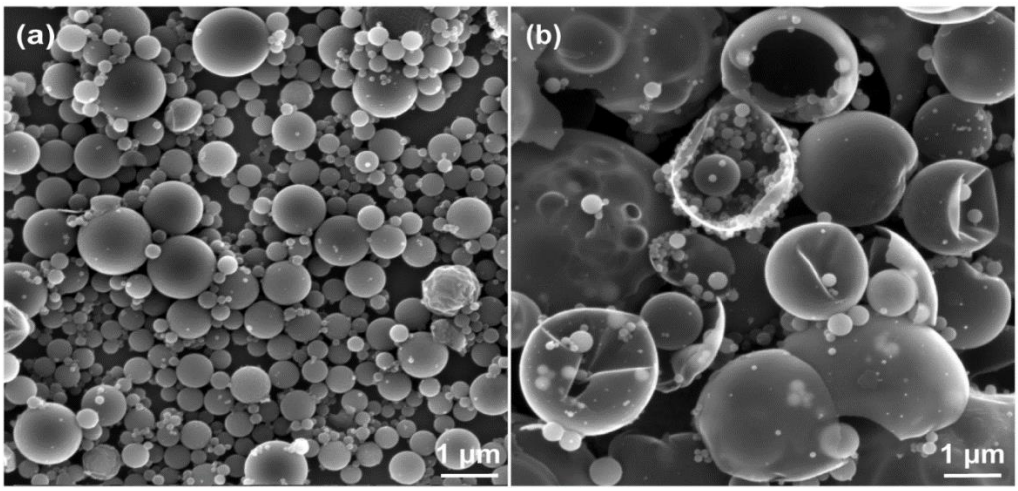

Figure 2.11 SEM images of carbon nanospheres prepared from precursors with $Zn(NO_3)_2$ to sugar ratios of (a) 3g:3g; (b) 6g:3g.

N_2 adsorption isotherms were used to determine the specific surface area (SSA) of the carbon nanospheres using the Brunauer–Emmett–Teller (BET) method at 77K. The adsorption isotherms were used to calculate the pore size distribution *via* Barrett–Joyner–Halenda (BJH) method. Higher precursor concentrations of $Zn(NO_3)_2$ to sugar were used to increase the product yield. Figure 2.11 shows the SEM images of samples prepared from 3g:3g and 6g:3g in 100 mL water. Although the diameters of the carbon nanospheres became larger, the carbon nanosphere structures were similar to those observed in 1g:1g and 3g:1g samples described above, with the 3g:3g sample displaying predominately solid carbon nanospheres and the 6g:3g sample displaying many porous hollow carbon nanospheres. Figure 2.12a shows the N_2 adsorption/desorption isotherms and Table 1 shows the SSA and total pore volumes for carbon nanospheres prepared with different precursor concentrations and subsequent heat treatments. For the sample prepared from 3g: 3g followed by treatment with HCl and annealing at 1000 ^oC for 1 h, the isotherm is classified as type I, which indicates that a microporous structure is generated from the holes when the ZnO nanoparticles were removed with HCl. The SSA of this sample was 920 m^2/g. For the sample prepared from 6g: 3g and treated with the same condition, the SSA was almost the same at 928 m^2/g. After annealing both of these samples at 2300 ^oC for 1 h, the SSAs dropped dramatically to 14 m^2/g and 42 m^2/g, respectively, indicating disappearance of the microporous structure during the crystallization at high temperature. When these two samples were annealed at 1100 ^oC directly without removing the ZnO with HCl, the SSA were 1106 m^2/g and 1036 m^2/g, respectively. This higher SSA compared to the samples with ZnO removed using HCl etching indicates that the ZnO may be etching additional carbon during the high temperature annealing, making the pores bigger. The

BET curves from samples prepared with higher $Zn(NO_3)_2$ concentration have larger slopes than samples from low $Zn(NO_3)_2$ concentrations. This corresponds with the hollow carbon nanosphere structures observed in the SEM (Fig. 2.11b). Importantly, these SSAs are about double those obtained for mesoporous carbon nanospheres synthesized using chemical vapor deposition on polystyrene templates.[47] Although, the total pore volume may be different for different samples, most of the pore sizes were around 2 nm (Fig 2.12b).

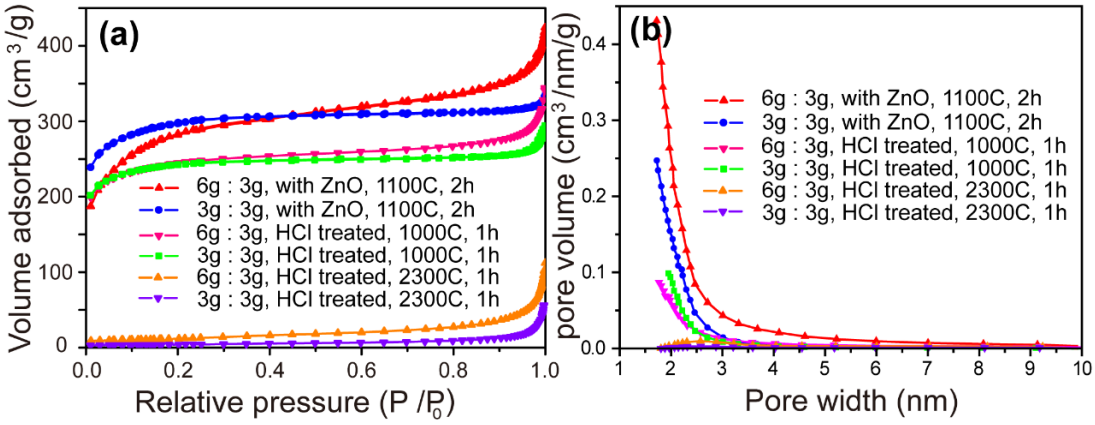

Figure 2.12 (a) N_2 adsorption-desorption isotherms of different carbon nanospheres. (b) Pore size distribution curves of different carbon nanospheres.

Table 2.1 Specific surface area and pore volume of carbon nanospheres measured from BET

$Zn(NO_3)_2$ to sugar ratio in precursor	Post-synthesis Treatment	SSA (m^2/g)	Pore volume (cm^3/g)
3g:3g	HCl etching then heat at 1000 °C for 1 h	920	0.30
6g:3g	HCl etching then heat at 1000 °C for 1 h	928	0.28
3g:3g	HCl treated then heat at 2300 °C for 1 h	14	0.06
6g:3g	HCl treated then heat at 2300 °C for 1 h	42	0.13
3g:3g	Heat at 1100 °C for 2 h	1106	0.32
6g:3g	Heat at 1100 °C for 2 h	1036	0.40

2.5.2 Application of Carbon Nanospheres as an Adsorbent for Dye Removal

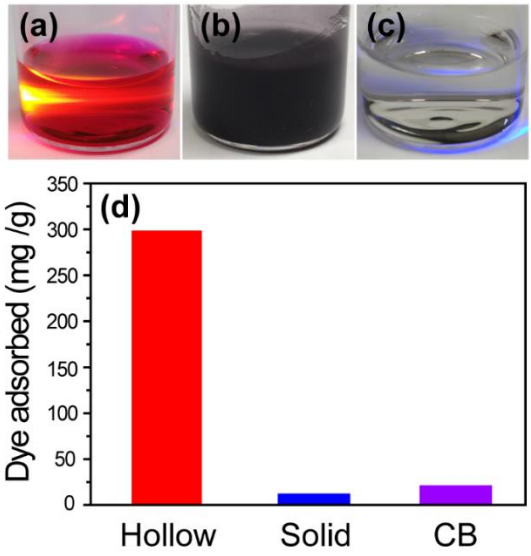

Figure 2.13 Photographs of (a) 100 mg/L RB solution under excitation with 405 nm laser, (b) carbon nanospheres suspended in the RB solution, (c) RB solution after carbon

nanospheres removed solution with excitation by 405 nm laser. (d) RB adsorption abilities of different samples (mg dye adsorbed per g carbon): hollow carbon nanospheres (prepared from 6g:3g followed by annealing at 1100 ^{o}C), solid carbon nanosppheres (prepared from 3g:3g), and commercial carbon black (CB).

To make use of the high SSA of the carbon nanospheres, dye adsorption experiments were conducted. The hollow carbon nanospheres prepared from solutions containing 6g:3g $Zn(NO_3)_2$:sugar, followed by annealing at 1100 ^{o}C for 2 h (without removing ZnO) were added to a 100 mg/L rhodamine B (RB) solution (Fig. 2.13a) and suspended with sonication for about 5 min (Fig. 2.13b). After removing the carbon nanospheres with filtration, the clear water could be observed (Fig. 2.13c). UV-Vis spectroscopy was used to determine the concentration of the dye remaining in the solution using Beer's law. As shown in Figure 2.14, the remaining RB in solution was only around 0.087 mg/L when 300 mg of dye was mixed with 1 g of carbon nanospheres (300 mg/g). For the solid carbon nanospheres prepared from 3g:3g and treated with same conditions, the dye adsorption ability was much less compared to the hollow materials despite its slightly higher SSA (Table 2.1). Even when using a dye:carbon ratio of only 12 mg/g, the concentration of RB remained in the solution was still as high ~1.5 mg/L (Fig. 2.14). As a comparison, commercially available carbon black with SSA 45 m^2/g was found to adsorb ~20 mg/g, even higher than the solid carbon nanospheres. The results reveal that for solid carbon nanospheres, the dye molecules may not be able to access the pores inside the nanospheres. Instead, only the external surface could be used for adsorption. For hollow carbon nanospheres, the internal pores are more accessible to the dye molecules, which explains why its adsorption ability is much higher.

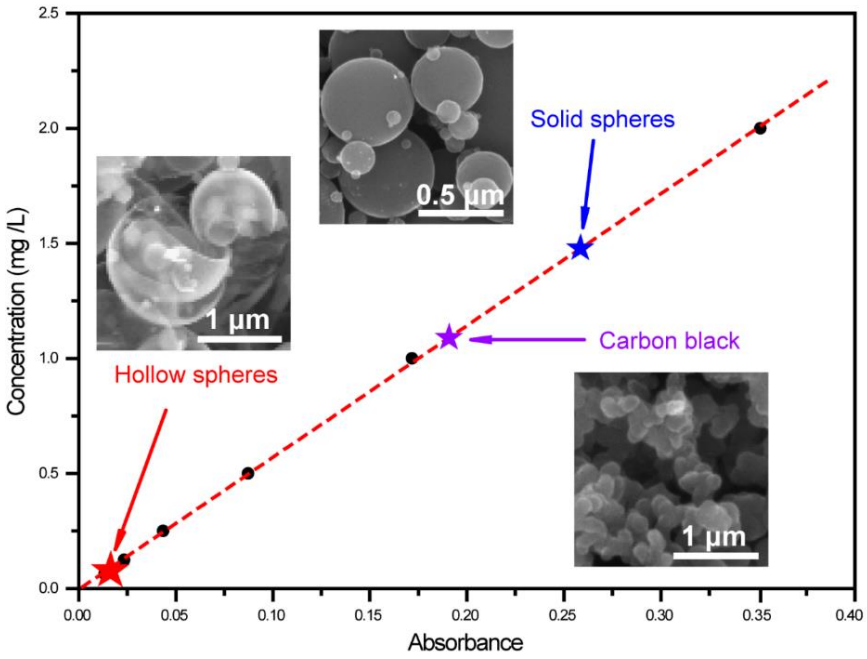

Figure 2.14 Calibration curve for used to determine concentration of RB using UV-vis spectroscopy. Black points correspond to the calibration points. Stars correspond to the concentrations of remaining RB after sorption onto different carbon samples: hollow carbon nanospheres (300 mg dye per g carbon), solid carbon nanospheres (12 mg/g), and carbon black (20 mg/g). Insets show the corresponding SEM images.

2.5.3 Application of Carbon Nanospheres as an Adsorbent for Removal of Arsenate and Selenate from Water

As an effective adsorbent, the adsorption ability of carbon nanospheres was also studied for removal of arsenate (As(V)) and selenate (Se(VI)). Unlike most toxic metal ions such as lead and mercury, arsenate and selenate are difficult to remove with common activated carbon adsorbents, since they are negatively charged species in neutral pH solutions. For activated carbons, due to the wide range of preparation conditions, they can have very different porosity, surface functional groups, and specific surface area. Here

the adsorption ability of carbon nanospheres and commercially available activated carbons (Cabot Norit® 20BF powdered activated carbon (PAC, 325 mesh) and GAC-820 granular activated carbon (GAC, 8 x 20 mesh)) was compared for As(V) and Se(VI) removal. The carbon nanospheres used here were prepared with $Mn(NO_3)_2$ as catalyst. Specifically, 1 g sucrose and 1 g $Mn(NO_3)_2$ were dissolved in 100 mL DI water and sprayed using N_2 carrier gas into a tube furnace heated at 1000 ^oC. High temperature annealing at 1200 ^oC for 2 hours under Ar was performed, followed by etching with concentrated HCl and washing in DI water to form the final product consisting of carbon nanospheres with a median diameter of ~ 70 nm, with the largest particle size < 1 micron. Figure 2.15b shows typical scanning electron microscopy (SEM) images of the carbon nanospheres. Transmission electron microscopy (TEM) of the material after carbonization showed that the carbon nanospheres contained manganese oxide nanoparticles 2 – 10 nm in diameter (Fig. 2.15c). After etching, the nanoparticles were dissolved to reveal empty micropores (Fig. 2.15d). Based on the X-ray diffraction (XRD, Fig. 2.16a) and Raman spectroscopy (Fig. 2.16b) analysis, the carbon nanospheres adopted a disordered amorphous structure with predominately carbon sp^3 bonding. As you can see, although $Mn(NO_3)_2$ was used as catalyst here, the features of carbon nanospheres are similar with those prepared with $Zn(NO_3)_2$, which is consistent with the results mentioned above.

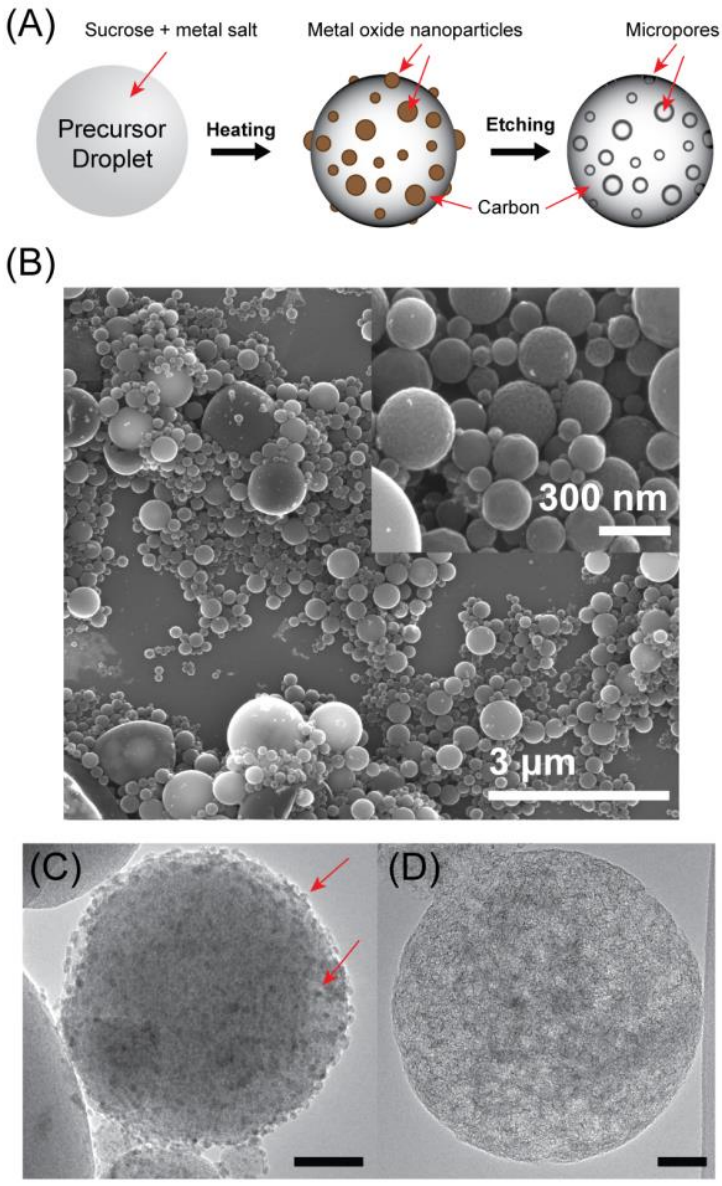

Figure 2.15 (a) Schematic of formation mechanism for synthesis of microporous carbon nanospheres. (b) SEM images of synthesized carbon nanospheres. TEM images of carbon nanospheres (c) after carbonization as a composite with metal oxide nanoparticles (noted with arrows) and (d) after acid etching to dissolve the metal nanoparticles. Scale bar = 50 nm.

Both commercial activated carbons studied (PAC and GAC) are prepared from bituminous coal. The Raman spectrum for PAC showed a similar disordered structure as that in the carbon nanospheres (Fig. 2.16b) but the (002) and (100) planes associated with graphitic carbon can be discerned in the XRD pattern (Fig. 2.16a). Thus, the structure of PAC is likely a mixture of disordered carbon with some regions of graphitic, sp^2 carbon.

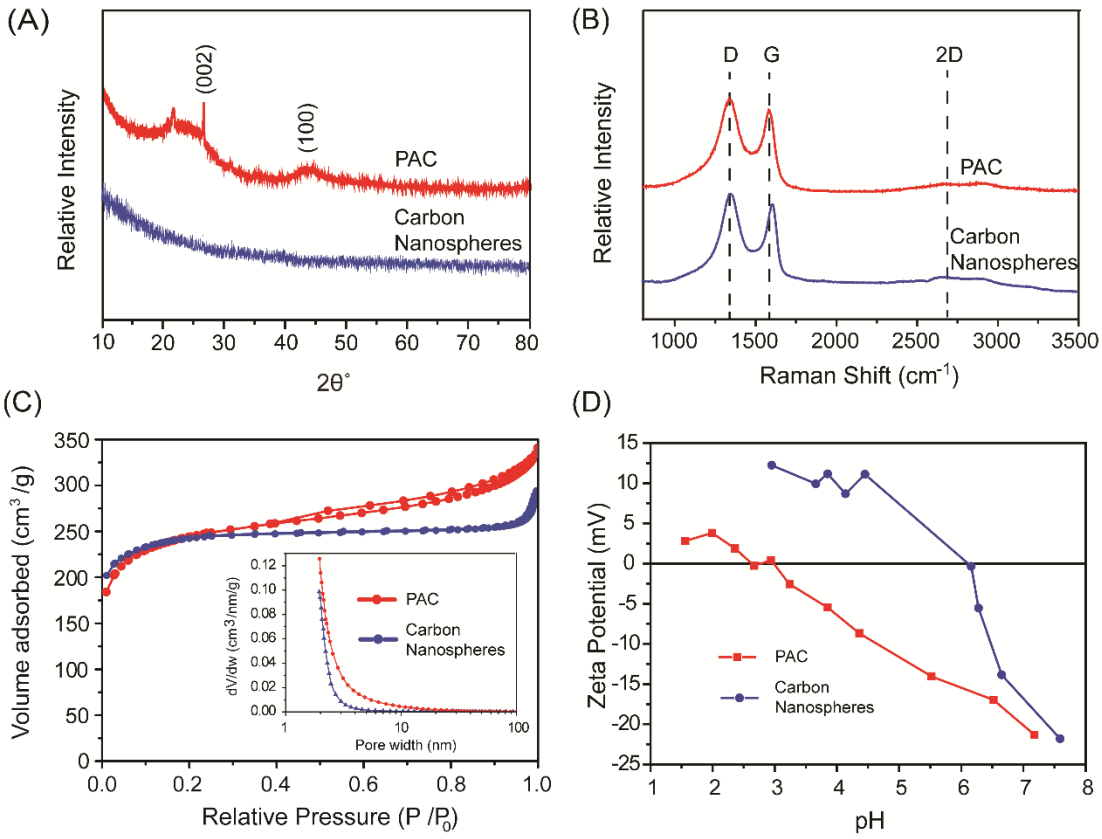

Figure 2.16 (a) XRD, (b) Raman spectra, (c) N_2-sorption curve with pore size distribution the inset, and (d) Zeta potential measurement for PAC compared with carbon nanospheres.

The specific surface area for the carbon nanospheres using the Brunauer-Emmett-Teller (BET) method at 77 K in nitrogen (Micromeritics TriStar II 3020) was around 1000 m^2/g with a pore volume around 0.28 cm^3/g. Gas sorption measurements on PAC determined a

BET surface area of 864 m^2/g and pore volume of 0.22 cm^3/g. GAC has been reported with a BET surface area of 908 m^2/g and pore volume of 0.5 cm^3/g.[123] The nitrogen-sorption isotherm for the carbon nanospheres and PAC are shown in Figure 2.16c. While PAC shows a type IV isotherm with hysteresis, indicating some mesoporosity,[124] the CNS had a type I isotherm with no hysteresis. This indicates that the CNS contained mostly micropores < 2 nm and no significant pore volume associated with mesopores (2 – 50 nm) or macropores (> 50 nm), as shown by the Barrett-Joiner-Halenda (BJH) derivative pore distribution plot (Fig. 2C, inset). This is consistent with the formation mechanism of the porous carbon nanospheres and the results mentioned above.

Zeta potential measurements were performed on the PAC and CNS (ZetaPALS, Brookhaven Instruments). As shown in Fig. 2.16d, the isoelectric point (pH where the zeta potential is zero) for PAC was around pH 2.5–3, which is typical for coal-derived activated carbons with acidic surface groups (L-type carbon).[125] In contrast, the isoelectric point for the CNS was around 6.16. The higher isoelectric point in the CNS is a result of the high temperature annealing temperatures used in the synthesis, which can remove the oxidised acidic surface groups.[126] Basic carbons with anionic exchange properties (H-type carbons) can be obtained when heating >950 ℃ in vacuum or inert atmosphere.[125]

Batch adsorption experiments were performed using the carbon materials at a concentration of 0.44 g/L in water spiked with 1 ppm Na_2SeO_4 and 1 ppm $Na_2HAsO_4 \cdot 7H_2O$. The sorbents were added to the spiked solutions and stirred at a constant speed with sampling at different time periods. The sorbents were then removed with filtration and the filtrate was analyzed with inductively coupled plasma atomic

emission spectroscopy (ICP-AES). Ultrapure DI water (18.3 MΩ-cm, pH 5.5) was used for synthetic water solutions. The predominant species at this pH are SeO_4^{2-} and $H_2AsO_4^-$.[59,127] Water samples were also obtained from the service canal and B well that serve as makeup water for the boiler and cooling towers at the Salt River Project Santan Generating Facility in Gilbert, AZ. The canal and well waters were spiked with 1 ppm selenate or arsenate in the same manner. The pH of the canal and well waters were 8.54 and 8.30, respectively. In this pH range, the dominant Se(VI) species is still SeO_4^{2-}, but the As(V) is found as the doubly charged anion, $HAsO_4^{2-}$.[59,127]

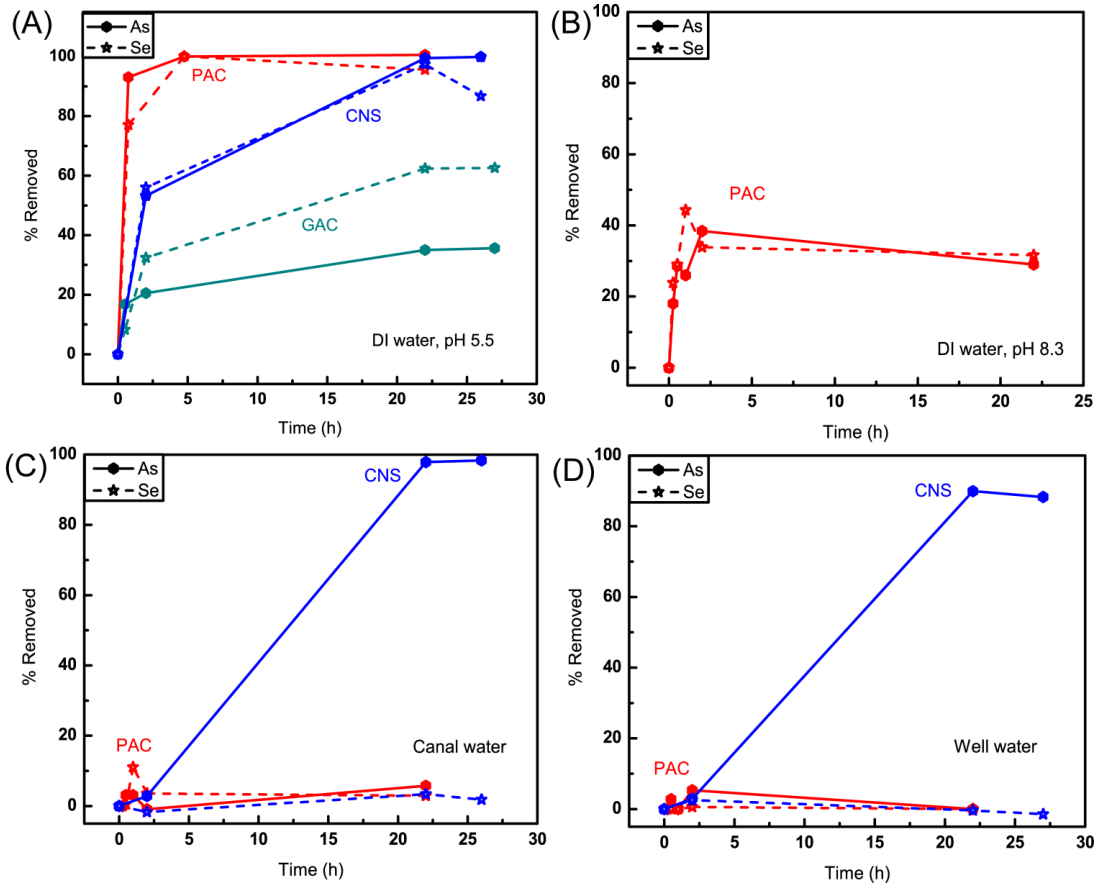

Figure 2.17 Percentage removed of 1 ppm As(V) and 1 ppm Se(VI) on carbon nanospheres compared to powdered activated carbon (PAC) and granular activated carbon (GAC) at

dosage of 0.44 g/L in (a) DI water, pH 5.5, (b) DI water, pH 8.3, (c) canal water, and (d) well water.

The arsenate and selenate removal over time with carbon sorbents is shown in Fig. 2.17 in the different water samples. As Fig. 2.17a shows, in DI water CNS can remove 53% arsenate in 2 hours, and almost 100% arsenate in 22 hours. Even in the canal water (Fig. 2.17c) and well waters (Fig. 2.17d), still more than 89% arsenate could be removed in 22 hours, although the initial removal rates were slower, only about 3% removed in first 2 hours. Compared with DI water, the slightly lower removal efficacy for arsenate in the canal and well waters can be explained by their higher pH. The anionic adsorption capability of carbons is typically attributed to surface functional groups such as –COOH, $–OH_2^+$, $–COO^–$, –OH, $–O^–$, which become protonated and/or positively charged when dispersed into aqueous solutions.[63,128,129] Typically, the arsenate adsorption capacities of activated carbons reported in the literature reached maximum at pH 2–5,[130,131] where the carbon surface was positively charged. Here, due to its high isoelectric point, the CNS displays good arsenate adsorption even at pH > 8, without any surface modification. Moreover, the canal and well water also contains the competing anion species such as nitrate (typically 60–130 ppm) and sulfate (700–1000 ppm), which did not seem to have large effect on the arsenate adsorption.

For selenate removal in DI water, CNS could remove 56% and 97% selenate in 2 and 22 hours, respectively (Fig. 2.17a). When tested in the canal (Fig. 2.17c) and well waters (Fig. 2.17d), the selenate removal efficacy of the CNS was very low, only about 2–3%, due to the presence of completing anions. Sulfate has been found to compete with selenate binding on various sorbents due to its similar anion structure and adsorption

behavior.[132,133] One way to potentially address this problem is to use a barium salt to precipitate out the sulfate from the water prior to its exposure to the sorbent.[134]

As a comparison, PAC and GAC were also used to conduct the adsorption experiment under the similar conditions. In DI water, PAC could adsorb arsenate and selenate faster than the CNS, with 93% arsenate and 77% selenate removed in first 45 minutes. Similar to the CNS, all of the arsenate and selenate could be removed in longer exposure time. However, GAC could only remove 35% of the arsenate and 62% of the selenate in 22 hours. Due to the poor performance in DI water, GAC was not tested further.

When further tested in the canal and well water, PAC, however, could barely remove arsenate and selenate anymore. To further investigate whether the low removal efficacy of PAC in the canal and well waters was due to the higher pH or the presence of competing ions, the pH of the DI water was adjusted to 8.3 by adding NaOH and the results are shown in Fig. 2.17b. Comparing with the results obtained in DI water without pH adjustment (Fig. 2.17a), both arsenate and selenate removal efficiencies of PAC decreased about half, which means the higher pH of the solution does have a negative effect on the adsorption properties. This suggests that the worse performance of PAC in the canal and well waters was mainly due to the decrease in positively charged surface binding sites as the result of the higher pH.

2.5.4 Application of Carbon Nanospheres for Supercapacitors

To evaluate the performance of the carbon nanospheres as supercapacitor electrode materials, a two-electrode configuration[69] was used in coin cells with 6 M KOH electrolyte. The cyclic voltammetry (CV) curves from -0.5 V to 0.5 V for supercapacitors made from hollow and solid carbon nanospheres are shown in Fig. 2.18a and Fig. 2.19a,

respectively, while the galvanostatic charge-discharge curves obtained at different current densities are shown in Fig. 2.18b and Fig. 2.19b. From the IR drop obtained from the discharge curves, the internal resistance (IR) or equivalent series resistance (ESR) was around 24 Ω and 30 Ω for the hollow and solid carbon nanospheres, respectively, which was a little high and might be due to the small contact points between the nanospheres. Based on the charge-discharge curves, the specific capacitances were 112 F/g and 105 F/g for the hollow and solid carbon nanospheres, respectively, at a current density of 0.1 A/g. Even when the current density increased as high as 10 A/g, the specific capacitances still remained 88.5 F/g and 79.5 F/g, respectively. Similar with the dye adsorption result, the hollow nanospheres had better performance than the solid ones. However, since the electrolyte ion is much smaller than the dye molecule, the difference in performance was not as significant as in dye adsorption. The specific capacitances observed for the carbon nanospheres are higher than typical values observed in carbon nanotube electrodes (50-100 F/g),[135] but a little lower than those observed in other mesoporous carbon nanospheres (~200 F/g)[47] and graphene (100-250 F/g).[4,5,7,136] The specific capacitance in supercapacitors prepared from both solid and hollow carbon nanospheres was stable with very little decrease, with the final capacitance retention of 100.3% and 99.2% after 20,000 cycles for the solid and hollow nanospheres, respectively. In contrast, only 96% capacitance retention was observed after 10,000 cycles for other mesoporous carbon nanosphere supercapacitors.[47] Since the carbon nanosphere samples were observed to be somewhat hydrophobic, it is likely that the electrolyte wetting was improved after cycling, allowing more of the internal micropores to be accessible to the ions. This suggests that the specific capacitances observed here may be further increased if the carbon

nanospheres are modified with surface functionalization to improve electrolyte wetting, which will be investigated in future studies.

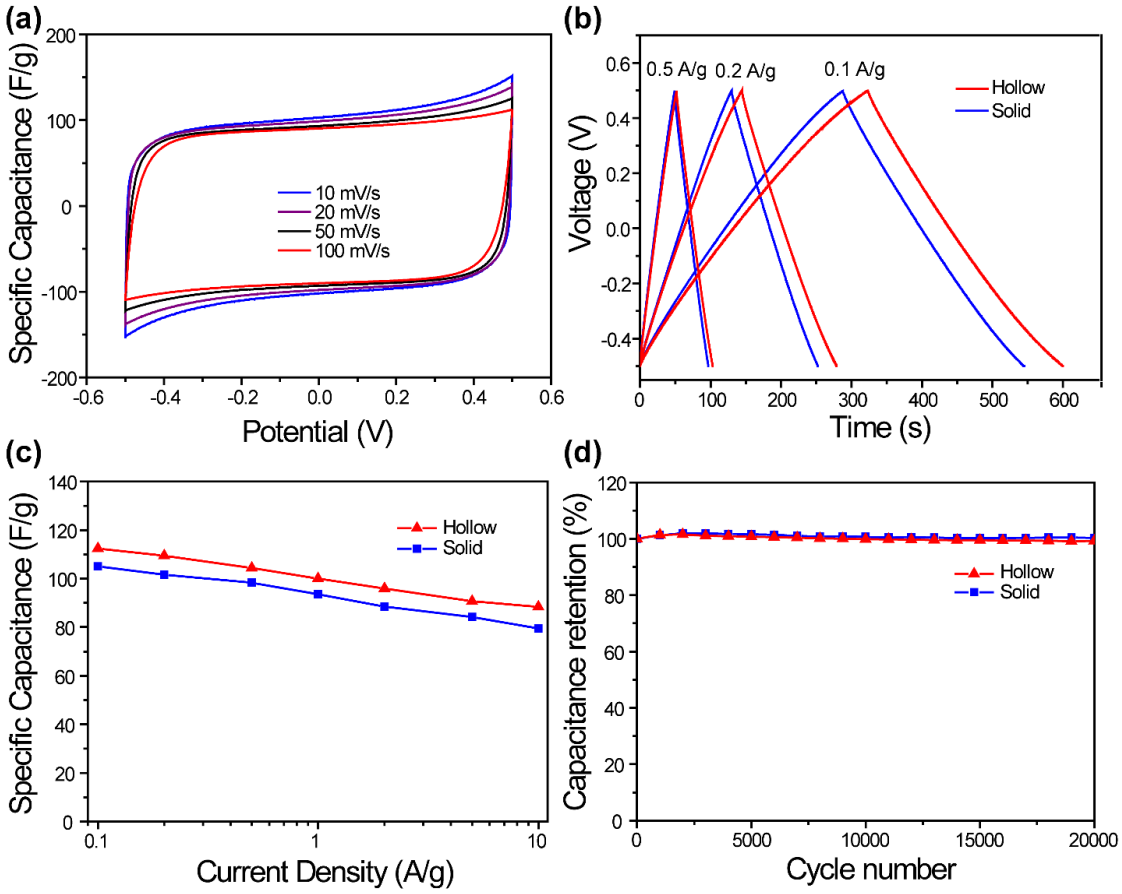

Figure 2.18 Performance of carbon nanosphere supercapacitors in 6 M KOH aqueous electrolyte. (a) CVs curves obtained using different scan rates for supercapacitor made from hollow carbon nanospheres. (b) Galvanostatic charge/discharge curves of supercapacitors made from hollow or solid carbon nanospheres at different current densities. (c) The specific capacitance at different current densities. (d) Cycle life of different capacitors at a current density of 10 A/g.

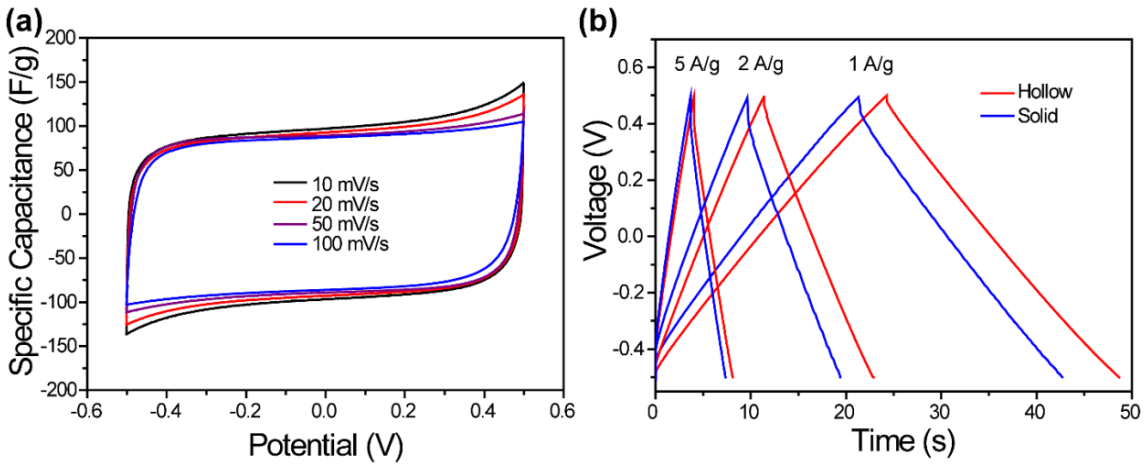

Figure 2.19 (a) Cyclic voltammograms (CVs) curves at different scan rates for supercapacitor made of solid carbon nanospheres in 6 M KOH aqueous electrolyte. (b) Galvanostatic charge/discharge curves of supercapacitors made from hollow or solid carbon nanospheres at different current densities.

2.5.5 Application of Carbon Nanospheres for Lithium Ion Battery

The performance of the carbon nanospheres was also evaluated for lithium ion battery applications. The porous carbon spheres (PCS) investigated here were prepared by dissolving 3 g sucrose and 3 g $Zn(NO_3)_2$ in 100 mL DI water and sprayed using N_2 carrier gas into a tube furnace heated at 1000 ^oC. The product was collected and then annealed either at 1200 ^oC (referred to as PCS-1200) or 2300 ^oC (PCS-2300) for 2 h under Ar atmosphere.

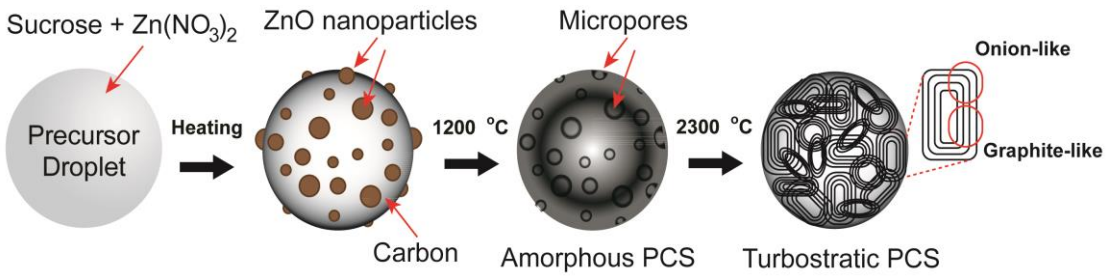

Figure 2.20 Schematic of the synthesis of amorphous and turbostratic porous carbon spheres

Figure 2.20 shows the schematic description about the synthesis of porous carbon spheres. Just as the processes mentioned above, the precursor droplet containing sucrose and $Zn(NO_3)_2$ was sprayed into the furnace, where they converted to carbon-ZnO nanoparticles composite spheres. When further annealed at high temperatures, the carbothermal reduction of ZnO will create porosity.[70] The X-ray diffraction (XRD) pattern (Fig. 2.21a) and Raman spectra (Fig. 2.21b) confirmed that porous carbon spheres heat treated at 1200 ℃ (PCS-1200) has an amorphous structure, while the graphite (002) and (100) reflections are clearly evident in the PCS-2300 XRD pattern confirming a more ordered structure. Additionally, the 2D band at ~2680 cm^{-1}, which is characteristic of graphitic carbon, also appeared in the Raman spectra of PCS-2300.[137] The SEM images (Fig. 2.22a-b) and low resolution TEM (Fig. 2.22c-d) of porous carbon spheres annealed at 1200 ºC and 2300 ºC showed that temperatures did not play a role in the morphology and size distribution (100-2000 nm). However, the structural differences are evident from the high-resolution TEM images, in which graphitic layers are clearly observed in PCS-2300 (Fig. 2.22f) but not in PCS-1200 (Fig. 2.22e). These layers are not perfect concentric sheets like those previously observed in onion-like carbon, which can be

considered multi-shelled fullerenes.[138,139] Rather, the PCS-2300 contained domains about 5 nm in size containing about 3-5 graphene layers, which can be considered a turbostratic structure (Fig. 2.22f, inset). Within each domain are regions of high curvature, imparting onion-like character, as well as planar regions that are more graphitic (Fig. 2.20). In contrast, the PCS-1200 showed a porous amorphous structure.

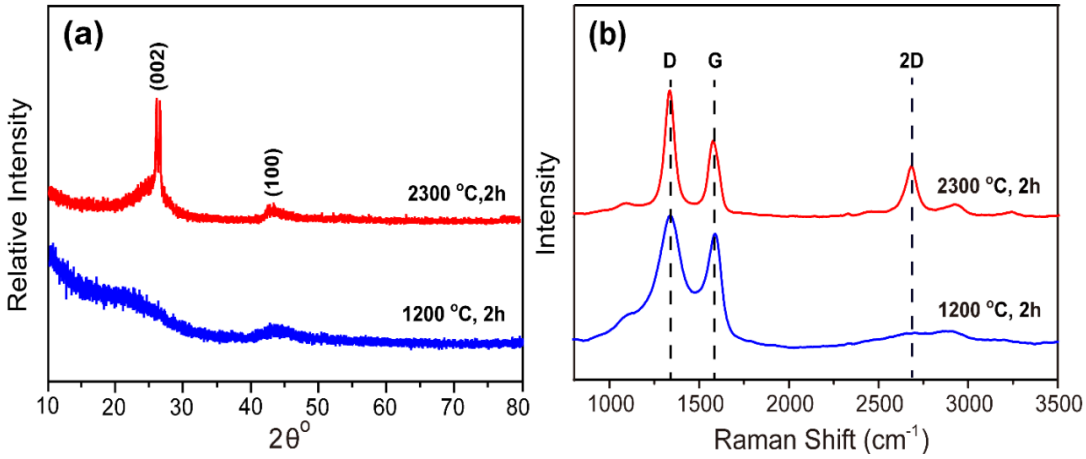

Figure 2.21 (a) XRD patterns and (b) Raman spectra of porous carbon spheres annealed at 1200 ℃ and 2300 ºC

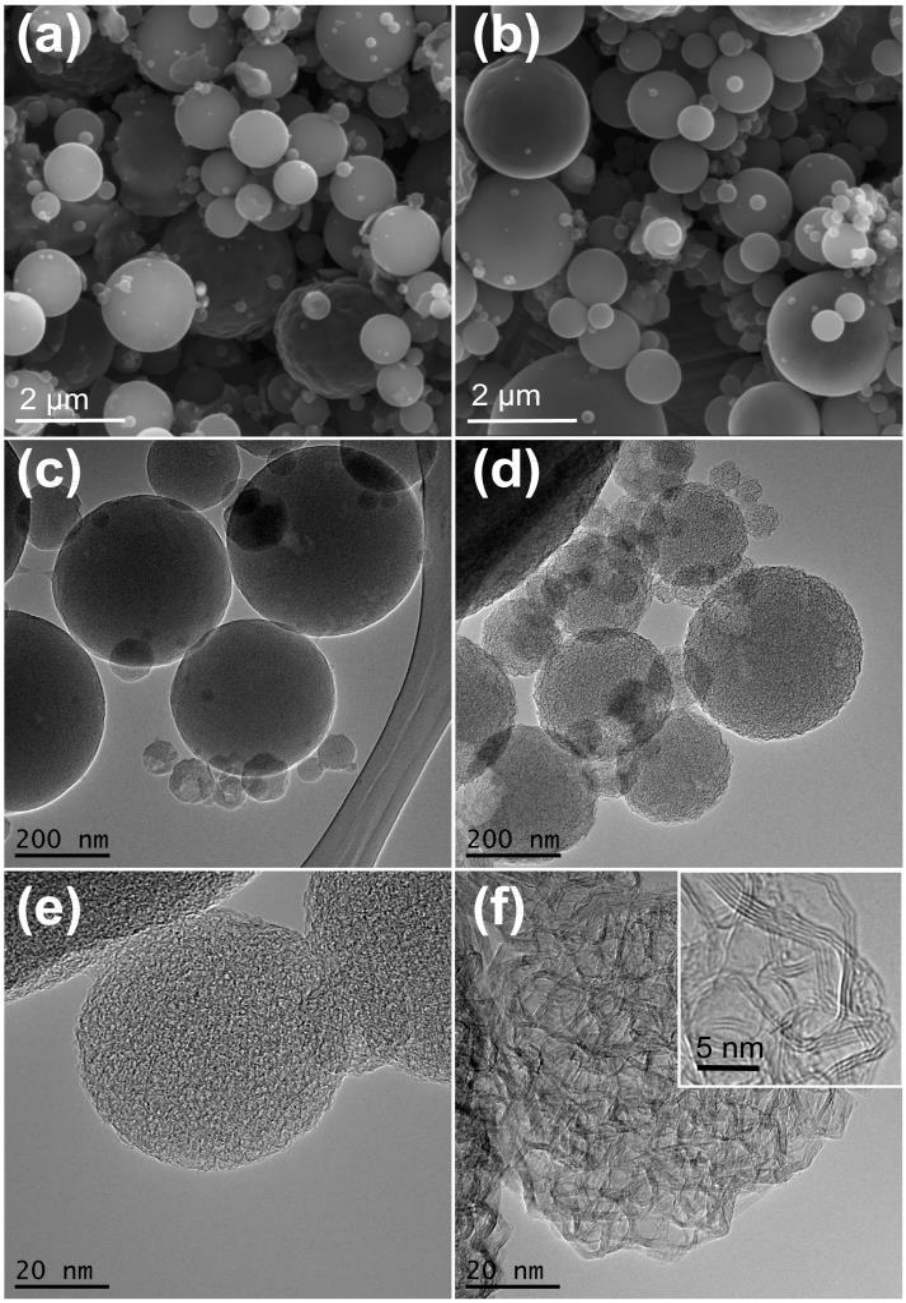

Figure 2.22 SEM (a, b), low resolution TEM (c, d) and high resolution TEM (e, f) images of porous carbon spheres annealed at (a, c, e) 1200 ^{o}C and (b, d, f) 2300 ^{o}C.

N_2 adsorption/desorption isotherms and pore size distributions of porous carbon spheres are shown in Figure 2.23. The low temperature treated spheres PCS-1200 with a

specific surface area of 1100 m^2/g displayed a type I isotherm, which indicates a microporous structure. After annealing at 2300 ℃, the surface area of the carbon spheres decreased to 14 m^2/g and was associated with a type III isotherm and the disappearance of microporous structure. During the crystallization of the turbostratic structure, mesopores and a higher degree of macropores originated in PCS-2300. It should be noted that porosity was retained even after heating the carbon spheres at 2300 ℃.

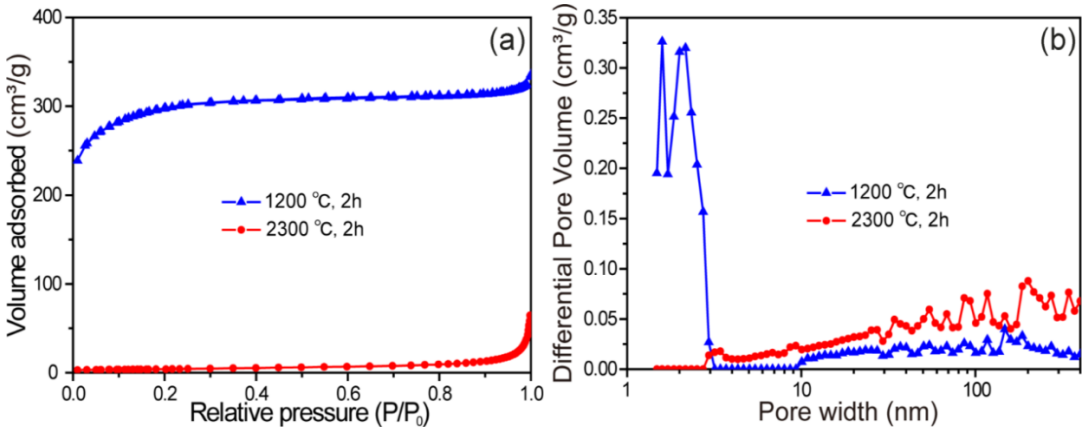

Figure 2.23 (a) N_2 adsorption-desorption isotherm and (b) pore size distribution of porous carbon spheres annealed at 1200 ºC, and 2300 ºC

Cyclic voltammetry (CV) analysis was used to investigate the electrochemical response of porous carbon spheres in the voltage range of 3.0-0 V (Figure 2.24a-b). Both samples showed the cathodic feature of Li^+ insertion into disordered amorphous carbons,[140] rather than the redox peaks typically seen in graphite,[141] which is expected for the amorphous sample, but unexpected for the high temperature treated PCS-2300. However, CVs of turbostratic carbons still display obvious peaks at the potentials corresponding to some of the staging processes observed during lithiation and delithiation of graphite.[142] The absence of these features in PCS-2300 might be due to additional

disorder from the imposed curvature of the spheres and lack of long-range order between the various graphitic-like regions of different domains. Similarly, previous electrochemical studies on carbon onions also did not show staging features during lithiation possibly because of the lack of long-range order caused by the high curvature of the stacked sheets.[143–145] Another notable feature in the CVs of the porous carbon spheres is the large reduction current associated with formation of the solid electrolyte interphase (SEI). The large cathodic peak of PCS-1200 at 0.25 V can be attributed to its high surface area compared to PCS-2300, causeing more SEI formation. The narrower anodic and cathodic bands of PCS-2300 also further prove the graphitic structures in turbostratic carbon spheres.

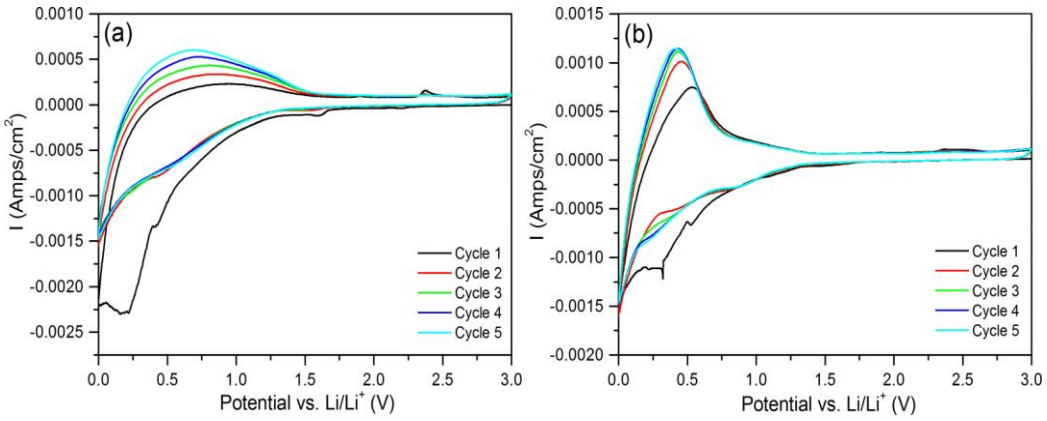

Figure 2.24 Cyclic voltammogram of porous carbon spheres annealed at (a) 1200 ^oC, and (b) 2300 ^oC at a scan rate of 1 mV/s

The first cycle charge and discharge voltage profiles obtained at a current density of C/10 for PCS-1200 and PCS-2300 are shown in Figure 2.25a-b, respectively. Due to the large SEI formation caused by its high surface area (~1100 m^2/g), the amorphous carbon sphere sample PCS-1200 had more irreversible capacity loss than that of PCS-2300

containing more graphitic structure. Initial cycle coulombic efficiency of PCS-1200 and PCS-2300 are 29 % and 58 %, respectively. The second cycle voltage profiles of carbon spheres at various charge-discharge rates are presented in Figure 2.25c-d. Both samples showed typical slopping voltage profiles of disordered carbons. The same shape of the voltage profiles at various current densities implied similar type of Li-intercalations reactions in the porous carbon spheres at different charge-discharge rates. Lithiation at higher potentials with sloping voltage profile makes such porous carbon spheres safer anode compared to commercial graphite anode, which suffers Li-dendrite growth issue due to Li-intercalation at lower potentials (<0.3 V *vs.* Li^+/Li).

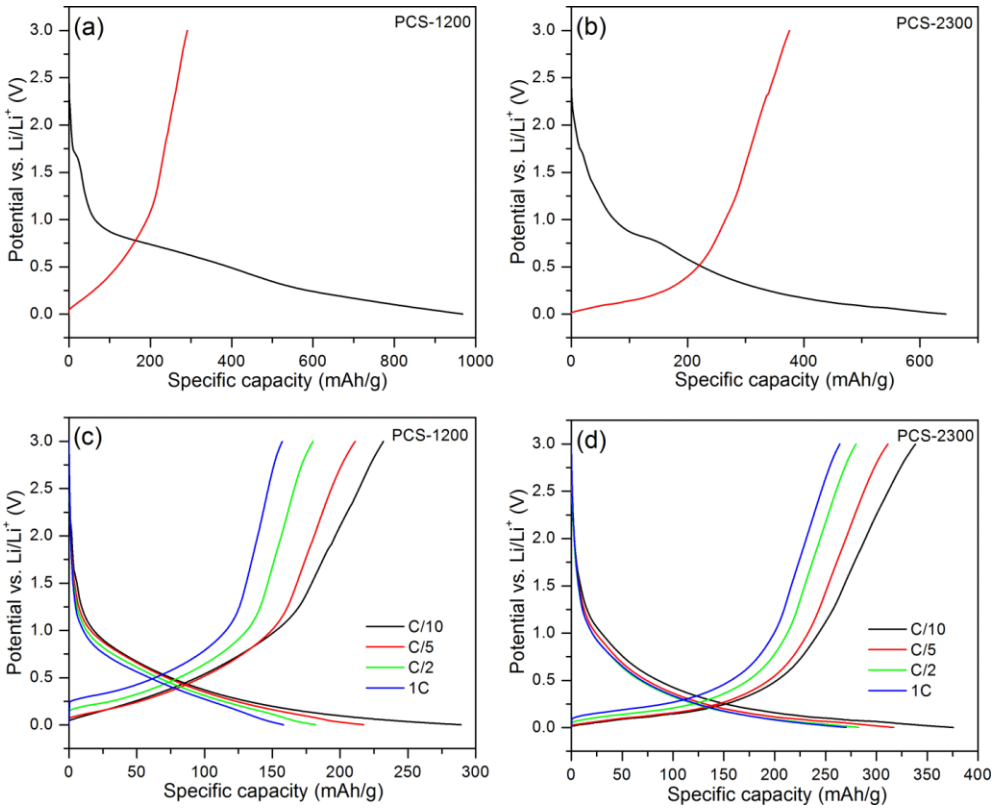

Figure 2.25 First cycle discharge and charge voltage profiles of porous carbon spheres annealed at (a) 1200 ^oC, and (b) 2300 ^oC at a current density of C/10. Second cycle voltage

profile at various current densities for porous carbon spheres annealed at (c) 1200 ^{o}C, and (d) 2300 ^{o}C

According to the electrochemical rate performances at different current densities (Figure 2.26a), the Li-ion storage performances of amorphous, turbostratic and commercial graphite anodes are significant different. At a low rate of C/10, graphite and PCS-2300 showed a reversible capacity of 378 mAh/g, which equivalent to the theoretical capacity of graphite (372 mAh/g). However, at higher charge-discharge rates, specific capacity of graphite anode decreased considerably, while PCS-2300 still kept significant capacity. For instance, at a current density of 1C, PCS-2300 demonstrated a discharge capacity of 270 mAh/g, which is 4-fold higher than those of the commercial graphite anode (60 mAh/g). Under similar experimental conditions, even PCS-1200 showed 2-fold higher (155 mAh/g) capacity than graphite anode. The electrochemical performance of these turbostratic carbon spheres is notably higher than those of solid carbon spheres reported previously, which had low reversible capacity and severe capacity fading.[146–149] The poor performance of graphite at high cycling rates is well known and has been previously attributed to slow kinetics and poor solid-state diffusion of Li^{+} within the particles.[150]

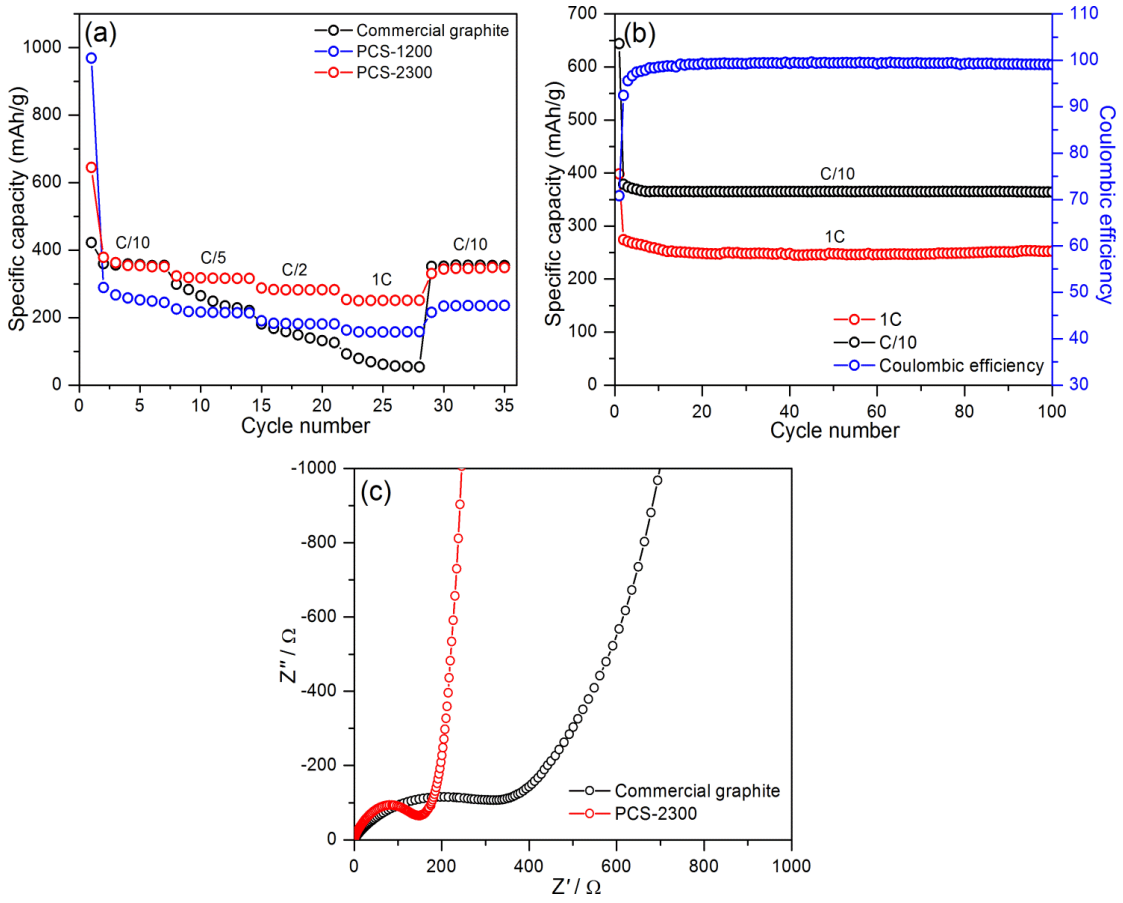

Figure 2.26 (a) Electrochemical rate performances of porous carbon spheres annealed at 1200 ^{o}C, 2300 ^{o}C, and commercial graphite; (b) Galvanostatic cycling performance of porous carbon spheres annealed at 2300 ^{o}C at 1C rate. (c) Electrochemical impedance spectra of porous carbon spheres annealed at 2300 ^{o}C, and commercial graphite

The long term electrochemical stability was tested for the electrochemically most active turbostratic carbon spheres (Figure 2.26b). After 100 charge-discharge cycles at current densities of 0.1 and 1 C, PCS-2300 retained stable specific capacities of 365 and 250 mAh/g, respectively. Capacity fading was noticed only during the first few cycles, which was ascribed to the SEI formation. Further investigation of porous turbostratic spheres to get insight into the superior electrochemical performance was carried out using

electrochemical impedance spectroscopy (EIS). Nyquist plots for PCS-2300 and commercial graphite anode are showed in Figure 2.26c. The semicircle arises from the sum of the contact resistance, SEI resistance, and charge-transfer resistance, while the 45^{o} line is due to solid-state Li^{+} diffusion.[151–154] The smaller diameter and lower solid-state diffusion resistance of PCS-2300 demonstrated superior Li-ion diffusion in porous carbon spheres compared to graphite anode. This can be explained by their unique disordered turbostratic structure and porosity, which results in the faster solid-state Li-ion diffusion, and superior electrode-electrolyte contact (interfacial kinetics).

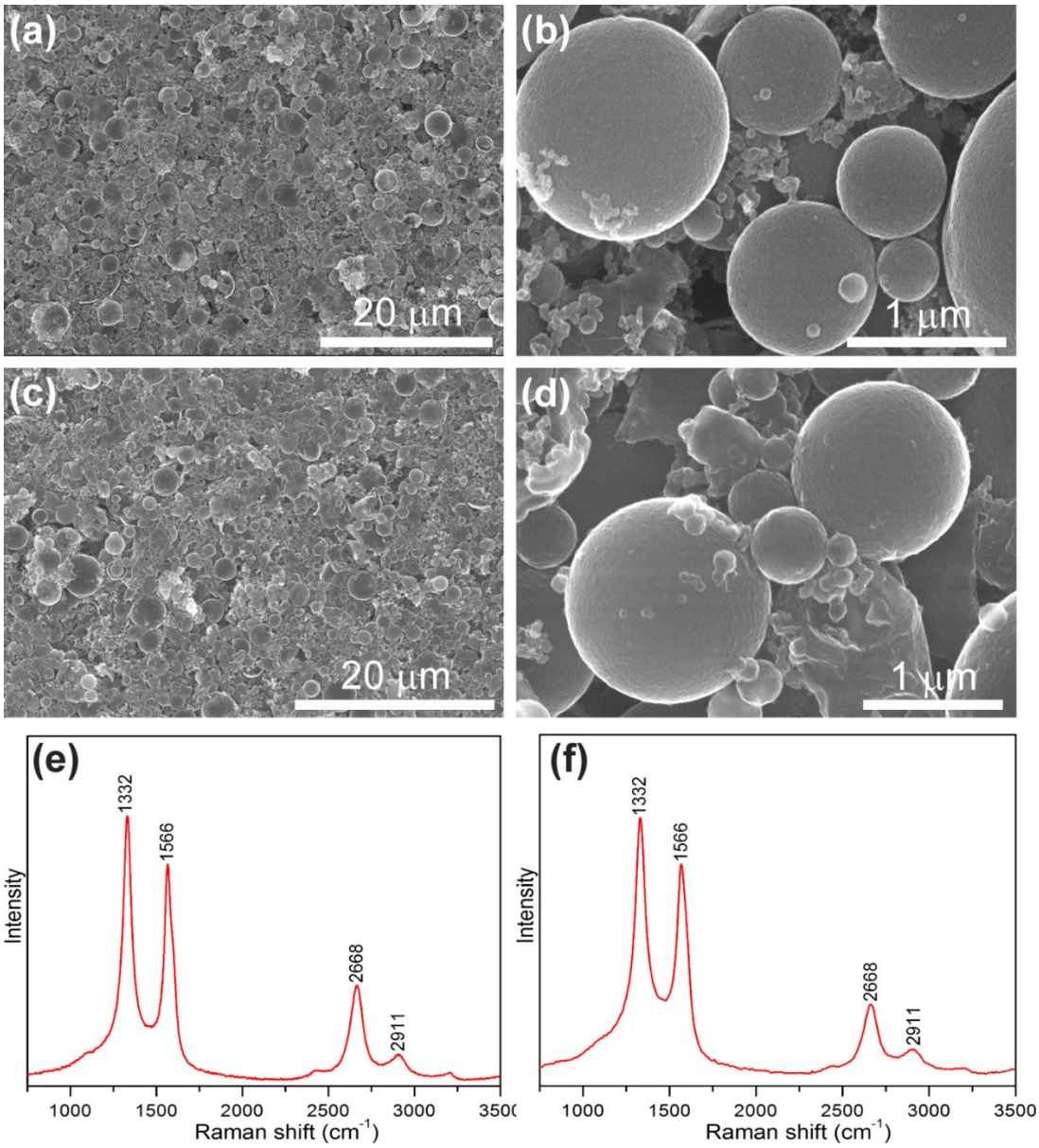

Figure 2.27 SEM images of porous carbon spheres annealed at 2300 ^{o}C (a, b) before cycling, (c, d) after 100 galvanostatic cycles. Raman spectrum of porous carbon spheres (annealed at 2300 ^{o}C) electrode (e) before cycling, and (f) after 100 galvanostatic cycles.

Structural stability of PCS-2300 during lithiation-delithiation process was examined by SEM and Raman spectral analysis of pristine and cycled carbon sphere electrodes. In the composite electrode, carbon spheres are connected together by super-P nanoparticles and

PVDF binder (Figure 2.27a,b), creating submicron-sized voids between individual spheres. The structural integrity of composite electrode and the morphology of individual carbon spheres retained after 100 galvanostatic cycles (Figure 2.27c,d). No significant amount of solid electrolyte interface (SEI) was observed on the carbon spheres, which might be due to the reduced reactivity of PCS-2300 due to low surface area, and uniform current distribution resulting from spherical morphology. For both pristine and cycled porous carbon sphere electrodes (PCS-2300), isoenergetic D, G, and 2D bands on Raman spectrums appeared at 1332 and 1566, and 2668 cm^{-1}, respectively (Figure 2.27e-f). D/G ratio were also unaffected by charge-discharge cycling. These results further demonstrated the excellent structural and electrochemical stability of carbon spheres during prolonged lithiation-delithiation cycles.

In summary, higher Li-ion storage electrochemical performance of carbon spheres were obtained due to its turbostratic crystal structure and slightly higher porosity than graphitic carbon. The higher reversible capacities for PCS-2300 compared to PCS-1200 can be attributed to its turbostratic structure, which may offer graphitic regions with dangling bonds that can act as additional sites for Li^+ adsorption. The disordered graphitic structure present in PCS-2300 also enable fast insertion of Li-ions to attain superior specific capacities at faster charge-discharge rates. Moreover, the porosity of the individual carbon spheres facilitates superior electrolyte contact, which reduces the interfacial charge transfer resistance, resulting in improved rate performance and long-term cycling stability. The inexpensive synthesis and superior Li-ion storage performance compared to commercial graphitic carbon anodes make the porous carbon spheres an excellent anode material for rechargeable Li-ion batteries.

2.6 Conclusions for Studies on Carbon Nanospheres

In summary, a metal salt catalyzed, solution-based spray pyrolysis synthesis technique was demonstrated able to create individual carbon nanospheres. The particle size could be easily adjusted from ~10 nm to several micrometers by changing the concentration of the precursors. By adjusting the ratio of carbon to metal salt precursors, hollow or solid nanospheres could be acquired without requiring templates. The study indicates that many kinds of metal salts can be used to form crystalline or amorphous oxides that act as nucleation sites and catalyze the formation of carbon nanospheres. After the removal of the metal oxides using acid or annealing at high temperature, porous-structure-carbon spheres with SSA as high as 1106 m^2/g are produced. These materials could be very promising for energy storage applications such as li-ion batteries and supercapacitors. The strong adsorption ability of the carbon nanospheres also makes them very promising as sorbents for water purification and environmental remediation.

3 SYNTHESIS OF POROUS CARBON FOAM AND THEIR APPLICAIONS

3.1 Introduction to Porous Carbon foam

Here a facile one-pot synthesis technique without pre-synthesis of any templates or catalyst was developed, which was able to achieve porous carbon foam with SSA up to 2340 m^2/g. The approach uses the direct pyrolysis of a sucrose and zinc nitrate mixture, with extremely quick (~ 5 min) reaction time and simple post-synthesis treatment. In this method, the zinc nitrate decomposes and generates gas to blow the melted sugar, similar to the role of ammonium salt in Wang's method.[29] The ZnO nanoparticles formed from the decomposition of zinc nitrate can also serve as an etchant during high temperature annealing[119] to further activate the carbon foam and create more porosity just as in Strubel's method.[21] However, the technique used here is not just the simple combination of the blowing effect from Wang's method and etching effect in Strubel's method. In this method, the nitrate could also act as an oxidizer to burn the sugar. Meanwhile, the ZnO nanoparticles also act as frames to prevent the collapse of the melted porous sugar during the carbonization process. Both of these two factors are critical and make it possible for the reaction to be finished quickly in one step within a few minutes, which, to the best of my knowledge, has not been reported before. Moreover, this technique also offers a way to quickly synthesize other metal or metal oxide/porous carbon composites for multiple applications. In this work, the role of ZnO and annealing temperature on the structure and SSA of the carbon foam were systematically studied. The materials were then evaluated as electrodes for supercapacitors in aqueous electrolyte and showed specific capacitances as high as 280 F/g at a current density of 0.1 A/g, higher than activated carbons and

nanocarbons such as carbon nanotubes and graphene, and still remained as high as 207 F/g even at a high current density of 10 A/g.

3.2 Experimental Details of Direct Pyrolysis and Post Treatment

To synthesize porous carbon foam, sucrose and $Zn(NO_3)_2.6H_2O$ (both from Alfa Aesar) were mixed with different weight ratios. Typically, 1 g sucrose and 2 g $Zn(NO_3)_2.6H_2O$ (1g:2g, same naming rule for other ratios) were put in a 100 mL beaker and slowly melted and mixed thoroughly to form a uniform viscous mixture using a hot place at 120 ^oC. Then the viscous mixture could be quickly carbonized and form carbon foam in about 5 minutes at ~180 ^oC on a hot plate or inside a box furnace. If using a hot plate, in order to heat the precursors more uniformly, a heat gun is recommended to heat the side of the beaker and make the entire mixture carbonized. If a box furnace were used, the reaction would be more uniform, since the temperature is more uniform. Due to the formation of NO_2 and NO_x gases, it is recommended to place the hot plate or box furnace in a fume hood with good ventilation.

High temperature annealing experiments were performed by heating the as-prepared carbon foam at 1200 ^oC in a tube furnace under N_2 gas flowing at 150 sccm for 2 h. For some samples, a graphite furnace (GT Thermal Technologies Inc, Model: 1050CG) was used to anneal the samples at up to 2300 ^oC for 2 h in Ar. In some samples where the annealing temperature was not hot enough to reduce ZnO, the ZnO was etched with HCl, followed by thorough washing with DI water and drying.

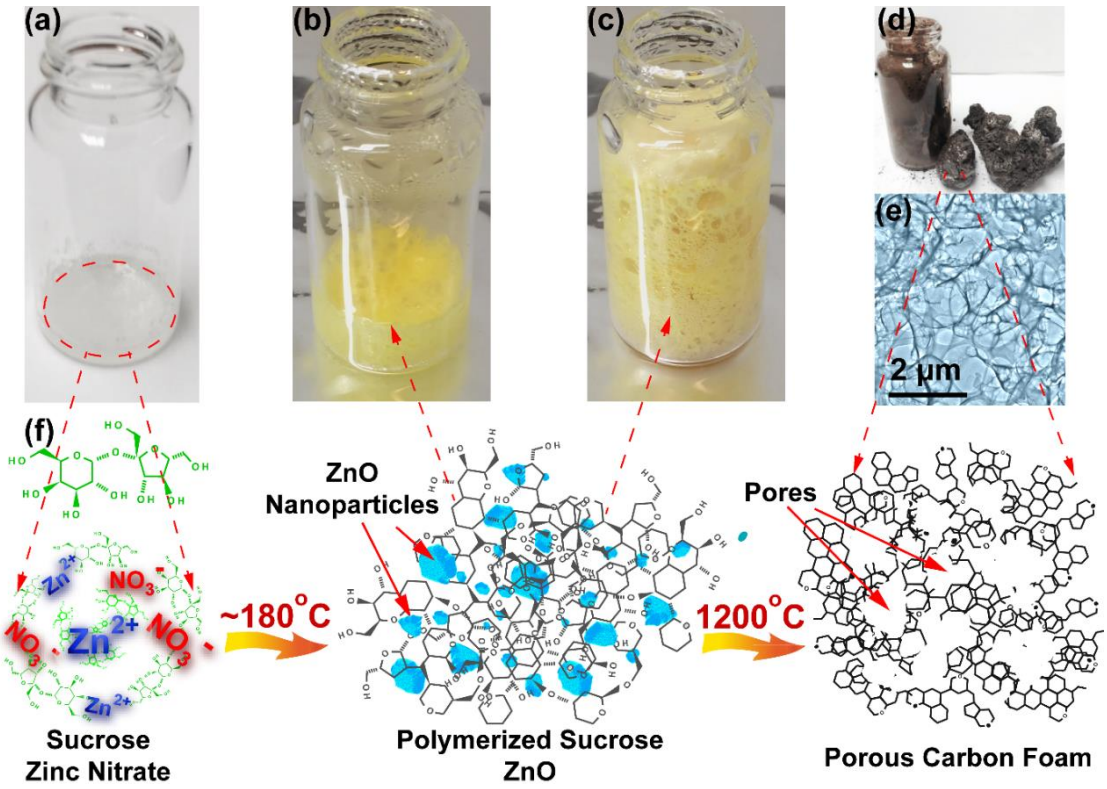

Figure 3.1 Synthesis process and schematic illustration of carbon foam. a-e) Different stages of the synthesis process: a) the starting mixture of sucrose and zinc nitrate precursors (0.5 g sucrose and 1g zinc nitrate shown in picture); b,c) the precursors start reacting at ~ 180 ^{o}C, with the zinc nitrate decomposing to ZnO and formation of gases that cause the melted sucrose to blow into a foam-like structure; d) the carbon foam after further annealing at high temperature; e) typical TEM image of carbon foam annealed at 1200 ^{o}C; f) The molecular schematic illustration for the corresponding steps.

As Figure 3.1 shows, the synthesis of carbon foam could be achieved through the direct reaction of a sucrose and zinc nitrate mixture in a few minutes. Sucrose and zinc nitrate were first slowly melted and mixed uniformly at a relative low temperature (~120 ^{o}C) (Figure 3.1a). The initiation of the carbonization process was characterized by a color change in the mixture to yellow (Figure 3.1b) corresponding to the formation of NO_2

from decomposition of $Zn(NO_3)_2$ when the temperature was increased to ~180 ^oC. The reaction then proceeded according to the general process:

$$C_{12}H_{22}O_{11} + Zn(NO_3)_2 \cdot 6H_2O \xrightarrow{\sim 180\ ^\circ C} C_{foam} + ZnO + N_2 \uparrow + H_2O \uparrow + NO_x \uparrow + CO_2 \uparrow$$

where $Zn(NO_3)_2.6H_2O$, a strong oxidizer, decomposed and reacted with sucrose to generate gases (N_2, NO_x, CO_2, *etc.*), which acted to blow the melted viscous sugar and cause it to swell (Figure 3.1b,c).

Meanwhile, the sucrose would dehydrate and polymerize, resulting in the mixture to change to a brown color and form a foam-like composite containing embedded ZnO nanoparticles (Figure 3.1f). After the reaction was completed, the ZnO nanoparticles could be removed using acid or through further annealing at high temperatures. ZnO can be reduced by carbon at 900 ^oC[119] according to the following reaction:

$$xC + ZnO \xrightarrow{>900\ ^\circ C} (x-1)C + Zn + CO$$

and then the resulting zinc can evaporate, leaving the black colored porous carbon foam behind (Figure 3.1e,f).

Thermogravimetric analysis (TGA) was used to further confirm the reactions. Heating a carbon foam prepared from 1 g sucrose and 2 g $Zn(NO_3)_2.6H_2O$ (1g:2g carbon foam) in either N_2 or air resulted in the weight loss and differential thermogravimetric curves shown in Figure 3.2. The weight loss peak at around 250 ^oC for both samples corresponds to the decomposition of residual $Zn(NO_3)_2.6H_2O$. The sample started burning in air and showed a weight loss peak at around 380 ^oC. For the sample annealed in N_2, the sugar kept carbonizing and showed weight loss until 500 ^oC. Then, the weight decreased slowly from 500 ^oC to 800 ^oC, which might be caused by the slow reaction between carbon and

the ZnO nanoparticles. The weight loss peak around 900 ^{o}C is from the carbothermal reduction of ZnO[119] as described by Eq. (2).

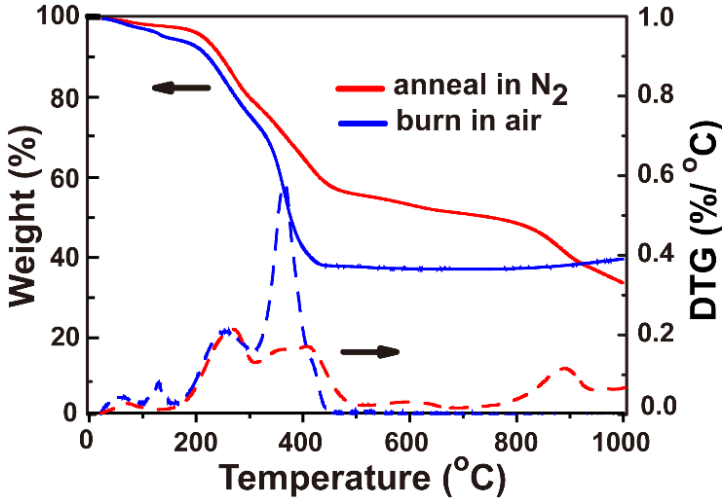

Figure 3.2 TGA results for 1g:2g carbon foam annealed in N_2 (red) and burning in air (blue).

3.3 The Effect of Precursor Ratio on Morphology and Specific Surface Area of Carbon Foam

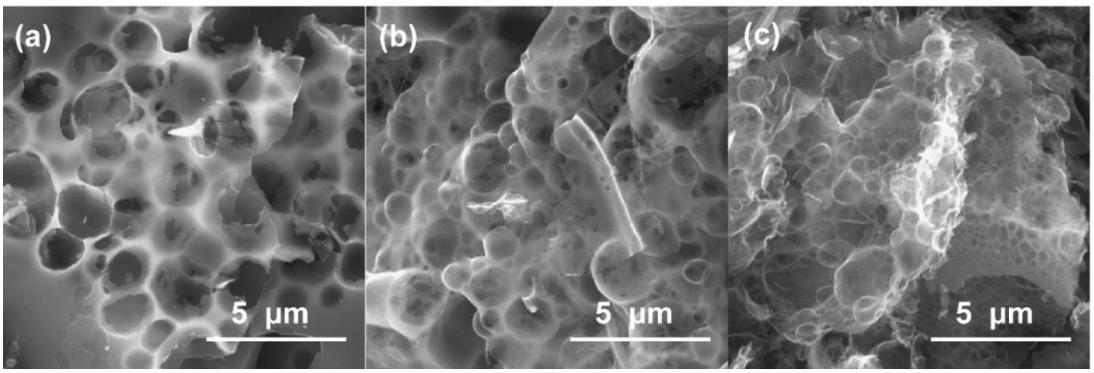

Figure 3.3 SEM images of carbon foam after annealing at 1200 ^{o}C for 2 h made from different sugar to $Zn(NO_3)_2.6H_2O$ ratio. a) 1g:1g; b) 1g:2g; c)1g:3g.

Typical scanning electron microscopy (SEM) images of the carbon foams are show in Figure 3.3. It can be seen clearly that by increasing the amount of $Zn(NO_3)_2.6H_2O$ in the precursor, the carbon foam became more porous and had more smaller pores. This could be from the increased amount of gas (N_2, NO_x, CO_2, *etc.*) generated from the decomposition of $Zn(NO_3)_2.6H_2O$ and the carbonization of sugar, which could form bubbles in the molten sugar, as seen by the morphology of the carbon foam. Moreover, the additional ZnO nanoparticles can also etch more carbon[119] and form more pores at high temperatures.

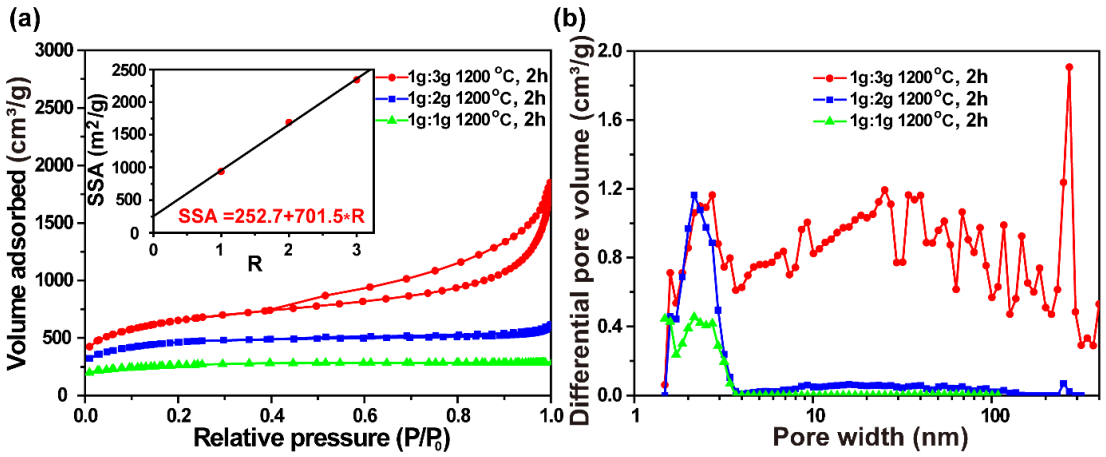

Figure 3.4 a) N_2 adsorption-desorption isotherms of carbon foam made from different sugar to $Zn(NO_3)_2.6H_2O$ ratio and annealed at 1200 ^oC for 2 h, the inset plots the SSA against the grams of $Zn(NO_3)_2.6H_2O$ used (R) with 1 g sugar in the precursor; b) the corresponding pore size distributions calculated using the DFT method.

In order to further study the effect of the sugar to $Zn(NO_3)_2.6H_2O$ ratio on the SSA of carbon foam, N_2 adsorption-desorption isotherms measurements were conducted on three carbon foam samples with different precursor ratios. Calculated from the curves shown in

Figure 3.4a, the SSAs of the 1g:1g, 1g:2g, 1g:3g carbon foams annealed at 1200 ºC for 2 h were around 937 m^2/g, 1690 m^2/g, and 2340 m^2/g, respectively, indicating that the higher the amount of $Zn(NO_3)_2.6H_2O$ in the precursor solution, the higher the SSA of the resulting carbon foam. When plotting the SSA against R, where R is the mass of $Zn(NO_3)_2.6H_2O$ (g) used to 1 g of sugar, there is a linear relationship. Specifically, it can be observed that the SSA increased around 700 m^2/g when the amount of $Zn(NO_3)_2.6H_2O$ increased 1 g relative to the amount of sugar. Also, the *y*-intercept, where R equals zero, is around 252 m^2/g, which corresponds to the SSA of carbon foam derived from carbonization of pure sucrose without any zinc nitrate, as reported in the literature.[155] This further confirms the contribution of $Zn(NO_3)_2.6H_2O$ to increase the SSA of the carbon foams. As shown in Figure 3.4a, the 1g:1g carbon foam had a type I isotherm with almost no hysteresis, while the 1g:2g carbon foam starts to show a little hysteresis but still kept the type I shape, indicating its microporous structure. However, the 1g:3g carbon foam showed a type IV isotherm with large hysteresis, which indicates that it contains mesoporosity.[106] The pore size distributions calculated using density function theory (DFT)[156] also showed the pore size changes with increasing $Zn(NO_3)_2.6H_2O$ in the precursor (Figure 3.4b). Specifically, the pore size distributions in the 1g:1g carbon foam are mainly between 2-3 nm, while the 1g:2g carbon foam starts having some pore size between 10-100 nm. For the 1g:3g carbon foam, however, the mesopores between 5-400 nm in size become significant.

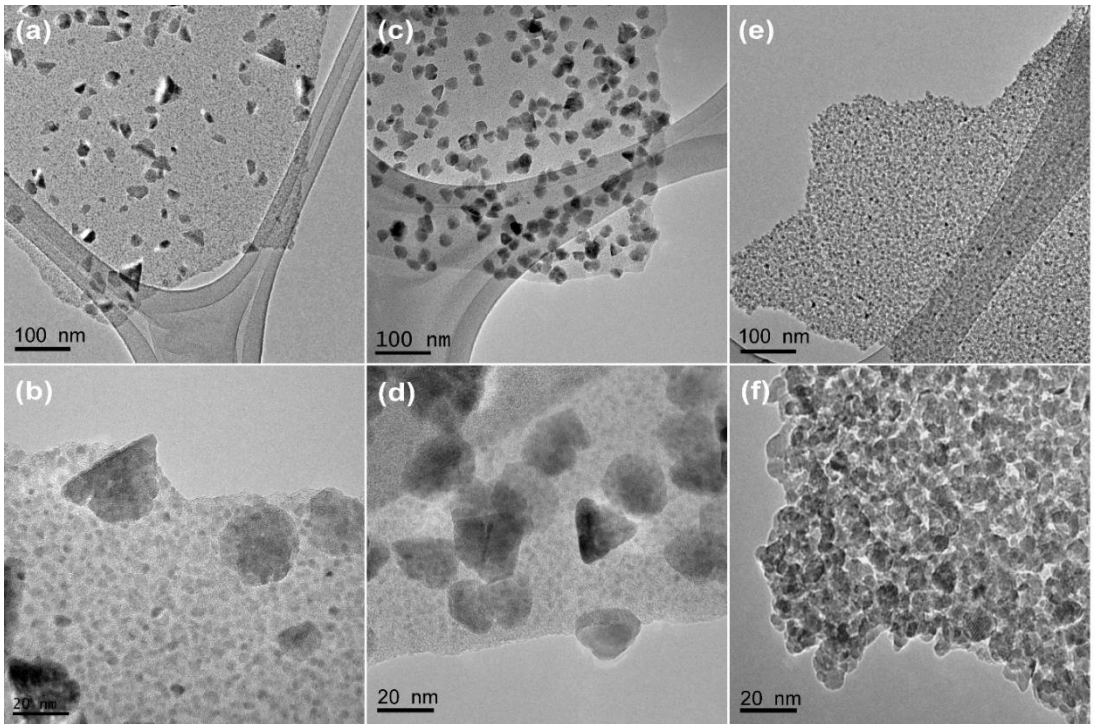

Figure 3.5 TEM images at different magnifications of carbon foams made from different sugar to $Zn(NO_3)_2.6H_2O$ ratios and carbonized at 350 ^oC for 30 min. a,b) 1g:1g, c,d) 1g:2g, e,f) 1g:3g.

These features could be further explained by the transmission electron microscopy (TEM) images (Figure 3.5) of the as-made carbon foams that were heated at 350 ^oC for 30 min. At this point, most of the sugar was carbonized but ZnO had not been reduced by carbon yet. The carbon adopted a sheet-like morphology and the ZnO nanoparticles could be found interdispersed within. The ZnO nanoparticles in both the 1g:1g and 1g:2g carbon foam mainly had two sizes. The smaller particles with around 5 nm size were found embedded in the carbon matrix surrounding the bigger particles around 20 nm in size. In the 1g:1g carbon foam (Figure 3.5a,b), the majority of the ZnO nanoparticles were around 5 nm. However, the bigger particles became significant in the 1g:2g carbon

foam (Figure 3.5c,d). This explains why the 1g:1g carbon foam has a type I isotherm with almost no hysteresis, while the isotherm of the 1g:2g carbon foam starts having the hysteresis feature. The ZnO nanoparticles in the 1g:3g carbon foam are mainly around 10 nm instead of differentiating into two sizes. Moreover, the ZnO nanoparticles are so crowded and interconnecting with each other that the carbon phase no longer looks like a matrix (Figure 3.5e,f). The aggregation of ZnO nanoparticles makes the 1g:3g carbon foam mesoporous and have a type IV isotherm.

3.4 The Role of ZnO on the Specific Surface Area of Carbon Foam

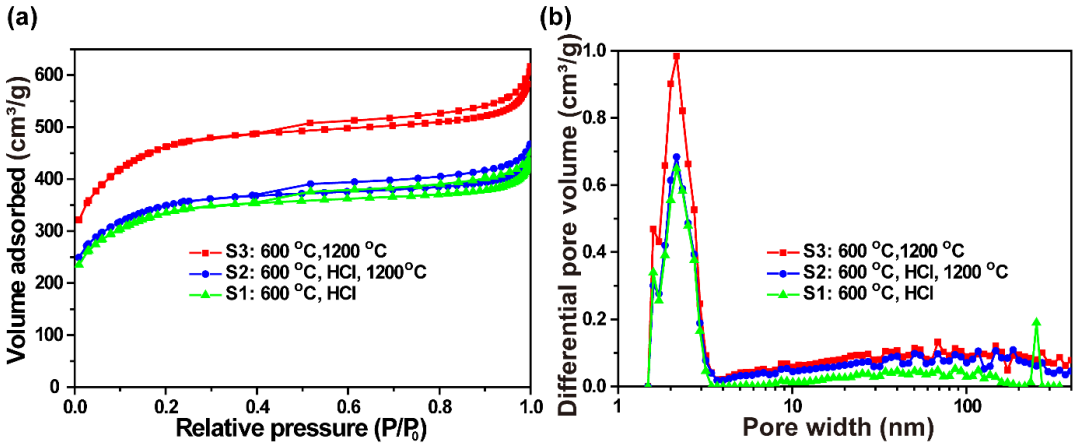

Figure 3.6 a) N_2 adsorption-desorption isotherms of 1g:2g carbon foam treated with different conditions. Sample S1 was annealed at 600 ^oC for 2 h then treated with HCl to remove ZnO; sample S2 was made from S1 by further annealing at 1200 ^oC for 2 h; sample S3 was annealed at 600 ^oC for 2 h and then further annealed at 1200 ^oC for 2 h without removing ZnO with HCl. b) the corresponding pore size distributions calculated using the DFT method.

In order to study the contribution of ZnO to the SSA at high temperature, three 1g:2g carbon foam samples treated with different annealing conditions were characterized with

N_2 adsorption-desorption isotherms. Specifically, after the synthesis, all three samples were heated at 600 ^oC for 2 h, where most of the carbon source changed to carbon but had not reacted with ZnO nanoparticles. For samples S1 and S2, the ZnO was removed with HCl acid and washed with DI water thoroughly. Sample S1 had no further treatment while S2 was further annealed at 1200 ^oC. Sample S3 was annealed at 1200 ^oC directly without removing ZnO beforehand with HCl. Based on the N_2 adsorption-desorption isotherms (Figure 3.6a), the SSAs of S1 and S2 were 1211 m^2/g and 1268 m^2/g, respectively, indicating that further annealing at 1200 ^oC did not change the SSA much once the ZnO was removed. However, the SSA of S3 was 1674 m^2/g, around 400 m^2/g more than that of S1 and S2, revealing that the presence of ZnO can lead to higher SSA after annealing at 1200 ^oC due to the ability of ZnO to etch carbon. The pore size distribution also reveals that from S1 to S2, further annealing at 1200 ^oC did not have much change on the amount of micropores, but caused a small increase in the mesopore volume. However, the etching effect caused by ZnO nanoparticles at high temperatures makes the differential pore volume peak increase by about one third in the micropore region.

3.5 The Effect of Annealing on the Specific Surface Area of Carbon Foam

For porous carbon materials, since the annealing temperatures can significantly change the pore volume, bond structures, and surface functional groups, they have a great influence on both the SSA[157–159] and carbon electronic conductivity,[158–162] which are two critical factors for carbon materials in many applications, especially as electrode materials. For this reason, the effect of annealing temperatures on the structure of carbon foam was systematically studied so that good conductivity in the carbon foam could be

achieved by annealing the samples at higher temperatures, while still keeping the SSA relatively high. According to the N_2 adsorption-desorption isotherms of 1g:2g carbon foams shown in Figure 3.7a, when the temperature was increased from 1200 ^oC to 1500 ^oC, the SSA remained almost the same and then started to decrease from 1690 m^2/g to 1265 m^2/g when the temperature was further increased to 1800 ^oC. For the sample annealed at 2300 ^oC, the SSA had only 62 m^2/g remaining.

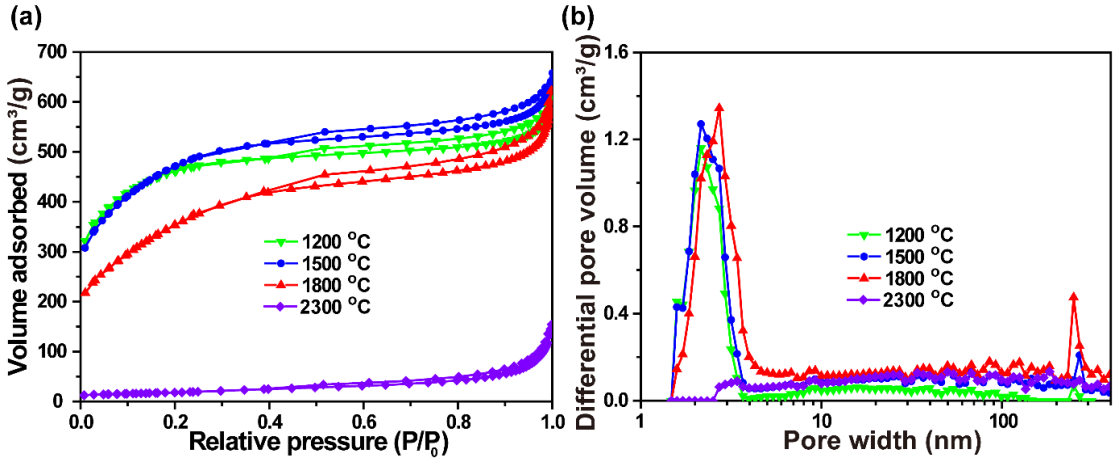

Figure 3.7 a) N_2 adsorption-desorption isotherms of the 1g:2g carbon foam annealed at different temperatures: 1200 ^oC, 2 h (green); 1500 ^oC, 2 h (blue); 1800 ^oC, 2 h (red); 2300 ^oC, 2 h (violet), b) the corresponding pore size distributions calculated using the DFT method.

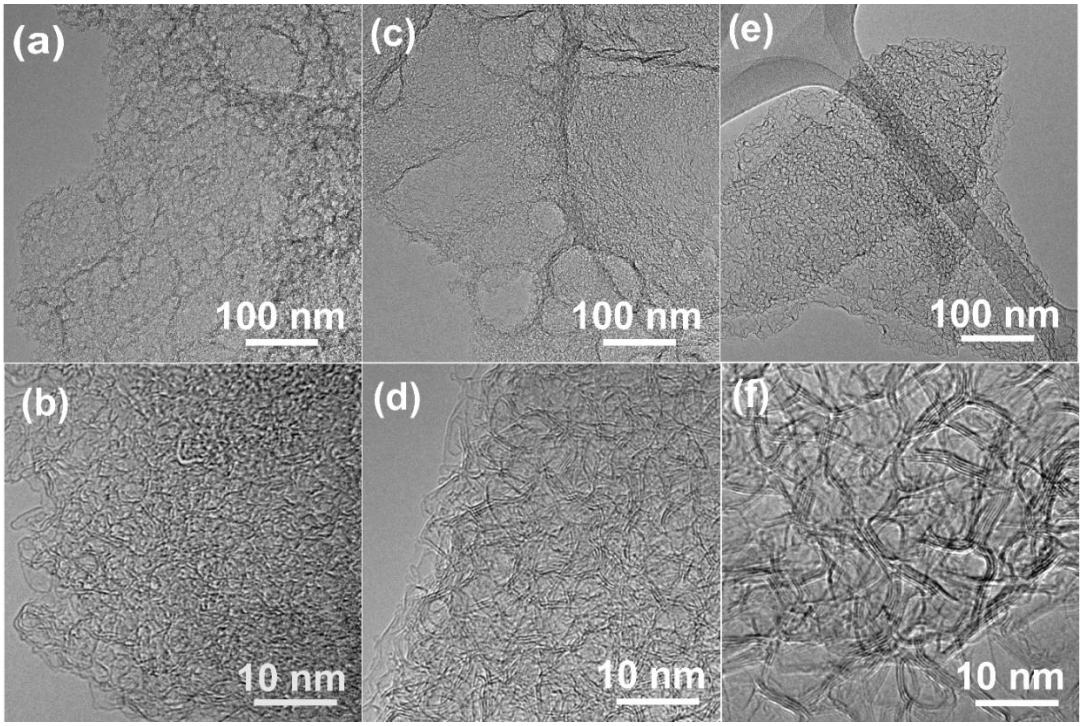

Figure 3.8 TEM images of carbon foam. a,b) 1:2 CF annealed at 1200 ^{o}C for 2 h; c,d) 1:2 CF annealed at 1800 ^{o}C for 2 h; e,f) 1:2 CF annealed at 2300 ^{o}C for 2 h.

To understand this decrease in SSA after high temperature annealing, TEM was used to study the structural changes in the carbon foam. As shown in the TEM images in Figure 8, when the annealing temperature increased, the carbon foam started to crystallize and its surface became smoother. For the sample annealed at 1200 ^{o}C, the surface of the carbon foam sheet was very rough (Figure 3.8a), while the structure was mostly amorphous, with only one to two layers of graphitic structure (Figure 3.8b). When the samples were annealed at 1800 ^{o}C (Figure 3.8c,d) and 2300 ^{o}C (Figure 3.8e,f), the surfaces of the foam sheets became smoother, and the structures became more crystalline. The sample annealed at 1800 ^{o}C had two to three graphitic layers while the one annealed at 2300 ^{o}C had three or more layers. These results indicate that the crystallization process

may cause the coalescence or closing of the small pores and lead to the decrease of SSA, which also changes the pore size distribution (Figure 3.7b). According to Figure 3.7b, the pores in the microporous region shifted to larger size when the annealing temperatures increased from 1200 ^{o}C to 1800 ^{o}C, while the volume of pores in the mesoporous region became higher. When the temperature further reached 2300 ^{o}C, the volume of the smallest pores in the microporous region became negligible.

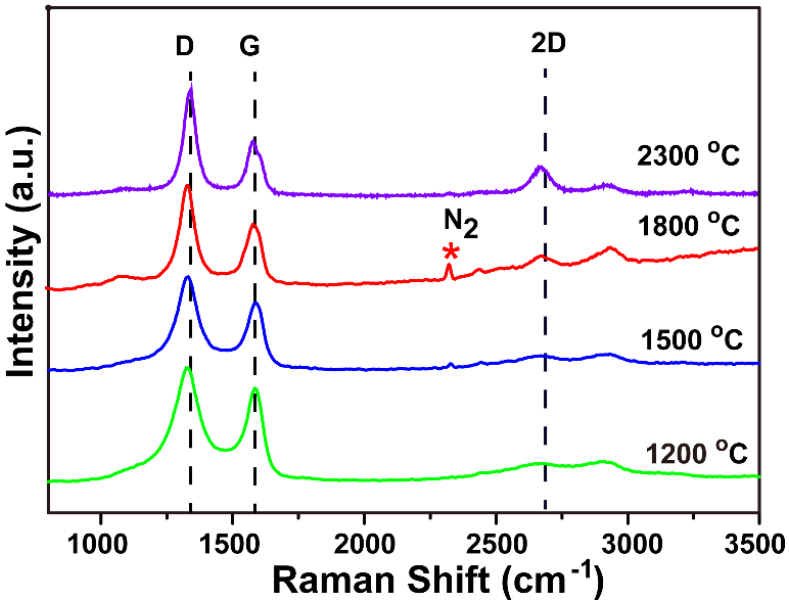

Figure 3.9 Raman spectra of 1g:2g carbon foam annealed with different temperatures: 1200 ^{o}C, 2h (green); 1500 ^{o}C, 2h (blue); 1800 ^{o}C, 2h (red); 2400 ^{o}C, 2h (violet). The asterisk denotes N_2 adsorbed from the air during the spectrum acquisition.

The Raman data shown in Figure 3.9 also confirm that the carbon foam started to crystallize above 1500 ^{o}C, since the 2D band at ~2680 cm^{-1} relating to the stacking order of the graphitic structure along the *c*-axis[103] became more significant for samples annealed at 1800 ^{o}C and 2300 ^{o}C. Moreover, both the D band at ~1360 cm^{-1} attributed to defect and disorder[122] and the G band at~1590 cm^{-1} corresponding to the sp^2 carbon

network[103,104] became sharper as the annealing temperature increased, which means the high temperature annealing made the carbon more graphitic. Meanwhile, the curvature of the graphitic sheets might introduce more defects, which is consistent with the TEM result (Figure 3.8 d,f).

3.6 Electrochemical Performance of the Carbon Foams as Supercapacitor Electrodes

3.6.1 Electrochemical Measurement Details

The carbon foam powder was put onto stainless steel discs (1.5 cm diameter) directly without any binder or carbon black to make a ~0.5 mg/cm^2 electrode. For the carbon foams annealed at 1200 ^{o}C, in order to improve the wetting with the electrolyte, the carbon foam was mixed in a slurry with conducting carbon black (10 wt%), polyvinylidene fluoride (PVdF, 10 wt%), and N-Methyl-2-pyrrolidone (NMP) and coated onto the stainless steel discs as a film. Then two identical electrodes were assembled into a coin cell with Whatman filter paper as separator and 1 M H_2SO_4 as the electrolyte. The coin cell was sealed with around 1200 psi of pressure. A two-electrode set up was used to measure the performance of the supercapacitors using cyclic voltammetry with a BioLogic VMP3 potentiostat from -0.5 V to 0.5 V. The specific capacitance was calculated from the galvanostatic charge-discharge curves. Electrochemical impedance spectroscopy (EIS) was conducted at open circuit voltage in the frequency range of 1 Hz to 100 kHz with a 5 mV AC amplitude.

3.6.2 Electrochemical Performance

For the batch of carbon foams used for the supercapacitor test, the as-made 1g:3g carbon foams were annealed at 600 ^{o}C for 5 h under N_2 atmosphere (designated as 1g:3g 600 ^{o}C). Then the ZnO was etched with HCl, followed by washing with DI water and

drying at 300 °C. The 1g:3g 700 °C or 800 °C carbon foams were obtained from the 600 °C foams by further annealing at 700 °C or 800 °C for 1 h, respectively.

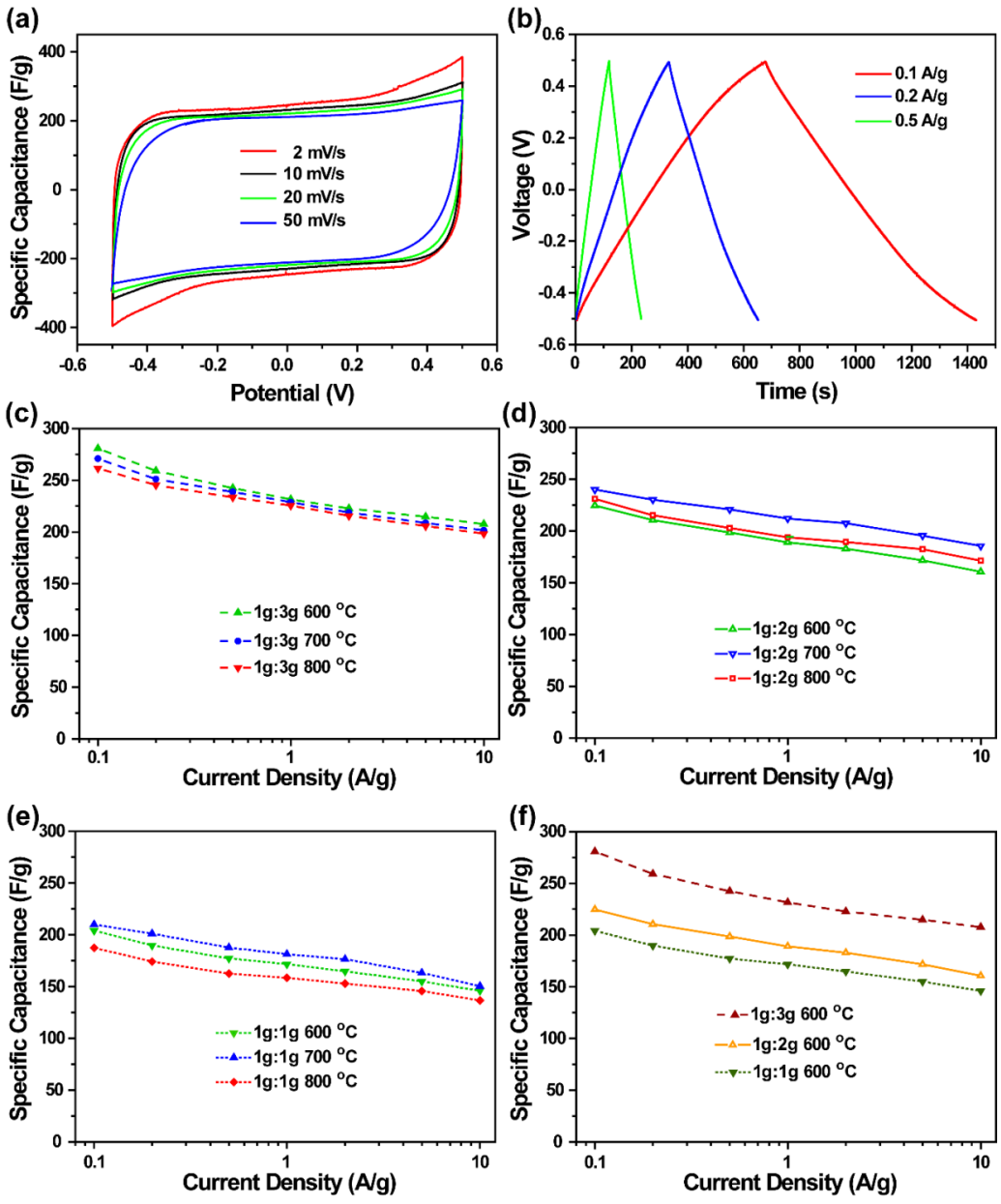

Figure 3.10 Performance of supercapacitors with carbon foams electrodes in 1 M H_2SO_4 aqueous electrolyte. a) CV curves obtained at different scan rates for supercapacitors made from 1g:3g 600 °C carbon foam. b) Galvanostatic charge/discharge curves of supercapacitors made from 1g:3g 600 °C carbon foam at different current densities. The

specific capacitances of supercapacitors made from 1g:3g (c), 1g:2g (d), and 1g:1g (e) carbon foams treated with different temperatures at different current densities. f) The specific capacitances of supercapacitors made from 1g:3g, 1g:2g, and 1g:1g carbon foams annealed at 600 ^{o}C at different current densities.

Figure 3.10a shows the typical cyclic voltammetry (CV) curves of supercapacitors made from 1g:3g 600 ^{o}C and Figure 3.10b shows the galvanostatic charge/discharge curves taken at different current densities. Similar galvanostatic tests were performed on samples with different precursor ratios and annealing temperatures. The specific capacitances of the samples treated with different conditions are shown in Figure 3.10c-f determined by fitting the slope of the linear part of the discharge curve. The specific capacitance was as high as 280 F/g for the 1g:3g 600 ^{o}C carbon foam at a current density of 0.1 A/g, with 207 F/g still remaining even when the current density increased to 10 A/g (Figure 3.10c).

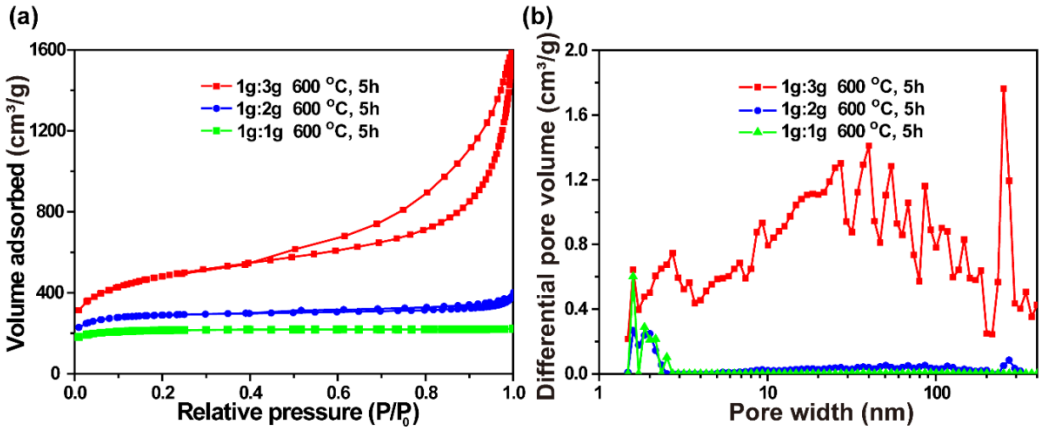

Figure 3.11 a) N_2 adsorption-desorption isotherms of carbon foam made from different sugar to $Zn(NO_3)_2.6H_2O$ ratio and annealed at 600 ^{o}C for 5 h, b) the corresponding pore size distributions calculated using the DFT method.

The other combinations of precursor ratio and annealing temperature showed lower specific capacitances. When the post treatment temperature was held constant (e.g. 600 ^{o}C), the specific capacitance increased with the ratio of $Zn(NO_3)_2.6H_2O$ in the precursor mixture (Figure 3.10f), as expected since the SSA increased with the ratio of $Zn(NO_3)_2.6H_2O$. Calculated from the N_2 adsorption-desorption isotherms shown in Figure 3.11a, the SSAs for 1g:1g, 1g:2g, and 1g:3g carbon foams annealed at 600 ^{o}C were 788 m^2/g, 1069 m^2/g, and 1731 m^2/g, respectively. Although the SSAs were lower than those of corresponding carbon foams annealed at 1200 ^{o}C with ZnO nanoparticles, the shape of the N_2 adsorption-desorption isotherms and the pore size distribution curves were similar with those shown in Figure 3.4.

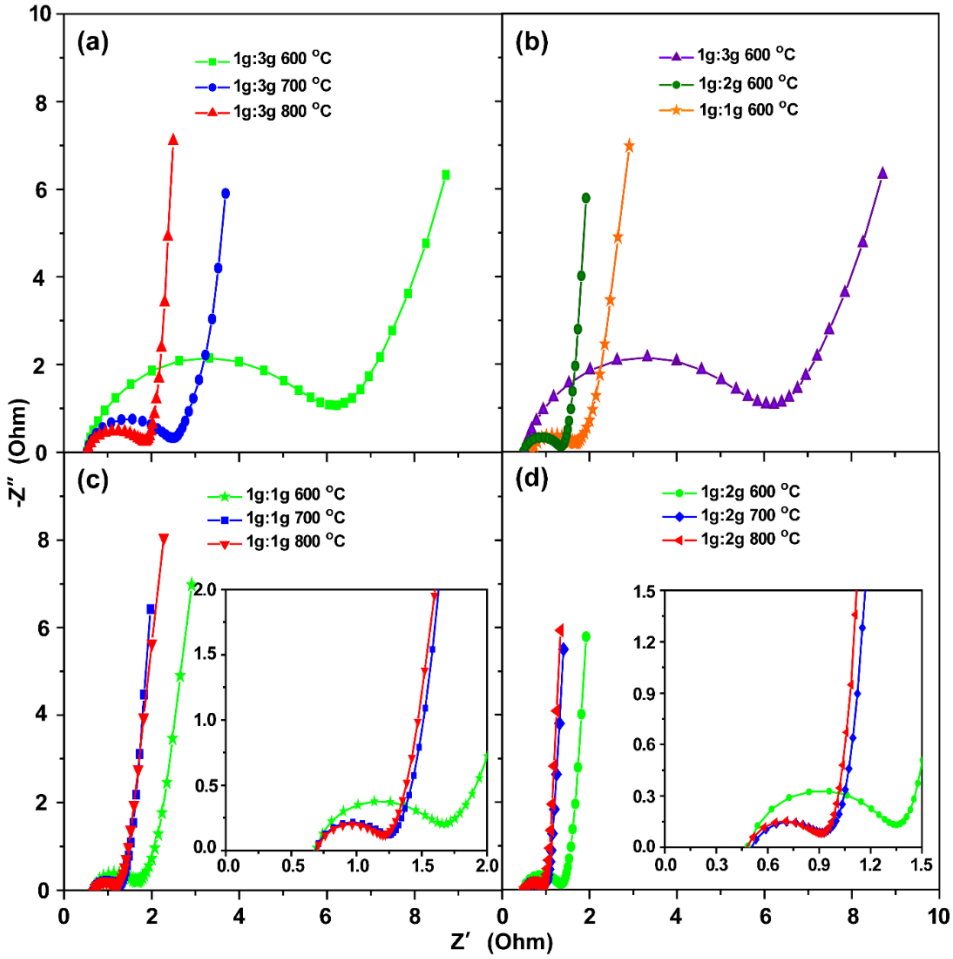

Figure 3.12 EIS measurement of supercapacitors made of different carbon foams annealed with different temperatures. a) 1g:3g carbon foams; b) carbon foams with different precursor ratio annealed at 600 ^{o}C; c), d) 1g:1g, and 1g:2g carbon foams, the insets are the zoom-in view of the high frequency region.

According to previous studies, the annealing temperature has an influence on the carbon surface functional groups, especially oxygenated groups,[158–163] which directly relate to the wettability of the carbon surface with the electrolyte. With the removal of oxygenated surface groups at higher temperatures, the carbon is expected to have less wettability with the aqueous electrolyte. The annealing temperature also affects the carbon conductivity dramatically, especially in the range between 600 ^{o}C to 800 ^{o}C,[158–161] where the conductivity can increase one order of magnitude or more. This change could also be seen from the EIS measurement in Figure 3.12. In the Nyquist plots, the intercept with the real axis at high frequency represents the ohmic resistance including the resistance of the electrode materials, electrolyte, and the contact resistance. The ohmic resistance was similar for all of the different samples. Amongst each batch of carbon foam prepared with the same precursor ratio, the charge transfer resistance R_{ct}, represented by the semicircle regions, decreased when the annealing temperature increased, especially from 600 ^{o}C to 700 ^{o}C. Specifically, the 1g:3g carbon foams (Figure 3.12a) have much larger resistance than the 1g:1g (Figure 3.12c) and 1g:2g (Figure 3.12d) carbon foams at different temperatures. Figure 3.12b compares the Nyquist plots for the carbon foams with different precursor ratios annealed at 600 ^{o}C. Since the 1g:3g carbon foams are more porous and have more large pores (Figure 3.11b), the contact resistance between the carbon foam particles is more significant than that of the less porous 1g:2g

and 1g:1g carbon foams. The difference in the pore structure as a result of the three carbon foam precursor ratios also causes the change of carbon conductivity to have a different influence on the capacitance performance when combined with other factors, as the following discussion. Considering that these two factors can affect the capacitance properties of the carbon, the performance of the supercapacitors made from all three types of carbon foams treated with three different temperatures (600 ^{o}C, 700 ^{o}C, and 800 ^{o}C) was studied and shown in Figure 3.10c-e.

As Figure 3.10c shows, the specific capacitances of the 1g:3g carbon foams kept decreasing when the annealing temperature increased from 600 ^{o}C to 800 ^{o}C, despite the fact that the carbon conductivity has increased (Figure 3.12a). Since the ultrahigh SSA (1731 m^2/g, Figure 3.11a) and mesoporous structure (Figure 3.11b) indicate a high contact area with the electrolyte, this shows that temperature-dependent changes on the interfacial properties of the carbon foam (e.g. wettability) outweigh the effect of changes on the carbon conductivity. However, for both 1g:1g and 1g:2g carbon foams, since the SSAs are much lower than that of 1g:3g carbon foam and the pores are mainly micropores, the maximum specific capacitance obtained at 700 ^{o}C should be due to the significant increase of the carbon conductivity[158–161] (Figure 3.12c,d) and the increase in the pore sizes (Figure 3.6b and Figure 3.7b). The specific capacitances started decreasing at 800 ^{o}C (Figure 3.10d,e), even though the conductivity was slightly better than that of the carbon foam annealed at 700 ^{o}C (Figure 3.12c,d). This could be due to the surface dewetting from to the loss of the oxygenated goups.[158,160,161] A similar phenomenon showing a dependence of the specific capacitance on the annealing temperature was also reported on other porous carbons recently.[22]

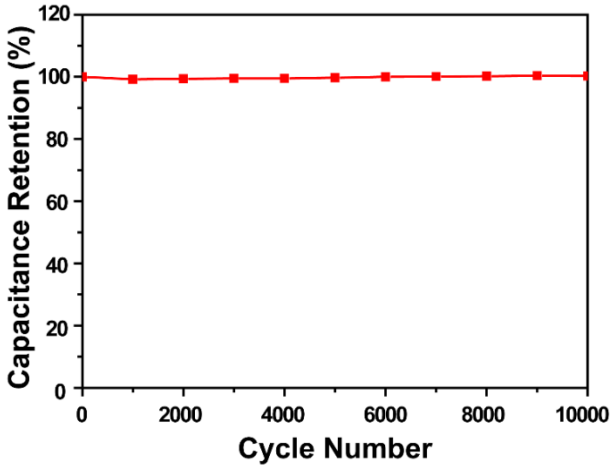

Figure 3.13 Cycle life of supercapacitor made with 1g:2g 700 ^{o}C carbon foam at a current density of 10 A/g.

The supercapacitor made with 1g:2g 700 ^{o}C carbon foam was used to study the cycle performance. The capacitance retention remained at 100% (Figure 3.13) after 10,000 charge/discharge cycles at a current density of 10 A/g, which demonstrates very good long-term stability.

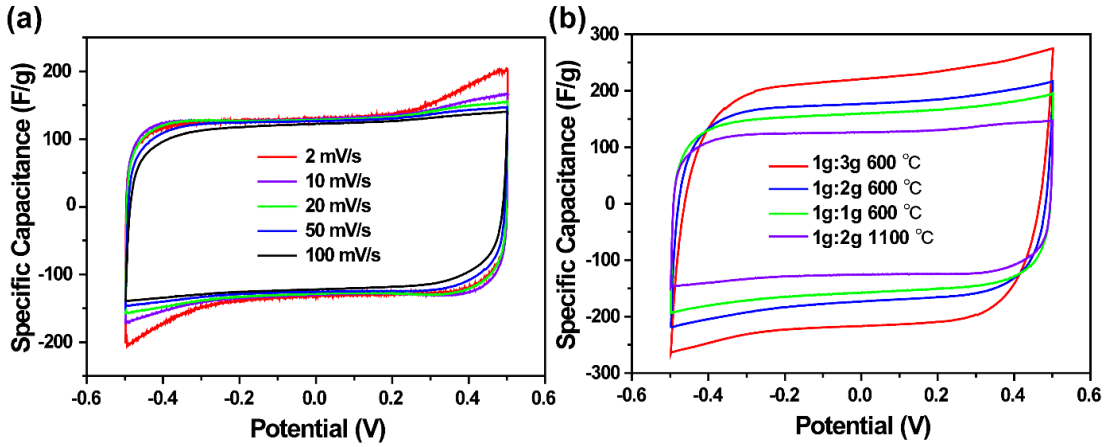

Figure 3.14 a) CV curves obtained at different scan rates for supercapacitor made from 1g:2g carbon foam annealed at 1200 ^{o}C with ZnO nanoparticles for 2 h. b) CV curves obtained at scan rate of 50 mV/s for supercapacitors made of different carbon foams.

To further study the influence of the wettability of the carbon foam surface on the specific capacitance, a 1g:2g carbon foam annealed at 1200 ^{o}C with ZnO nanoparticles for 2 h was used to test the performance as supercapacitor electrodes. Due to the etching effect of ZnO nanoparticles at high temperature, the SSA was as high as 1690 m^2/g (Figure 3.7a), much higher than that of 1g:2g 600 ^{o}C carbon foam, 1069 m^2/g (Figure 3.11a). Moreover, the carbon conductivity also improved a lot, as seen by the rectangular shape of the CV curves (Figure 3.14a). However, due to the bad wettability, the capacitance was not as good as expected. The specific capacitance was only around 125 F/g at a 50 mV/s scan rate, while the one for the 1g:2g 600 ^{o}C carbon foam was as high as around 175 F/g at same scan rate (Figure 3.14b). The results reveal that in aqueous electrolyte, the wettability could be the dominant factor on the performance of the carbon foam-based supercapacitors.

From these results, it can be seen that the carbon foams can act as high capacitance supercapacitor electrodes, with a specific capacitance as high as 280 F/g at a current density of 0.1 A/g, which is higher than most values reported for carbon nanotubes (50-100 F/g),[135] graphene (100-250 F/g),[5,7] and activated carbon (100-200 F/g).[24,48,135]. The carbon foam performance is comparable with the recently demonstrated three-dimensional strutted graphene (250 F/g, at 0.5 A/g),[29] KOH activated porous carbon nanosheets (300 F/g, at 0.5 A/g),[23] and even nitrogen doped KOH activated porous carbon (300 F/g, at 0.1 A/g).[164] However, the synthesis method to achieve the highly porous carbon foam is simple and does not require doping or pre-synthesized templates or particles.

3.7 Conclusions

In summary, a facile one-pot technique able to fabricate foam-like porous carbon have been developed without pre-synthesizing any hard templates or precursors. By simply adjusting the ratio of sugar to $Zn(NO_3)_2.6H_2O$, the carbon foams with different SSAs and pore size distribution can be easily achieved at a large scale. Due to the unique roles that ZnO nanoparticles act during the synthesis and post annealing stages, a high SSA up to 2340 m^2/g is obtained. The excellent electrochemical performance of the carbon foam makes it very promising for potential applications as electrode materials in the energy storage field. Moreover, the unique properties and the scalable synthesis make these novel carbon foams suitable for many other applications, such as sorbents and catalyst supports.

4 BIMORPH ACTUATORS

4.1 Introduction to Bimorph Actuators

In this work. the facile fabrication of printed active origami (PAO) was developed using common plastic films and coatings of single-walled carbon nanotubes. A walking robot was made from a common plastic sheet coated with conductive inks. The conductive inks were printed onto plastic films, then cut with scissors, folded into a desired shape and activated by on-board, circuitry. The solid-state actuators are multifunctional energy transducers powered by heat, light, or electricity. The maximum observed force produced by an actuator was 60x its own weight. Actuators were also demonstrated to bend more than 90 degrees. The actuators were repeatedly activated for nearly 50,000 cycles without significant loss of performance for a sub-hertz actuator and 1,000,000 cycles in the case of a 30 Hz actuator.

The actuation of the thermal bimorph actuators can be described by the thermal expansion of the polymer film during Joule heating of the CNT/polymer composite film. The bending is caused by the high van der Waals adhesion between the CNTs and polymer, and the roughly 2 orders of magnitude lower thermal expansion coefficient of the CNTs[165] constraining one side of the plastic substrate, analogous to a simple bimetal actuator. The unique combination of characteristics that comprise this actuation system creates one of the most facile, yet versatile fabrication methods for creating PAO.

Compared to actuators using electroactive polymers (EAPs) that might give similar performance, considering the weight of the entire structure,[166] the PAO actuators have some distinct advantages: (i) The low sheet resistance of CNT films allows for the use of low voltages to drive the current needed for electrothermal actuation. This allowed the use

of batteries to power the robot. (ii) These actuators were made from common polymer films, rather than electroactive or ferroelectric polymers, highlighting their versatility. (iii) Due to the optical characteristics[167] and excellent electrical conductivity[168] of CNTs, these actuators can also be powered by light, heat, or microwaves. (iv) These actuators were easy to fabricate. In some cases, the conductive inks were painted on by hand. The simple device architecture provided design flexibility that allowed the construction of several different PAO devices.

Due to their simple structure and these distinct advantages, the actuators were also used for photo/thermal detection applications when their size was decreased to micro scale. Unlike the large size actuators, the micro-actuators can actuate and respond to heat and light much faster. Based on the simple parallel plate capacitor structure, the photo/thermal sensors were easily fabricated with these mico-actuators. And a minimum 20 μW laser radiation was detected using the photo/thermal sensors in the measurement.

As another kind of bimorph structure actuators, the electrochemical actuators based on electroactive materials were also demonstrated in this work. Unlike the thermal bimorph actuators driven by thermal energy, the electrochemical bimorph actuators made use of the volume change of the eletroactive material during the electrochemical reactions. Since there is no energy loss from the heat, the electrochemical actuators are very suitable for underwater applications. Using a sandwich structure, an electrochemical actuator was fabricated that can bend toward two directions by alternatively conducting the electrochemical reaction.

4.2 Experiment Details of Thermal Bimorph actuators

4.2.1 Printing Techniques and CNT Ink Preparation

Single-walled carbon nanotubes (Carbon Solutions, P3) were oxidized[169] in order to render them less hydrophobic and easier to disperse compared to un-functionalized CNTs or CNTs grown by chemical vapor deposition. Inks were made by mixing and then sonicating[170] a 0.1-5% weight ratio (typically 0.3%) of nanotubes in a 1:1 mixture of ethanol and water. A light centrifugation step using a micro-centrifuge at 13,000g for 30 seconds was performed in some cases to remove large bundles of nanotubes.[171] Patterning was achieved using stencils, silk screen printing and/or inkjet printing. Multiple coatings were used to lower the sheet resistance to the typical single digit Ω/□ range. The low sheet resistance allows for a smaller driving voltage to be used to achieve actuation. Other conductive coatings with single digit sheet resistances were tested as replacements for the single walled carbon nanotubes. Silver paint was too rigid after drying to bend when a voltage was applied. Sputtered gold did not adhere well enough to the substrate to constrain one side and induce curvature.

4.2.1.1 Stencil Mask

Most actuators were made with a stencil mask such as scotch tape cut with a razor blade or a laser-cut stencil secured to the plastic film with adhesive. The plastic substrate was cleaned with acetone or ethanol and dried with compressed air prior to ink deposition. The nanotube inks were deposited by pouring them onto the stencil-patterned plastic films for low viscosity inks or squeegeed in for the high viscosity inks. The ink was then allowed to self-level to the thickness of the tape and dried with a heat gun.

4.2.1.2 Ink-Jet

The carbon nanotubes were dispersed in ethanol, water and 1-cyclohexyl-2-pyrrolidone (CHP) at a 4:4:1 ratio respectively. The CHP helped with wetting characteristics and solution stability. The mixture was sonicated in room temperature followed by 5 minute 13,000g centrifuge step to remove large nanotube bundles. The supernatant solvents were evaporated in cases when the concentration of nanotubes was deemed to be too low. This process varied the actual ratio of solvents, so a variety of solvent ratios were actually used. Dimatix Materials Printer DMP-2800 is used for the ink-jet printing. The accompanying 11610 Dimatix Materials Cartridge has a nozzle size of 22 μm and provided 10 pL per droplet.

4.2.1.3 Screen Printing

A stencil was made by coating a polyester mesh with Chromaline Chromablue screen printing emulsion. The emulsion was air dried for about an hour. A positive image of the actuator circuit design was printed onto transparency film as the photo-mask. The screen was placed in an exposure unit and exposed to UV light for two minutes to cure the emulsion. The screen was rinsed with water to dissolve any unexposed emulsion. Carbon nanotube ink was deposited on the silk screen and pulled across the image with a plastic squeegee to deposit a thin layer of CNT ink onto the plastic film. The supplies were purchased from Advanced Screen Technologies.

Inks for screen printing were made using the inks for stencil and Inkjet patterning techniques. Phase separation was observed with an optical microscope using only a 50:50 water-ethanol solvent mixture. Screen clogging and de-wetting were problems with the

water-alcohol mixture. Stability and screen clogging problems were mitigated by centrifuging the inks, then evaporating the solvent to achieve higher concentrations.

4.2.2 Plastic Film Selection

Many common plastic films were tested in this work. The plastic films and their part numbers (P/N) are listed below: Polyimide (Kapton) - P/N 2271K73, polyoxymethylene (acetal) - P/Ns 5742T31, 5742T11 and 5742T51, polycarbonate (PC) - P/N 85585K102, polyester (PE) - P/N 8567K52, cellulose acetate - P/N 8564K44, Acrylonitrile butadiene styrene (ABS) - P/N 5751T31, polyvinyl chloride (PVC) - P/N 8562K11 and polyether ether ketone (PEEK) - P/N 4671T21, were purchased from McMaster Carr.

Plastic films were selected as substrates for the patterned nanotube coatings based on several criteria. Selected films had a Young's modulus large enough to retain their shape after being folded like paper origami, and could support their own weight when configured as a walking structure. Various plastic films (with thickness of 76.2, 127 and 254 μm) were selected and tested for actuation based on their high linear coefficients of expansion (α), glass transition temperatures (T_g), and melting points (Fig. 4.1A-B). All plastic films tested, including films not meeting the modulus criteria, produced force and movement. However, polyoxymethylene (acetal) and polyimide (Kapton) films had the best performance, based on properties depicted in Fig. 4.1 A-B. An example of an actuator made by this method is shown in Fig. 4.1 C-D.

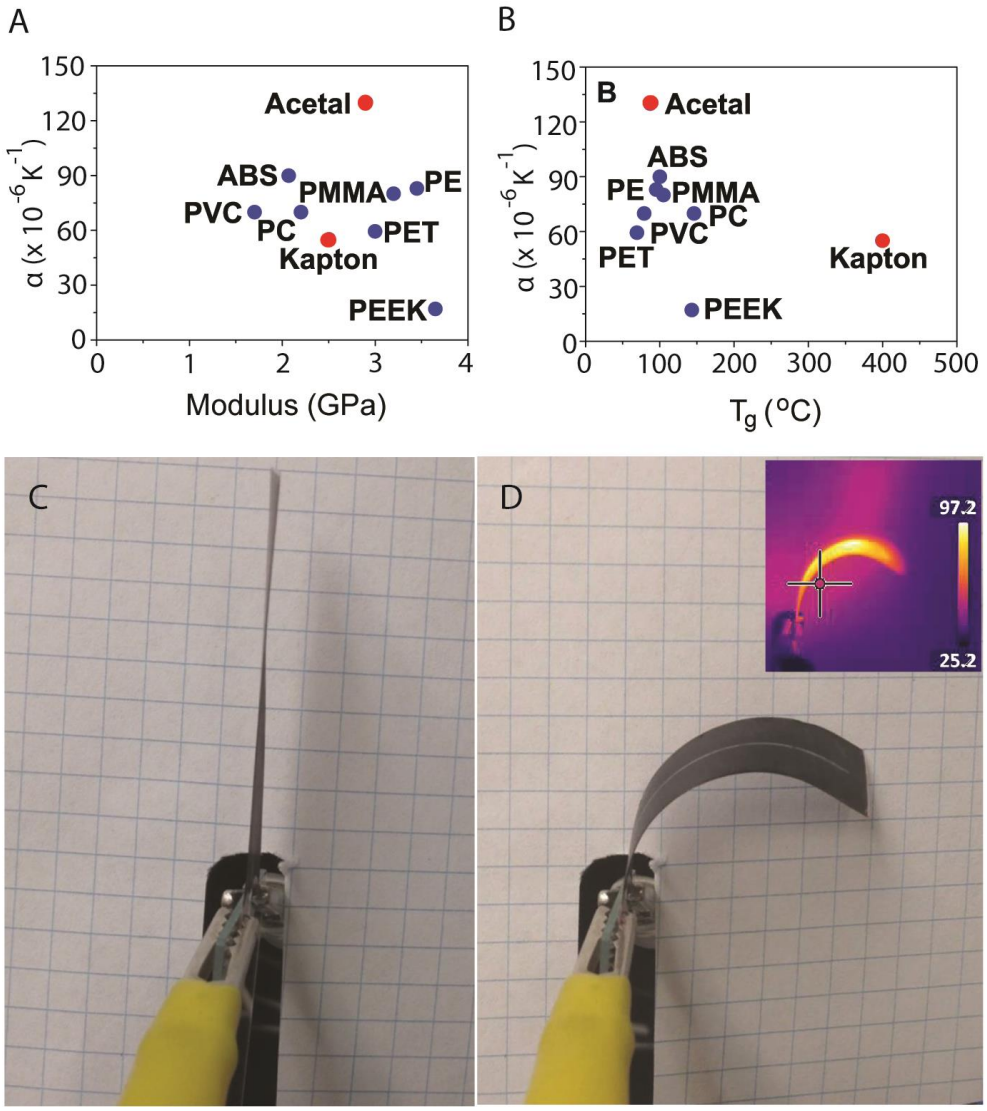

Figure 4.1 (A) The selection of polymer films was based on the expansion coefficient (α) being higher relative to other polymers and the modulus being high enough for the polymer to support its own weight, as a robot, but not so high as to limit movement. Acetal certainly sticks out with its high thermal expansion and midrange modulus. Kapton however does not appear to be different than the other polymer, aside from its midrange modulus. (B) The modulus changes with temperature, so a second polymer selection criterion was based on the plot of expansion coefficient versus the glass transition temperature. Kapton's high T_g

(temperature at which a polymer's modulus rapidly decreases) allowed greater total linear expansion than other polymers. (C) An actuator fabricated using an acetal film substrate, before power is applied to the actuator and (D) deflection after power is applied. (D-inset) Thermal image of the powered actuator showing uniform heating (false color scale depicts temperature in degrees Celsius).

4.3 Characterization of Thermal Bimorph Actuators

In order to power the actuator with electricity, the center of the CNT coating was removed to form a U-shape for CNT layer so that U-shape of CNT layer can act as a resistor and be heated by electricity uniformly. The actuators were characterized by measuring the force generated for a given power of electricity and the maximum force to failure. The force exerted by the actuator is an important characteristic for a walking robot, since it determines how much load it can carry in addition to its own weight. To understand the effect of actuator geometry on the magnitude of the force exerted, several actuators were fabricated with different widths, lengths and thicknesses. The force was determined by considering the actuator as a cantilever[172] and measuring the force exerted on a Mettler XP205 balance connected to a computer for data acquisition using Lab View. Actuation was controlled through Lab View via a data acquisition card (NI USB-6009 DAQ) connected to a relay breakout board and DC power supply. The DAQ also recorded the signal from a voltage divider circuit, which monitored the resistance of the actuators with time.

4.3.1 Temperature and Power Relation of Active Beam Calculation

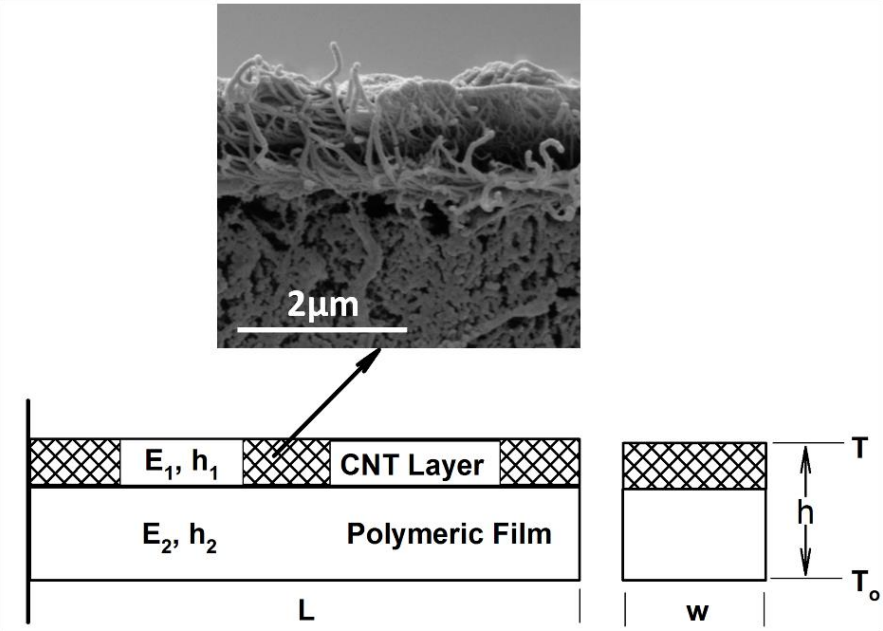

Figure 4.2 Schematic of a cantilever composite beam comprised of a CNT layer on a plastic film with length L, width w, and thickness h.

Heat-transfer analysis was used to predict the temperature of the actuator as a function of power input. The printed active origami is modeled as a rectangular cantilever beam comprised of a plastic strip coated with a CNT layer as shown schematically in Fig. 4.2. The composite beam is activated by supplying power, *P*, to the CNT layer, which causes internal heating and a temperature rise in the CNT. The temperature in the CNT layer is *T*, while the temperature of the plastic substrate before activation is T_o and the temperature gradient across the composite beam is, $\Delta T = T\text{-}T_o$, is given by

$$\Delta T = \frac{h}{h'}\frac{1}{A}\frac{\Delta Q}{\Delta t} = \frac{h}{h'}\frac{1}{A}P \qquad (4.\ 1)$$

where *h* is the thickness, *h'* is heat conductivity A is the area normal to the heat flow, $\Delta Q/\Delta t$ is the heat flux or power, P.

The heat flow through the CNT layer is controlled by single and multiple junctions in the 3-D CNT network, which has been analyzed by Chalopin *et al.*[173] and Prasher *et al.*[174] From the paper by Chalopin,[173] the thermal conductivity of a CNT network is given by:

$$h' = \frac{0.18l}{2\pi d}\left(\frac{\rho_1}{\rho_g}\right)\sigma \tag{4. 2}$$

where l is the length and d is the diameter of CNT, ρ_1 is the density of the CNT layer, σ is the thermal conductance of a CNT junction, and ρ_g is the density of graphene. Substituting Eq. 4.2 into Eq. 4.1 gives

$$\Delta T = \frac{2\pi h d\rho_g}{0.18l\rho_1 A\sigma}P \tag{4.3}$$

The density of the CNT layer, which can be written in terms of the mass, m_{CNTL}, and the thickness, h_1, of the CNT layer, is given by

$$\rho_1 = \frac{m_{CNTL}}{h_1 A} \tag{4.4}$$

which can be combined with Eq. 4.3 to give:

$$\Delta T = \frac{2\pi h d\rho_g}{0.18l\sigma(m_{CNTL}/h_1)}P \tag{4.5}$$

Eq. 4.5 indicates that the temperature change on the CNT layer is independent of the width of the composite beam specimen as observed in the experiment (Fig. 4.3A).

The thermal conductance of the CNT layer can be obtained by considering that the 3-D CNT network is comprised of a series of single and double junction.[174] Heat flow through single junctions is not influenced by other CNTs because the CNTs are widely spaced (> 1 μm). In contrast, heat flow through multiple (double) junctions is influenced by other

CNTs when the junction spacing is less than the coherence length, which is about 1 μm at 50Hz.[174] The CNT network utilized in this study, shown in Fig. 4.2, is typically comprised of a combination of single junctions and multiple junctions. Thus, the conductance, σ, of the 3-D CNT network can be estimated as

$$\sigma = V_{sj}\sigma_{sj} + V_{mj}\sigma_{mj} \tag{4.6}$$

where V is the volume fraction; the subscripts sj and mj denote single junction and double junction, respectively. Eqs. 4.5 and 4.6 were combined and utilized to compute the temperature of the active beam as a function of power input. All of the material parameters, which are tabulated in Table 4.1, are either measured experimentally or taken from the literature. The theoretical values reported by Prasher, *et al.*[174] for the conductance of single and multiple junctions of a 3-D CNT network were used. The only unknown parameters are the volume fractions of the single and multiple junctions in the 3-D CNT network. Fitting the model to the experimental data shown in Fig. 4.3A provided volume fractions of 14% and 86% for the single junction and multiple junctions, respectively. These values are consistent with the micrograph shown in Fig. 4.2, which reveals that most the CNT junctions are less than 1 μm while a few are larger than 1 μm apart. The finding suggests that heat transfer in the 3-D CNT network is dominated by multiple junctions.

Table 4.1 Material parameters for the temperature-power computation

Parameter	Value, unit	Source
d	12 nm	Rinzler *et al.*[169]
h	127 μm	Measured
ρ_g	7.6 E-7 kg.m^2	Prasher *et al.*[174]
m_{CNTL}/h_1	3.39 E-2 kg/m	Computed from CNT layer density and area; this study
h_1	1.36 μm	Measured
l	1 μm	Prasher *et al.*[174]
σ_{sj}	50 E-12 W/K	Prasher *et al.*[174]
σ_{mj}	3.5 E-12 W/K	Prasher *et al.*[174]

Using Eq. 4.5, ΔT can be computed once the power input, P, is specified. The experimentally obtained CNT layer temperature (T) was determined by using a thermal camera (FLIR-T400) (Fig. 4.1D, inset) for each applied P and was in close agreement with the theoretical predictions for 3 different actuator widths (Fig. 4.3A). Moreover, both experimentally derived values for temperature and the calculations indicate that the temperature on the CNT layer is independent of the width of the composite beam.

The dependence of the force on the dimensions of the actuator is shown in Figs. 4.3B-D. The standard actuator had dimensions of 3 cm x 1 cm x 0.0127 cm and each dimension was correspondingly evaluated. For each dimensional test, only one corresponding dimension was changed. Various widths (0.5, 1, and 1.5 cm) with the same length (3 cm) and thickness (0.0127 cm) are compared in Fig. 4.3B. A comparison of lengths (2, 3, and 5 cm), using a constant width (1 cm) and thickness (0.0127 cm) is presented in Fig. 4.3C. The effect of changing the thickness (0.0127 and 0.0254 cm) of the samples is shown in Fig. 4.3D. In each case, testing was conducted by powering the actuator for 30 seconds in 1V

increments in order to reach the steady state temperature (T_{max}). Between each power cycle, the actuator was allowed to cool for 30 seconds to ensure a full return to room temperature.

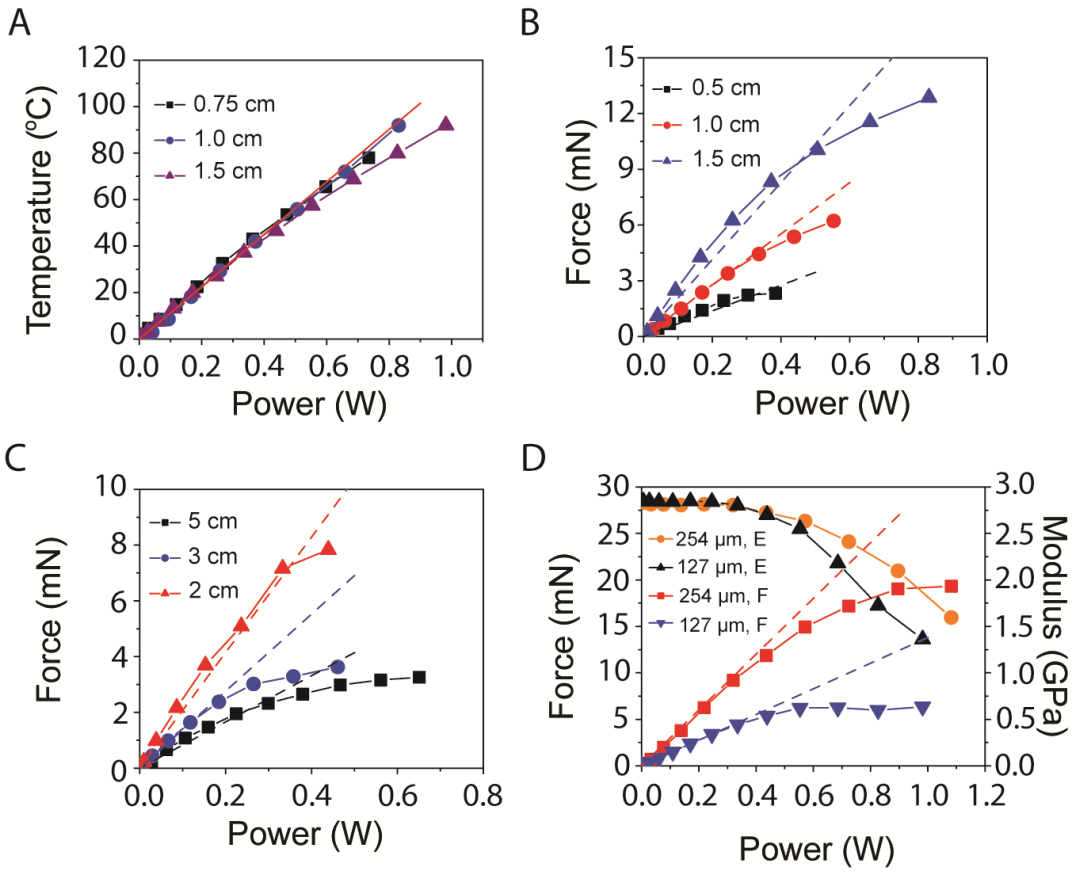

Figure 4.3 Comparison of experimental (solid) and calculated (dashed) results (A) The temperature generated for actuators with different widths as a function of applied power. (B) The exerted force for different actuator widths as a function of applied power. (C) The exerted force for different actuator lengths as a function of applied power. (D) The exerted force for different actuator thicknesses as a function of applied power (blue and red traces) the modulus change for two samples with different thickness as a function of applied power (black and orange traces).

4.3.2 Force of an Active Beam

The Timoshenko beam theory[82] was used to determine the force, F, and curvature, ρ, for CNT-coated plastic films. According to this beam theory:

$$F = \frac{3EI}{2\rho L} \tag{4.7}$$

$$\frac{1}{\rho} = \frac{6\Delta\alpha\Delta T(1+m)^2}{h(3(1+m)^2 + (1+mn)(m^2 + \frac{1}{mn}))} \tag{4.8}$$

where I donates the area moment of inertia (for a rectangle cross section area $I = (wh^3)/12$), ρ the curvature of the actuator, E the modulus of the actuator, w is the width of the actuator, h is the thickness of the actuator, L is the length of the actuator, m the ratio between the thickness of the CNT film and the plastic, n is the ratio of the modulus of the CNT films and the plastic, $\Delta\alpha$ is difference between the linear thermal expansion coefficients of the CNT film and the plastic, and ΔT is temperature gradient across the thickness of the composite beam. Combining eq. 4.7 and 4.8 leads to

$$F = \frac{kEwh^2\Delta\alpha\Delta T}{8L} \tag{4.9}$$

$$k = \frac{(1+m)^2}{3(1+m)^2 + (1+mn)(m^2 + \frac{1}{mn})} \tag{4.10}$$

and the ΔT term can be obtained from Eq. 4.3. Substituting ΔT into Eq. 4.9 gives

$$F = \frac{kEwh^3\Delta\alpha}{8L}\left[\frac{2\pi d\rho_g P}{0.18l\sigma(m_{CNTL}/h_1)}\right] \tag{4.11}$$

which can be used to design and control the deflection of composite beam through the power input, P. For illustration, Eq. 4.11 was utilized to compute the force response of the

composite beam of a CNT layer on an acetal film for various thicknesses, widths, and lengths of the composite beam. The material properties for these computations were obtained from experimental data.

The Young's modulus of CNT films has been reported to vary from 10-100 GPa.[173] This wide range of values was narrowed by experimentally determining the Young's modulus for 10 sample actuators made in the lab. The actuators were set up as cantilevers. One end of the plastic strip was clamped and small weights were placed on the other end. The deflection was measured with a ruler and recoded along with the value of the weight placed on the end. A graph was made from the plotted data and the slope was determined. The slope of the line was used to calculate the Young's modulus using the equation: $E = \frac{1}{3}\frac{gL^3}{sI}$, where I is area moment of inertia; g = 9.81 m/s; s is the slope of stress – strain plot. The modulus (E) was around 2.6 GPa, matching the literature values for acetal films and similar for nanotube coated plastic films and bare films. The nanotube coating introduced a change of 10% or less and was not measureable within the experimental error. The nanotube coating thickness was measured by scanning electron microscopy.

The modulus of the acetal and carbon nanotube films are: $E_{acetal} \approx 2.6GP$, $E_{carbon} = 10\text{-}15E_{acetal,}$ assuming $E_{carbon} = 12E_{acetal}$ then n = 12. SEM images were used to determine the nanotube coating thickness (Fig. 4.2). The carbon nanotube film is about 1/100 of the thickness of the plastic, so m=0.01 therefore k = 0.494, from Eq. 4.10. The expansion coefficient of acetal α_{acetal} is about 110-150 x 10^{-6} / K, taking $\alpha_{acetal} = 137 \times 10^{-6}$ / K, in order to fit well with the experimental data. The expansion coefficient of nanotube film is very small[175,176] compared to that of acetal, $\alpha_{nanotubes} << \alpha_{acetal}$, so, $\Delta\alpha \approx \alpha_{acetal}$. A sample with the

dimensions L = 3 cm, $w = 1.0\ cm$, h=0.127 mm, putting all these values into Eq. 4.11, the force equation becomes F = 1.392P. The force generated by samples with different dimensions was calculated using the same Eq. 4.11 and the results are shown in Figs. 4.3B-D.The force response for various thickness values is presented in Fig. 4.3D. The force response for various widths and various lengths are presented in Figs. 4.3B and 4.3C, respectively. In all cases, the computed forces are in good agreement with the measured values. Thus, Eq. 4.11 can be used for designing and manipulating the motion of printed active origami made from CNT-coated plastic films simply by controlling the power input.

The force generated by samples with different dimensions was calculated using Eq. 4.11 and the results are shown in Figs. 4.3B-D. In all cases, the computed forces are in good agreement with the measured values at low powers (i.e. low temperatures). Thus, Eq. 4.11 can be used for designing and manipulating the motion of printed active origami made from CNT-coated plastic films simply by controlling the power input. However, for increasing power (temperature), the measured force started to deviate from the theoretical value. This was a result of the temperature being too close to the T_g of the polymer substrate, which induced polymer chain relaxation and structural changes.[177] This non-linear behavior observed at high powers indicates that the modulus is decreasing with temperature as indicated in Fig. 4.3D.

The experimental data and calculations in Fig. 4.3 show that the maximum force for a given actuator is achieved for a thick and short design. Conversely, the calculation also revealed that longer and thinner designs provide greater deflection. Actuators demonstrated curvature on both axes of the plastic film plane, but commonly favored curvature primarily perpendicular to the longest dimension. A 2 cm × 2cm × 0.0254 cm

actuator was fabricated that developed more than 9 g force (0.088 N), as measured on the balance pan, which was 60 times its own weight. The force to weight ratio using actuators with electroactive polymers (EAPs) is often calculated using the force produced over the weight of the conductive coating, while ignoring the weight of the plastic substrate and liquid used for the electrolyte.[178] In this case, the entire device weight for the actuator is considered.

4.3.3 Force Measurement and Durability Cycling Data

To determine the durability of these actuators, actuators made from acetal and Kapton were tested for maximum cycling rate (Fig. 4.4). The voltage was adjusted (15-30 V) to heat the samples quickly, with on/off times of tens of milliseconds. The actuators typically reached 20-30 Hz. High actuation rates were possible with thinner films (127 μm or less). The cycling rate was intrinsically limited by the thermal conductivity of the polymer and the film thickness. Nanotube-coated Kapton films were compared to bare films after reaching 300 ^{o}C in an oven for several minutes with a thermal camera. The nanotube coated sample cooled faster, although the exact rate was not determined. The increase is expected given the higher surface area that the nanotube coating provides, so the coating modified the thermal transfer rate and contributed to higher frequency actuation.

The actuator was setup in a cantilever configuration for the force measurement[172] that used a Mettler 205 balance as the force sensor that was connected to a computer serial port and controlled by Lab View software for Mettler balances available on-line. Data acquisition and control of the actuator timing was achieved using Lab-View software with a National Instruments data acquisition card (NI USB-6009 DAQ) connected to a computer via USB. The output signal from the DAQ was sent to a break-out board with

relays that switched on to connect the power supply directly to the actuator. The actuators resistance was measured by a voltage divider circuit connected to the DAQ and recorded as voltage (V_{out}), as shown in Fig. 4.6B. The actuator's resistance was calculated using the equation $R_1 = \frac{R_2 \times V_{in}}{V_{out}} - R_2$ and the power was calculated using $P = \frac{(V_{in} - V_{out})V_{out}}{22}$. In the circuit, R_2 is a resistor with resistance of 22 Ω, and V_{in} is the voltage from the power supply. In order to measure the resistance of device, LabVIEW was used to measure the voltage of the divider resistance V_{out}.

The durability of an example actuator (acetal substrate 3cm x 1.5cm x 0.0127cm) was tested for 50,000 full cycles. Data was recorded for the force and resistance changes with the cycles. The working voltage was 10V, the current was 0.07A and the on/off time to 5s/7s respectively, which were based on the requirement of the walking robot. The recorded force changed less than 10% after the ~50k cycles, shown in Fig. 4.4. The durability of the fast cycling actuators was also tested. An example Kapton actuator cycled 1,000,000 times at 30 Hz without any observable changes. A fast actuating (20 Hz) dragon fly was designed and fabricated as shown in Fig. 4.5E.

The small resistance change that occurred might be due to changes in humidity, structural changes (movement) or loss of metallic nanotubes. The metallic nanotubes are known to carry the majority of the current in nanotube networks. The metallic nanotubes were shown to burn in air when high current was passed through them.[79]

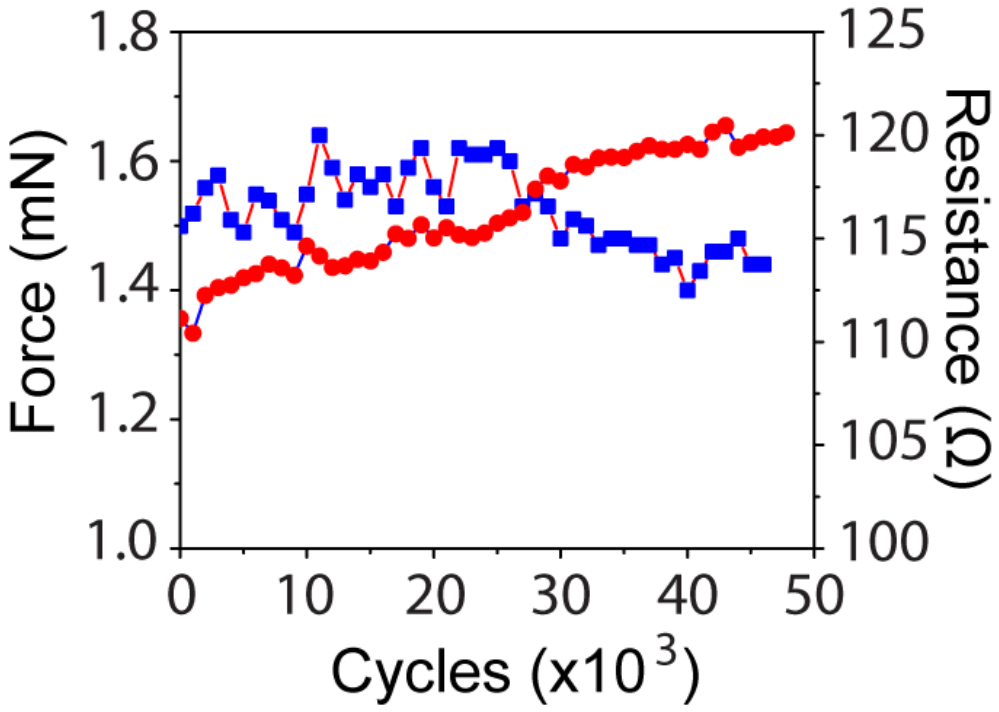

Figure 4.4 The durability test of the actuator. The measured force (blue) and resistance (red) of an actuator as a function of cycles. The change was less than 10% over the duration of the test.

To confirm the electrothermally driven actuation mechanism, the CNT/polymer bilayer films were placed in an isothermal environment with uncoated polymer films serving as controls. The CNT/polymer film curved towards the CNT coating, indicating that the CNT layer was under compression and confirming that it is a thermal bimorph actuator. However, heating the CNT film using electrical current made the film bend the opposite way for a very short period of time (visually observed). There are two possible causes for this: 1) the nanotubes heat rapidly due to their high thermal conductivity[179] and expand before the polymer is heated. Therefore, the films bend away from the CNT layer initially. 2) The voltage was set higher (12-15V) than the minimum values (1-3V) needed to drive

actuation to increase heating rates. The polymer expands closest to the nanotube coating, while the heat is still traveling through the polymer film causing the actuator to bend towards the cooler side. The actuator quickly bends the opposite direction once the heat reaches the entire volume of the plastic film. Thus, the actual actuation mechanism may be more complicated than for a bimetallic system. Based on the calculated and experimental results, three design constraints were considered for fabrication of an active origami robot: (i) deflection distance, (ii) exerted force, and (iii) operating temperature.

4.4 The Applications as Printed Active Origami

An actuator was fabricated that developed the force needed to carry the weight of the circuits and the structure itself, (e.g. about 0.5grams for small robot in Fig. 4.5A-D) The actuator also needed to move 1 cm per step, so that 50k cycles would equal 0.5 kilometers. These requirements were based on the minimum criteria a robot needed to achieve for the Google Lunar X-Prize (www.googlelunarxprize.org). A walking robot was made as shown in Fig. 4.5D. The dimensions chosen for the actuators (legs) were 2 cm x 0.6 cm x 0.0076 cm. The robot body was fabricated using a laser cut Kapton stencil coated with adhesive Fig. 4.5A. Silver ink was used as the electrical connection pathways on the main body of the robot Fig. 4.5B. The robot's circuit in Fig. 4.5C was made by inkjet printing silver to form the circuit traces on polyethylene naphthalate and then attaching the circuit to the main body of the robot with tape or glue. This modular method of fabrication was favored over printing the entire device as one unit, as different circuits could be designed and interchanged for the same robot body. The legs were controlled initially with Lab View through the 6009 DAQ and relay breakout board. The robot was powered by a single 12 V A23 battery, but could also be powered by 2-3 AAA and AA batteries (3-4.5V) and was

able to walk 1 cm per step. A simple program of on/off time was tested to determine the best parameters for a very basic onboard control system. In order to make the robot autonomous, a circuit was designed to actuate its legs diagonally in pairs using two 555 timer circuits. The robot's circuit in Fig. 4.6A was made by inkjet printing silver to form the circuit traces on polyethylene naphthalate and then attaching this circuit to the main body of the robot with tape or glue. This modular method of fabrication was favored over printing the entire device as one unit, as mistakes were easier and less time consuming to correct. Two 555 timer chips were programmed with selected resistors (R_1= 1.2 kΩ and R_2 = 7.48 MΩ) and capacitors (C_1 = 1 μF) to have an on time of 5.2 seconds and an off time of 5.2 seconds. On time was calculated as (T_{on}) = 0.693 * (R1+R2) * C and the time off = 0.693 * R2 * C. Larger robots that required higher current than the robot in Fig. 4.5D were controlled by the timer chip's output signal modulating a transistor. The transistor source was connected directly to the battery and the drain was connected to the robot legs. The robot body was fabricated using a laser cut Kapton stencil coated with adhesive. Silver ink was used as the electrical connection pathways on the main body of the robot. Crossed connections were made using tape as the insulator. Carbon nanotubes were used to coat the legs in order to make an actuator. Many designs were tested, including 2, 4 and 6 actuating legs designs. The legs were bent in order to make the walking movement more effective.

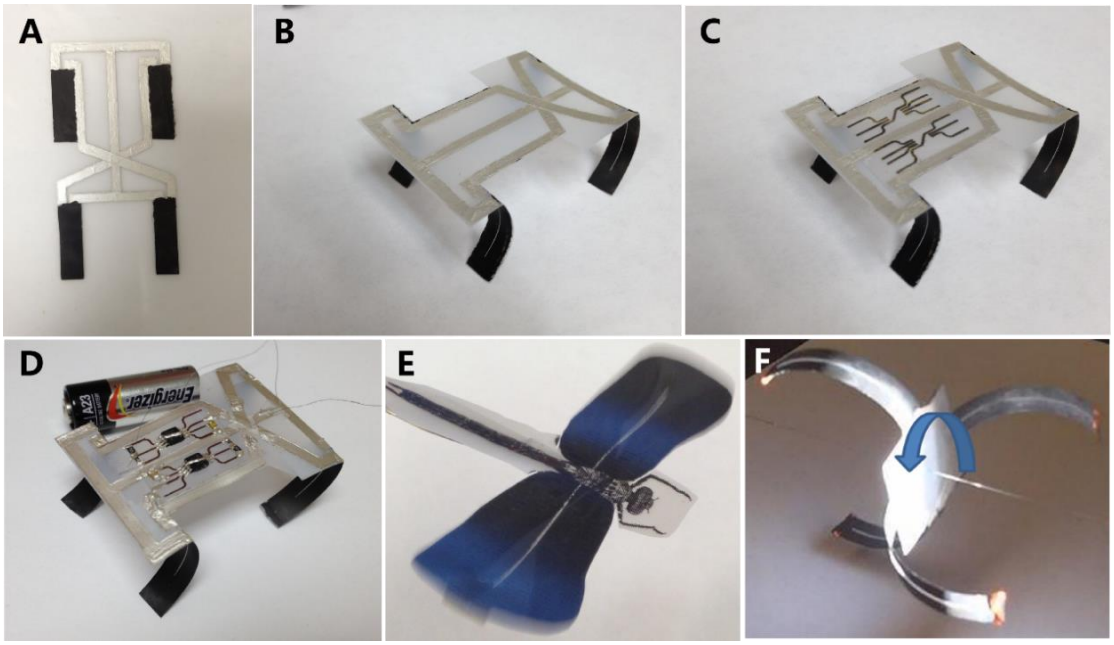

Figure 4.5 (A-C) Fabrication process for PAO (D) A printed robot on acetal film with a dual timer chip control circuit powered by an A23 battery. (E) A dragonfly with acetal wings that beat at 20 Hz. (F) A rotating acetal actuator powered by light.

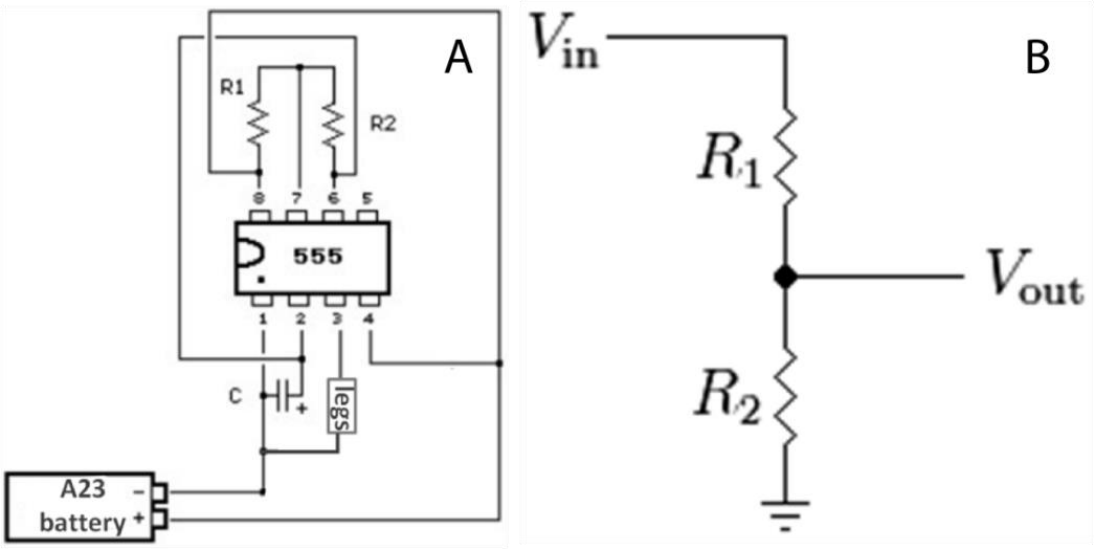

Figure 4.6 (A) Schematic for the 555 timer chip control circuit for the robot. (B) Voltage divider circuit schematic to measure the resistance of the actuator.

Due to their optical absorbance characteristics, the CNTs can also absorb light and convert it to heat[180] and serve as multifunctional energy transducers. This was demonstrated by fabrication of a light-driven rotating actuator as shown in Fig. 4.5F. The shape is a pair of vertex-intersecting parabolas extending away from each other. Each parabola is made of two legs, with very small copper wire weights on the ends of the legs. These small weights offer more driving force when they extend past the center of gravity and introduce a rotational motion by moving the moment out away from the wire to create torque. Each leg was coated with CNTs, which absorbed light and heated the polymer substrate while under irradiation with a 300 W Xenon lamp. The increased temperatures cause the actuator to bend outwards. Upon cooling in the dark, the copper weight was pulled towards the center, thereby letting each leg return to its original position. The axis of rotation was fixed by a copper wire threaded through the center of the disc and the rotation speed was about 5s per cycle.

4.5 Applications as Photo/Thermal Detectors

Since the actuators can respond to both light and heat, they were also studied for the applications of photo/thermal detectors based on the similar actuator structure. Unlike the requirement in the walking robot application, the force generated by the actuators is not as important. However, the deflection or the curvature of the actuators responding to the light or heat is more important so that they can be sensitive enough to serve as detectors.

According to the equations mentioned before, the curvature of a suspended beam could be expressed as Eq. 4.8. For any specific case, when the materials have been determined, the expansion difference $\Delta\alpha$ would be fixed. The thickness h and operation temperature ΔT can also be fixed for each application. Then the curvature will mainly depend on m, the

ratio between the thickness of the CNT film and the plastic, and *n*, the ratio of the modulus of the CNT films and the plastic, which could be denoted as *k* (Eq. 4.10).

$$\frac{1}{\rho} = \frac{6\Delta\alpha\Delta T(1+m)^2}{h(3(1+m)^2 + (1+mn)(m^2 + \frac{1}{mn}))} \tag{4.8}$$

$$k = \frac{(1+m)^2}{3(1+m)^2 + (1+mn)(m^2 + \frac{1}{mn})} \tag{4.10}$$

For a general case, where the ratio of the thickness between the bilayer and the modulus are not determined, the dependence of factor *k* on *m* and *n* was calculated and shown in Fig. 4.7. For any specific case, when the materials of the bilayer were determined, the ratio of the modulus, *n* will be known, then for the maximum curvature the best ratio of the thickness between the bilayer could be chosen according to Fig. 4.7.

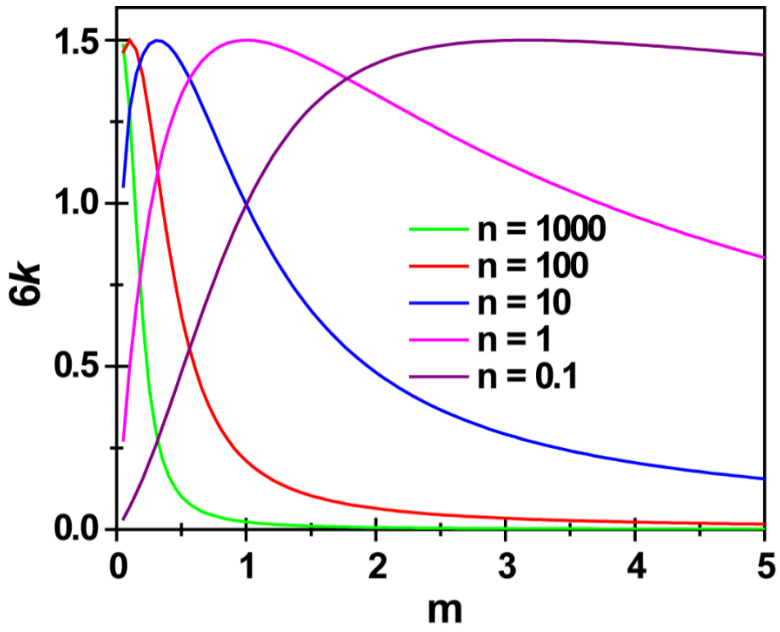

Figure 4.7 The dependence of factor *k* on the ratio of thickness, m, and the ratio of modulus, n.

As the demonstration of the concept, we fabricated a micro-actuator and tested its response to a laser beam (Fig. 4.8). The micro-actuator was fabricated with a layer-by-layer coating technique. First, a thin ZnO layer was coated onto the substrate using ZnO sol-gel for the following release step. Then a thin PVDF polymer layer was coated on the top of ZnO layer using 5% PVDF solution in NMP. Finally, the CNT ink was coated onto the PVDF to form the bilayer actuator structure. After the final layers were cut into the desired shape of the actuator, an HCl solution was used to etch the ZnO layer to release the actuator. In order to study how fast the actuator responded to the light, a ~10 mW 405 nm laser point was swept across the micro-actuator. After analyzing the recorded video, the actuator was found to bend almost 90^{o} in around 0.1 s, just as Fig. 4.8 shows. It means that at smaller sizes the thermal bimorph actuator could respond to light or heat very fast, which is very good and attractive for the photo/thermal sensor application.

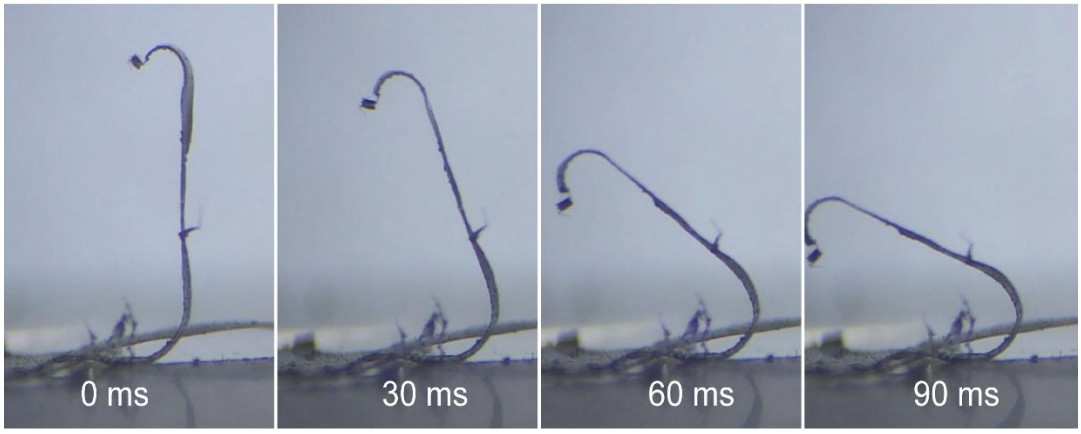

Figure 4.8 Photos of a micro-actuator (size: ~ 1 mm ×200 μm) responding to a 10 mW 405 nm laser beam. Taken under a microscope.

Based on the similar structure of this micro-actuator, a photo/thermal sensor was further fabricated and tested for the demonstration of the concept. As Fig. 4.9a,b shows, the sensor

worked based on the capacitor effect. Specifically, the CNT conductive layer worked as an electrode, while the bottom FTO strip layer worked as the other electrode. The polymer layer and the air gap acted as the dielectric. When the actuator was heated by light or heat, its deflection would cause the distance to change between the CNT and FTO electrodes, which would further change the capacitance between them. Fig. 4.9 c and d shows the distance change before and after a laser beam shined onto the actuator. The capacitance change was recorded with a capacitance meter, as Fig. 4.9e shows, where the capacitance responded to the laser very quickly. Theoretically, by calibrating the capacitance change to the corresponding power or temperature, the sensors could be used for photo or thermal detection. And due to the wide adsorption bands of CNTs, the sensor could be potentially used for UV-vis to IR detection. As a preliminary result, a minimum power as low as 20 μW 405 nm laser beam was detected in the lab. However, for real application, more work is still needed in future for the improvement of both fabrication process and detailed characterization.

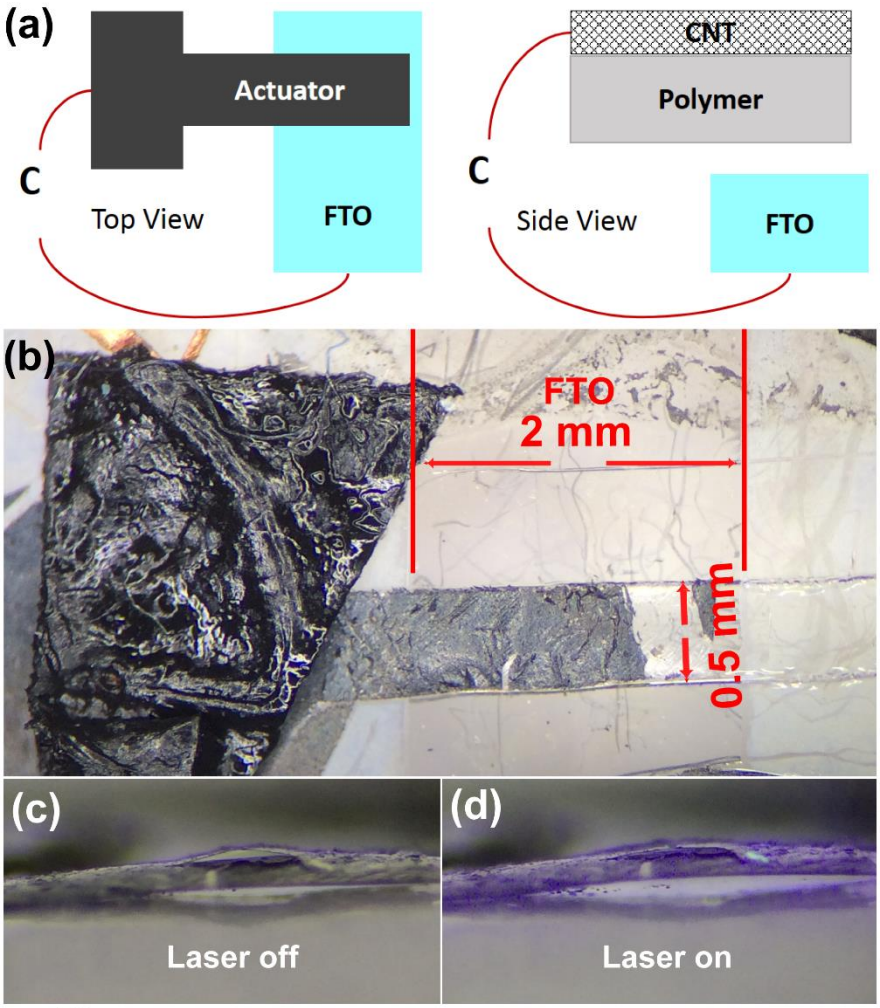
(a)
Actuator
C
Top View
FTO
CNT
Polymer
C
Side View
FTO
(b)
FTO
2 mm
0.5 mm
(c)
Laser off
(d)
Laser on

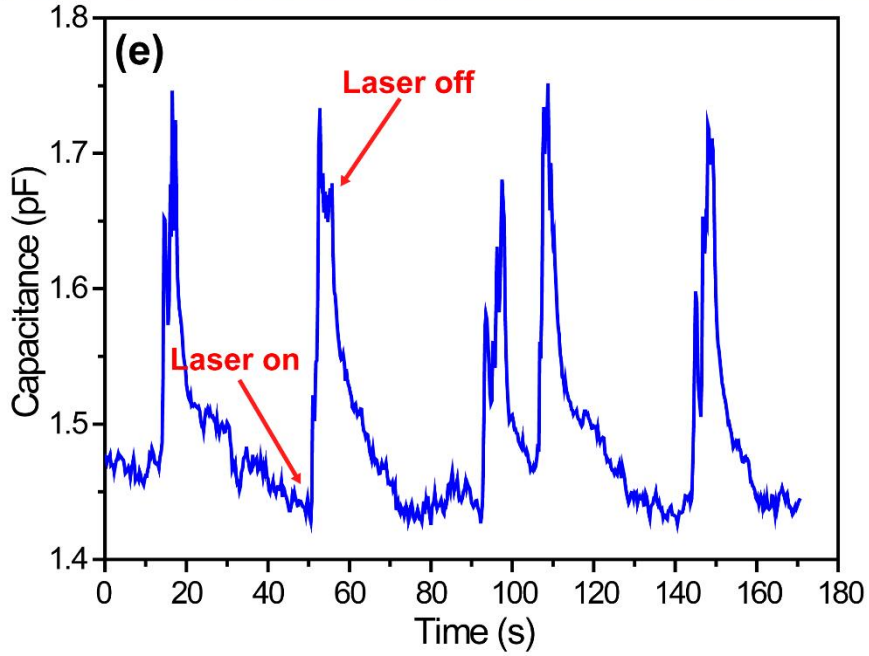
(e)
Laser off
Laser on
Capacitance (pF)
Time (s)
1.8
1.7
1.6
1.5
1.4
0
20
40
60
80
100
120
140
160
180

Figure 4.9 Schematic, photos and characterization of a photo/thermal sensor. (a) Top and side views of a schematic photo/thermal sensor based on parallel plate capacitor; (b) Top view of the photo/thermal sensor based on the CNTs/PVDF micro-actuator and FTO conductive strip; (c) and (d) side views of the same sensor when a laser beam was shined on and off; (e) the corresponding capacitance change between CNTs and FTO conductive layers.

4. 6 Electrochemical Actuators

Although the thermal bimorph actuators have very simple structures and can be easily fabricated, some drawbacks, such as their high energy consumption and inability to be used for underwater operation, limit their applications. For these reasons, electrochemical actuators are still needed, especially for applications in water. Among the strategies for the electrochemical actuators, ionic polymers have been studied the most.[76,181–183] Here, instead of using ionic polymers, an electrochemical actuator based on a MnO_2/Au nanostructure composite was developed. Due to its low cost and good performance, MnO_2 has been widely studied for energy storage applications, such as supercapacitors.[184–186] Just like many other energy storage materials, the volume of MnO_2 will change during the intercalation process of small ions, such as Li^+, or H^+. This effect was used for the actuation in the MnO_2/Au electrochemical actuator.

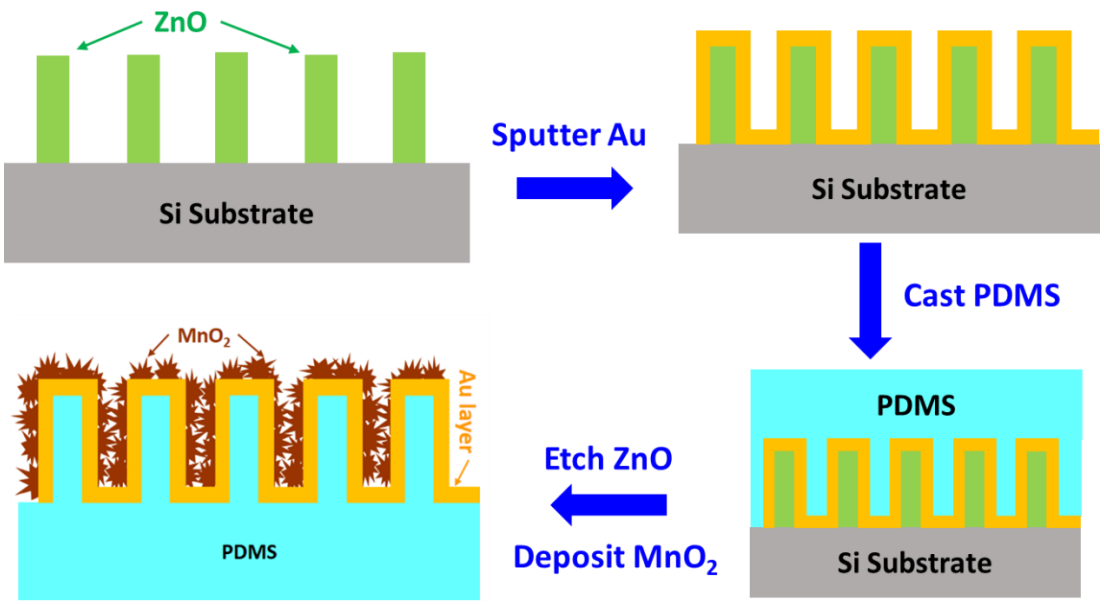

Figure 4.10 Schematic for the fabrication of MnO_2/Au/PDMS electrochemical actuator.

Figure 4.10 shows the process for the fabrication of the electrochemical actuator. In order to have a flexible porous electrode for the deposition of MnO_2, ZnO nanowires were used as the template for the fabrication of porous gold electrodes. Firstly, ZnO nanowires were grown on Si or glass surface with a liquid-phase chemical method described in the literatures before.[187,188] The as-made ZnO nanowires are shown in Fig. 4. 11 a, which are uniform and almost vertically aligned nanowires arrays. Secondly, 20-30 nm gold was coated onto these ZnO nanowires with sputtering for 5-10 minutes. The SEM image in Fig. 4. 11b shows that almost all ZnO nanowires were covered entirely by the rough Au layer. After etching the ZnO nanowires templates with HCl acid, the tube-like porous Au interconnected network was obtained, which looks like a nanoscale Au carpet (Fig. 4.11 c). This porous Au interconnected network was then used for the electrochemical deposition of MnO_2 in 100 mM Na_2SO_4 and 10 mM $MnSO_4$ solution with a current density of 100 $\mu A/cm^2$ for around 1h (Fig. 4.11 d). The electrodeposition was conducted using a

three-electrode configuration, where the Au electrode was used as working electrode, Ag/AgCl as reference electrode, and a Pt wire as counter electrode.[189]

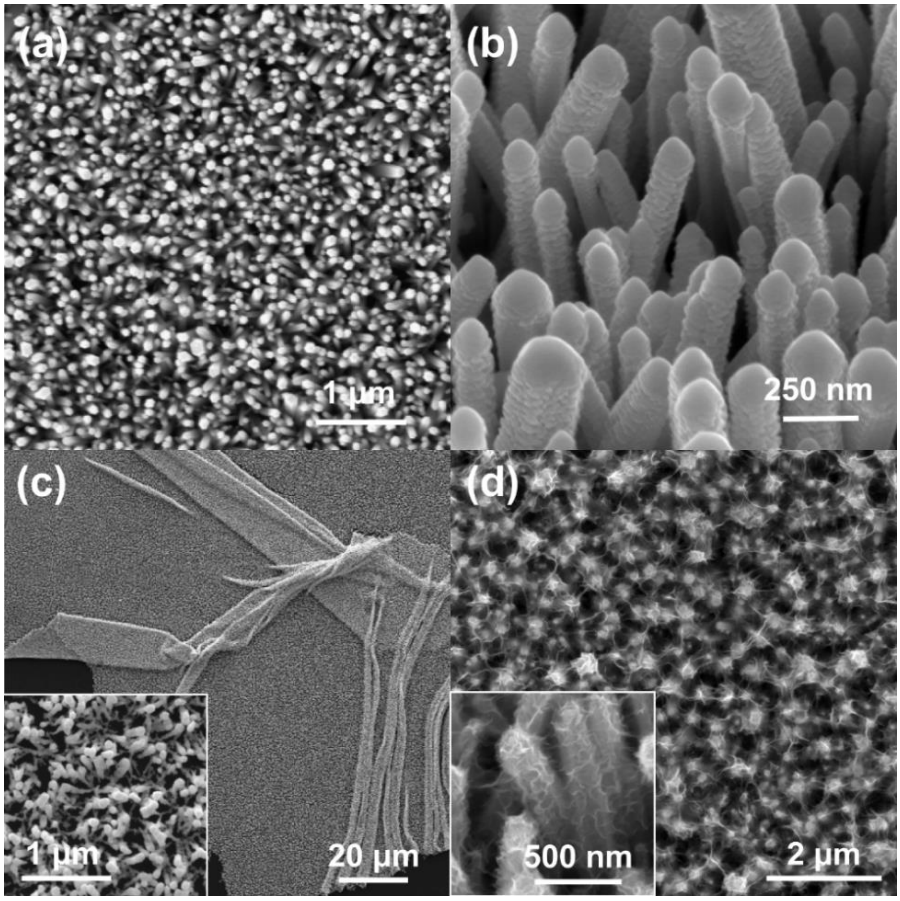

Figure 4.11 SEM images. (a) ZnO nanowires; (b) Au coated ZnO nanowires; (c) Porous Au tubes network; (d) MnO_2 deposited on the porous Au tubes network.

For the electrochemical actuator application, the MnO_2/Au did not have strong enough mechanical properties. To solve this problem, a polydimethylsiloxane (PDMS) polymer layer was used to strengthen the MnO_2/Au layer and acted as the low-expansion layer of the bimorph structure. In the fabrication process, PDMS was first poured onto the Au coated ZnO substrate, following with heating at 120 ^oC to form several tens of micrometers thick PDMS film. Then a Au/PDMS composite electrode film was obtained by etching the

ZnO nanowires template with HCl acid. Finally, the MnO_2/Au/PDMS electrochemical actuator was fabricated by further depositing MnO_2 onto the Au/PDMS electrode. A MnO_2/Au/PDMS electrochemical actuator that could bend and roll is shown in Fig. 4.12a, which was operated in 0.1 M Na_2SO_4 solution with a three-electrode set up, where the actuator was working electrode, Ag/AgCl as reference electrode, and a Pt wire as counter electrode. When the potential was scanned back and forth over the range of -0.2 V to 1.0 V, the following reaction: $MnO_2 + Na^+ + e^- \longleftrightarrow MnOONa$ will caused the volume change of the MnO_2/Au composite electrode while the volume of PDMS layer remained stable. As a result, the actuation of the bimorph was triggered.

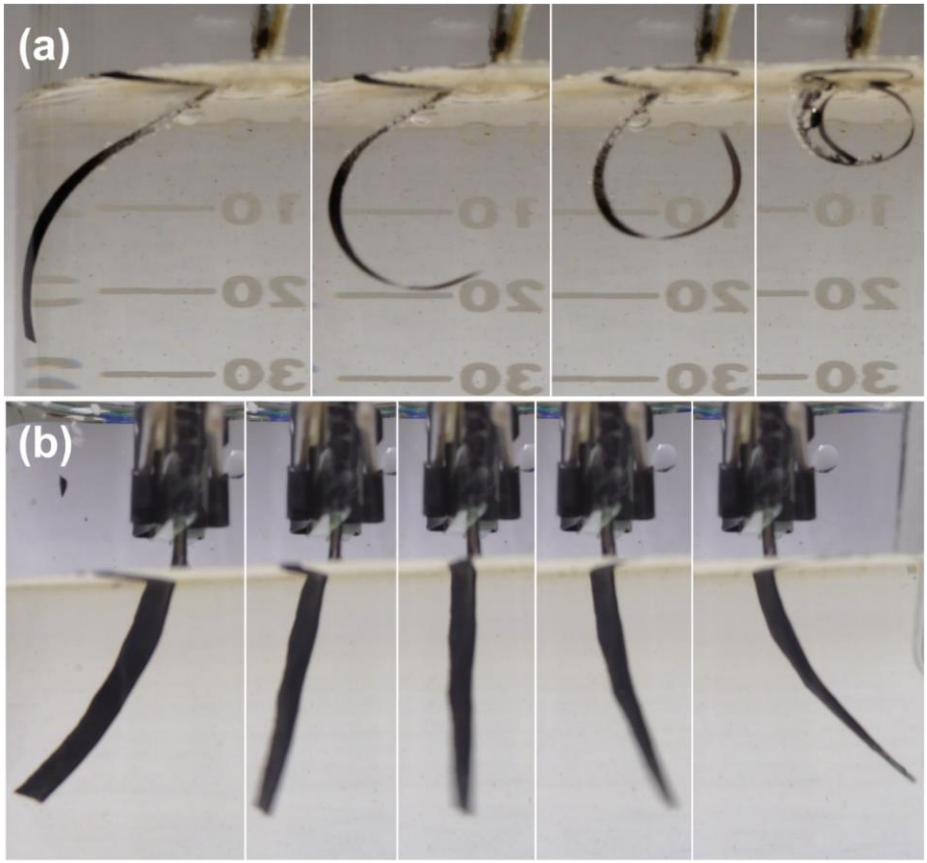

Figure 4.12 MnO_2/Au/PDMS actuators. (a) An electrochemical actuator made with MnO_2/Au composite electrode on only one side of PDMS strip (~ 0.5 × 3 cm^2) can bend

and roll into circle shape; (b) An actuator having MnO_2/Au electrode on both sides of PDMS strip (~ 0.5 × 2.5 cm^2) can bend toward to both directions.

Since the volume change only happened on the MnO_2/Au layer during the electrochemical reaction process, the actuator shown on Fig. 4.12a could only bend towards one direction. In order to make an actuator that could bend in both directions, a MnO_2/Au/PDMS/Au/MnO_2 sandwich design was used. Basically, the MnO_2/Au composite electrode was put on both sides of the PDMS layer. During the operation, one side of the MnO_2/Au electrode acted as the working electrode, while the other side of MnO_2/Au electrode worked as the counter electrode. For this case, the volume change along with the redox reaction of MnO_2 would happen alternatively, therefore the actuator could bend toward to both sides alternatively (Fig. 4.12b).

In this work, the concept of the electrochemical actuator based on the intercalation reaction of the energy storage material was shown. With different designs, the actuator can bend to one direction or two directions. However, for the real application, more study is still needed to characterize the actuators more systematically. Based on the same concept, other energy storage materials with more volume change during the intercalation reaction could also be promising and worthwhile for studying their application in electrochemical actuators.

4.7 Conclusions

The unique combination of characteristics that comprise this actuation system creates one of the most facile, yet versatile fabrication methods for creating PAO. This work will give engineers new approaches for designing active printed electronic systems. These actuators are light-weight, low-cost and enable rapid prototyping. Designs can be created

with CAD programs and printed in real time. These new devices are likely to find great utility as actuators, printed robots and active origami. The light weight aspect might allow new satellites and space exploration vehicles to be created at much lower costs of development and deployment. Other innovations will benefit from printed multifunctional and adaptive structures, such as small aircraft design and construction, robotics that are created on demand and 3-D self-folding electronics – all from common plastic films. The thermal bimorph actuators also showed very great potential for the application as wide radiation detection sensors. The electrochemical bimorph actuators offer the actuation for the underwater applications which are beyond the ability of thermal bimorph actuators.

5 CARBON NANOTUBE ELECTRODES FOR LOW-PPB-LEVEL CHROMIUM(VI) DETECTION

5.1 Introduction to Cr(VI) Detection with Amperometric Technique

In amperometric-based sensing techniques, the potential between the working and reference electrodes is held constant at the redox potential of the detecting species. The current changes between working and counter electrodes are recorded when different concentrations of detecting species are added. Since the current change is linear with the concentration of the detecting species, it can be used for calculating the unknown concentration of the detected species. Due to the different redox potentials of each species, the amperometric technique is very selective. Here a printable technique was used to fabricate carbon nanotube (CNT)-based electrodes for the electrochemical detection of hexavalent chromium, Cr(VI). The CNT electrodes showed electrochemical current responses as high as 500 nA/ppb Cr(VI) when a large area electrode was used. The limit of detection was shown to be as low as 5 ppb Cr(VI). The electrode could be deposited on multiple substrates, including fluorine-doped tin oxide (FTO) conducting glass, gold coated flexible plastic, filter paper, and commercially available printed electrodes. H_2O_2 was demonstrated to be a selective reducer, and a H_2O_2 reduction technique was developed for the Cr(VI) detection, which also could be integrated with normal amperometric detection methods. A flow detection system based on CNT/printed electrodes was also demonstrated, which could be potentially used for the real-time monitoring of Cr(VI) levels in flowing water.

5.2 Experimental Details

5.2.1 Carbon Nanotube Paste

To fabricate the carbon nanotube (CNT) electrodes, 18 mg of P3 CNTs (Carbon Solutions) was dispersed in 5 mL of a 50:50 water: ethanol solution (by volume) by sonicating for 20 min with a probe sonicator in pulse mode to make a CNT paste.

5.2.2 Fabrication of Carbon Nanotube Electrodes

A series of different electrodes were prepared using the CNT paste. The paste was uniformly coated with a spatula onto FTO glass to make a ~1 cm^2 working electrode. To serve as a comparison, a gold film electrode was made by sputtering gold onto FTO glass directly.

For the flexible electrode, a PET (polyethylene terephthalate) plastic sheet was coated with Ti for 5 min then Au for 10 min using a sputtering coater. Then the CNT paste was coated on top of the metal layers with a spatula.

Screen printed carbon electrodes (part#: RRPE1002C) were obtained from Pine Research Instrumentation. The CNT paste was coated on the rectangular carbon working electrode with a spatula.

The CNT paste was directly painted or filtered through filter paper to fabricate a CNT coated filter paper electrode with about 30 cm^2 active area.

5.2.3 Electrochemical Measurements

A three-electrode set up was used to measure the concentration of Cr(VI), in which Pt wire worked as counter electrode while a saturated calomel electrode (SCE) was used as reference electrode. In the printed electrodes case, the printed carbon electrode coated

with CNT paste was used as the working electrode, while the counter and reference electrodes were used as they were.

All measurements were performed on BioLogic SP-150 electrochemical potentiostat. Different concentrations of Cr(VI) ($K_2Cr_2O_7$ solution) were dissolved in 0.1 M HCl. Cyclic voltammetry (CV) and amperometric measurements were used to determine the Cr(VI)/Cr(III) redox reaction peak and Cr(VI) concentration, respectively.

5.2.4 Water Samples

Most measurements were conducted in 0.1 M HCl in nanopure water solution. For the real water case, samples were collected from 7 different sites at the Santan Generating Station in Gilbert, AZ, labelled Sites A through G as shown in Fig. 5.1. Detailed information regarding the different samples is shown in Table 5.1. In this report, the F sample was used, representing the blowdown from cooling towers 1 – 4, for the real sample test.

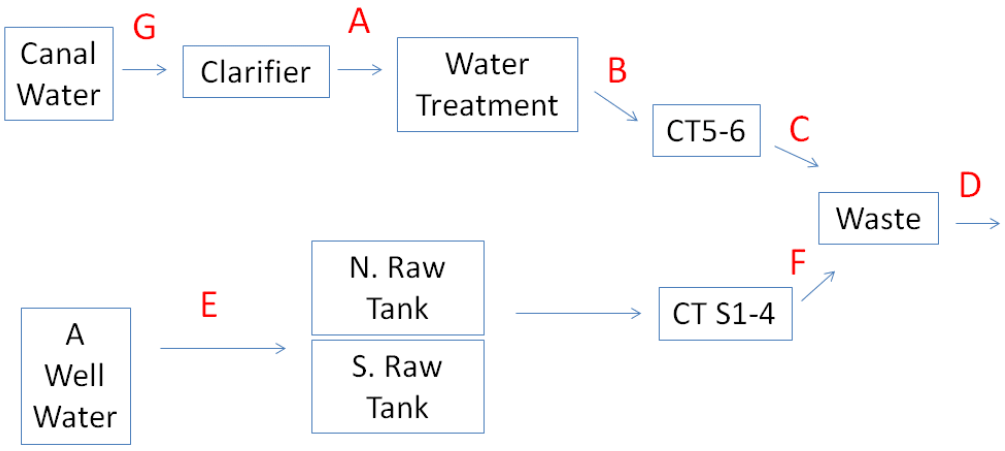

Figure 5.1 Sample sites for SRP water tests.

Table 5.1 Descriptions for the water samples

Site	Description
A	Raw canal water after clarifier
B	Canal water discharge from service water tank, chlorinated
C	CT-6 blowdown discharge, with bisulfite, de-chlorinated
D	Final plant discharge waste (ST-005)
E	Discharge from A well
F	CT1-4 blowdown discharge, de-chlorinated
G	Raw canal water before clarifier

5.3 Characterization of CNT Electrode for Cr(VI) Detection

Fig. 5.2 shows a typical scanning electron microscopy (SEM) image of CNTs after they were coated as a paste onto FTO glass. The CNT bundles form a net-like film, which has very good electric conductivity, while the pores allow for access of the electrolyte and Cr(VI) ions.

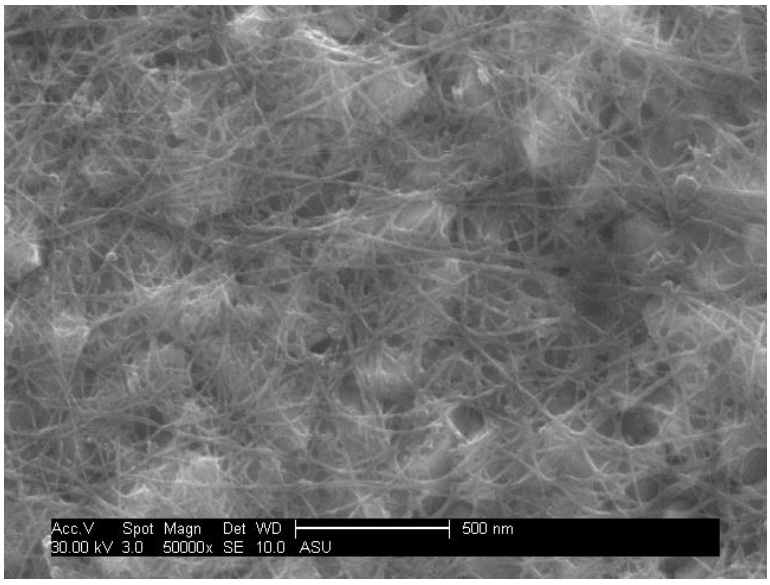

Figure 5.2 SEM image of CNT on FTO glass.

To evaluate the performance of the CNT as electrode materials for Cr(VI) detection, a three-electrode configuration was used in 0.1 M HCl electrolyte. The cyclic voltammetry (CV) curves from -0.1 to 0.6 V vs. SCE for electrodes made from CNTs and gold film on FTO are shown in Fig. 5.3a and b, respectively. The Cr(VI) to Cr(III) reduction ($HCrO_4^- + 7H^+ + 3e^- \rightarrow Cr^{3+} + 4H_2O$) peaks are at 0.25 and 0.315 V vs. SCE for the CNT and gold electrodes, respectively. Although, due to the high capacitance current, the reduction peak on the CNT electrode is not very obvious, when Cr(VI) concentration increased to 20 ppm, the net peak current change is still significant.

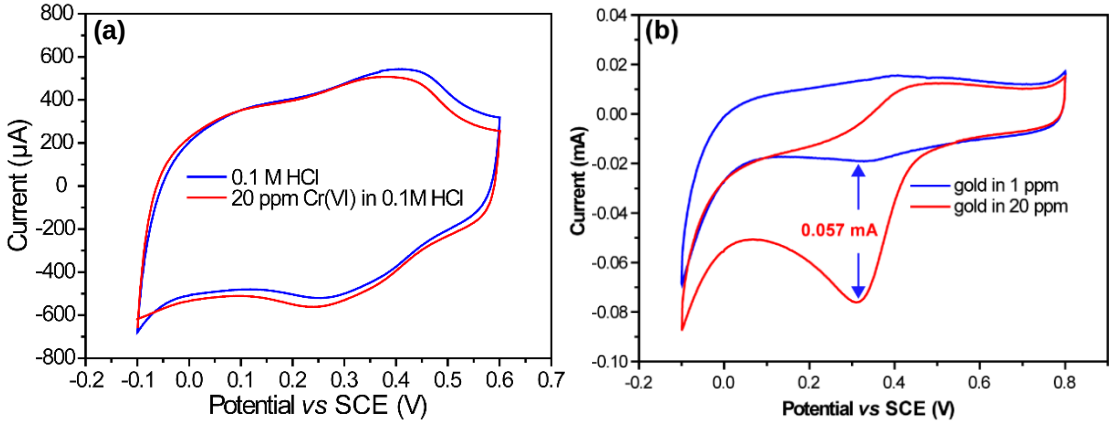

Figure 5.3 CV curves of different electrodes in different concentrations of Cr(VI) solution. (a). CVs of CNT electrodes. (b) CVs of gold film electrode.

To evaluate the sensitivity and reliability of the CNT electrode for Cr(VI) detection, amperometric measurements were conducted in 0.1 M HCl electrolyte. Different concentrations of Cr(VI) (5, 10, 20, 40, and 100 ppb) were injected into the stirred electrolyte while the potential was held at 0.21 V vs. SCE (Fig. 5.4a). After each injection, the current would change towards more negative values due to the reduction of Cr(VI). By fitting and subtracting different periods of the curves before and after the injection, the

reduction current versus Cr(VI) concentration was obtained as shown in Fig. 5.5a, which has very good linearity and shows the electrode has a sensitivity of 21.65 nA/ppb Cr(VI). To evaluate the reproducibility of the electrode, the CNT electrode was thoroughly rinsed with nanopure water and dried with a heat gun. The amperometric curve of the recovered CNT electrode is shown in Fig. 5.4b. By comparing with Fig. 5.4a, it can be seen clearly that the sensitivity almost remains the same, which shows that the CNT electrode has very good reproducibility.

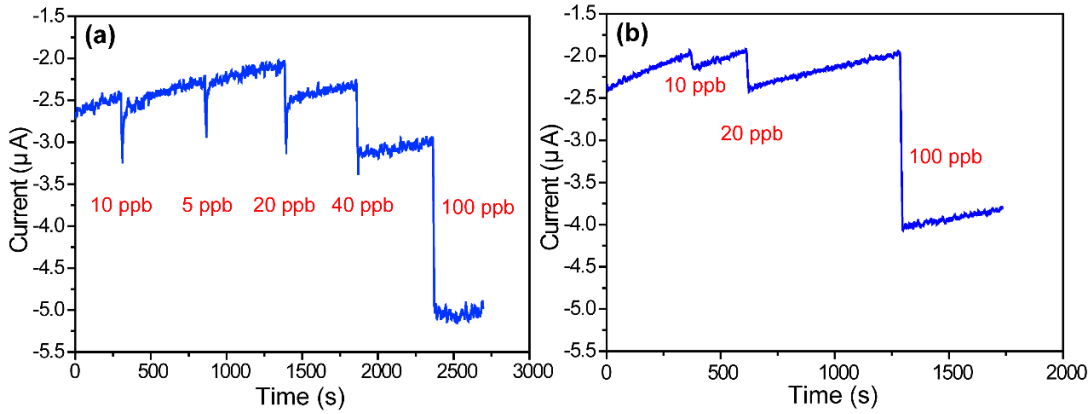

Figure 5.4 Amperometric response of CNT electrode at 0.21 V when different concentrations of Cr(VI) were add into 0.1 M HCl. (a) original CNT electrode, (b) recovered CNT electrode.

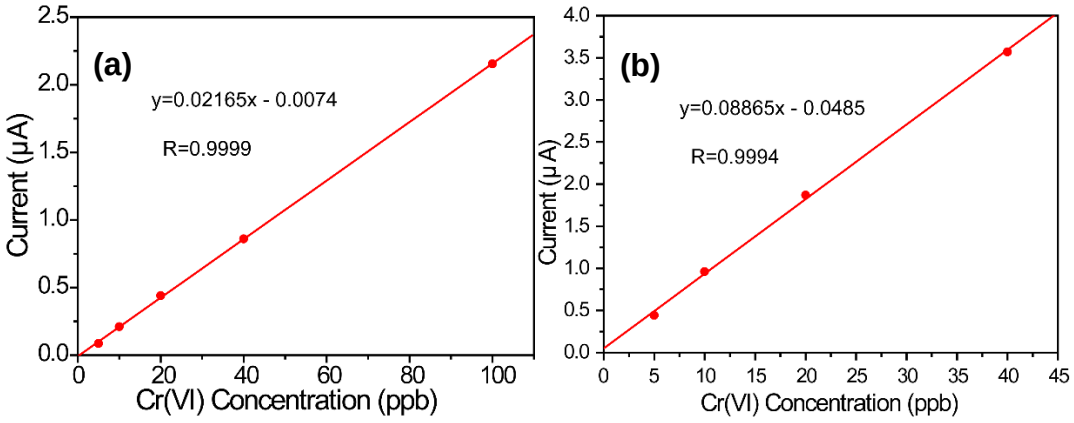

Figure 5.5 The reduction current versus Cr(VI) concentrations at different levels. (a) CNT on FTO electrode, (b) CNT on gold coated PET electrode.

In order to make a flexible electrode so that it can be put inside of a water pipe for real time monitoring, a gold coated PET plastic sheet was used as the substrate for the CNT electrode. Due to the flexibility of this electrode, it can be wrapped the sheet into a roll shape so that it can fit into a small volume while maintaining a relatively larger working area. Fig. 5.6 shows the amperometric measurement of the CNT electrode on gold coated PET (5 cm x 1 cm), which has around 5 times more area than the CNT on FTO electrode. The relative reduction current versus concentration plot is shown in Fig. 5.5b. With the larger working area, the sensitivity was increased to almost 90 nA/ppb, while the linearity was still well maintained. Although the noise in the signal was still relatively high, the current change of even 5 ppb level injection was significant compared with that in Fig. 5.4a. The dependence of sensitivity on the electrode working area also offers another way to increase the detection limit of the electrode with the additional benefit of the electrode being flexible. This will be further studied in future research to find the limitation of this detection method.

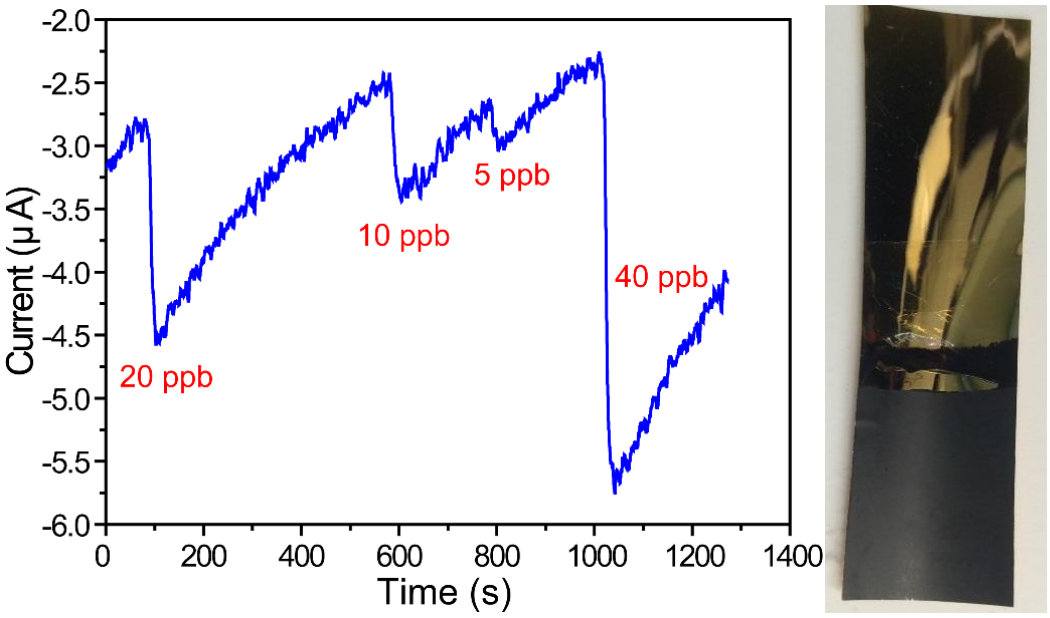

Figure 5.6 Amperometric response of CNT on gold coated PET electrode at 0.21 V when different concentrations of Cr(VI) were injeted into 0.1 M HCl, and the picture of the corresponding electrode (CNT coated area: ~1.5 cm x 2 cm).

5.4 CNT/Filter Paper Flexible Electrodes for Cr(VI) Detection

Due to its smooth surface, the gold coated plastic sheet does not promote good adhesion with the CNT layer, which makes it hard to fabricate large area uniform electrodes. To solve this problem, CNT coated filter paper electrodes were developed (Fig. 5.7b). Due the high porosity of the filter paper, the CNT paste could be easily uniformly coated onto the filter paper. The CNT paste could even be filtered through the filter paper to form the electrode very quickly. Due to the high conductivity of the CNTs, the resistance of CNT/filter paper electrode is only several tens of ohms. Nonetheless, to ensure a good electrical connection with the CNT/filter paper electrode, a layer of silver paint was coated on the edge of the electrode for the contact to the potentiostat. As shown in Fig. 5.7b, a layer of polyvinylidene fluoride (PVDF) was used to cover the top area of the electrode in

order to restrict the electrochemical reaction to only the CNT active area. The layer also prevents the solution from wetting the top area that was coated with silver paint.

Because of the large active area (~30 cm^2) and high porosity of the filter paper, the sensitivity of the CNT/filter paper electrodes was as high as ~500 nA/ppb. Although the noise also increased to around 1 μA, the signal to noise ratio still improved significantly compared to the CNT/FTO or CNT/Au-PET electrodes. As Fig. 5.7a shows, even 5 ppb Cr(VI) addition can cause a significant current change (2.5 μA), while the current change is linear to the concentration of Cr(VI). The influence of Cr(III) was also tested. Even adding 200 ppb of Cr(III) did not cause any noticeable current change, indicating that the electrode is very selective for Cr(VI).

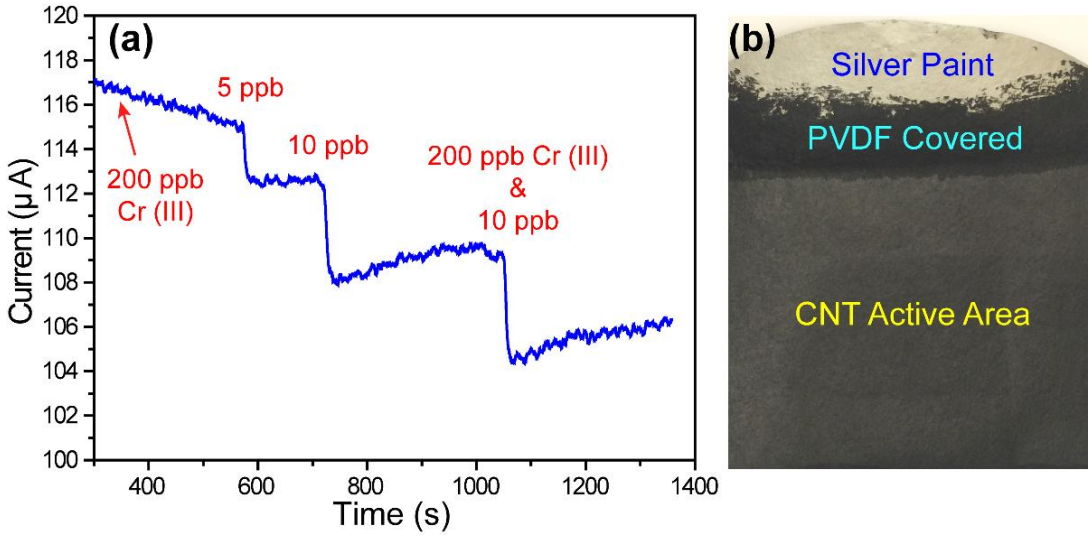

Figure 5.7 (a) Amperometric response of CNT coated filter paper electrode at 0.21 V when different concentrations of Cr(VI) or Cr(III) were injected into 0.1 M HCl. (b) The picture of the corresponding CNT coated filter paper electrode (CNT active area: ~ 5 cm x 6 cm).

5.5 CNT Coated Printed Electrodes for Cr(VI) Detection

Although the CNT/filter paper electrode had much better sensitivity due to its high surface area, its high capacitive current from adsorption of ions at the electric double layer made the relaxation time to reach the equilibrium very long. This characteristic is not ideal for practical applications where real-time monitoring might be desired. For more practical applications, a CNT modified commercial printed electrode was developed (Fig. 5.8c). As the picture shows, the CNTs were coated on the working electrode area of the commercial printed electrodes, while the counter and reference electrodes were embedded in the printed electrodes.

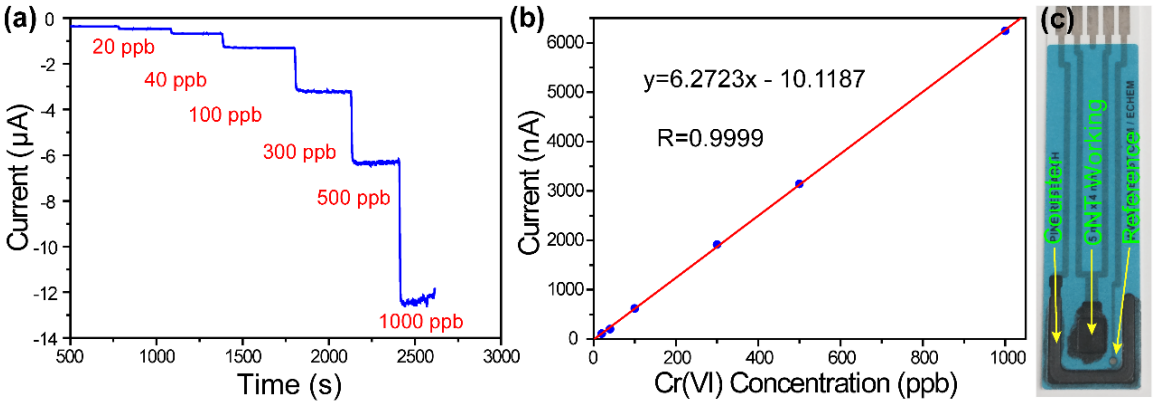

Figure 5.8 Standard addition measurement of Cr(VI) with CNT/printed electrodes. (a)The reduction current versus Cr(VI) concentrations, (b) the corresponding amperometric curve with different additions. (c) The picture of CNT coated printed electrode (1cm × 4 cm).

In the standard addition measurement, the current changed linearly with increasing Cr(VI) concentration up to 1000 ppb (Fig. 5.8a,b). The sensitivity was around 6.27 nA/ppb, while the noise also decreased significantly compared with that of the large CNT/filter paper electrode. More importantly, due to its smaller active area, the current could reach equilibrium quickly in just a few minutes. As Fig. 5.9a shows, when the amperometric

measurement was started in a solution of 0.1 M HCl nanopure water, the current stabilized in around 1 minute and remained unchanged for about 15 mins. After adding 20 ppb Cr(VI) in the solution and restarting the measurement, the current quickly reached the lower current and stabilized. When an additional 20 ppb Cr(VI) was added, the current further dropped by a similar amount. The influence of other ions was also checked further. As Fig. 5.9b shows, when up to 1 ppm Cr(III) and 40 ppb As(V) were added to the solution, they only caused small peaks on the amperometric curve, after which the current returned back to the original value. When even as high as 500 ppm Na_2SO_4 was added, the big sharp peak still quickly relaxed back to the original current level. After adding these high concentrations of ions, the current still responded with the same sensitivity when 40 ppb Cr(VI) was added (Fig. 5.9b), which means our CNT/printed electrode is very selective to Cr(VI).

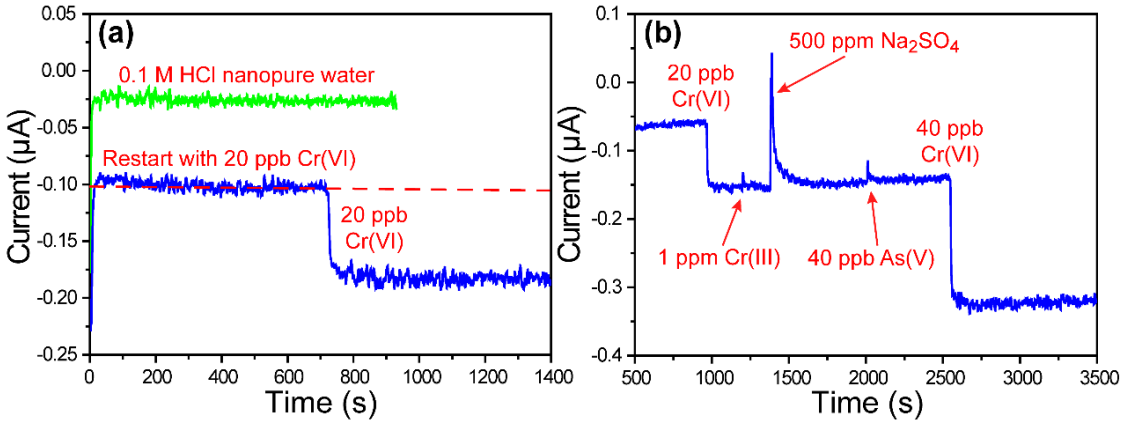

Figure 5.9 Amperometric response of CNT/printed electrode at 0.21 V. (a) stable current in 0.1 M HCl nanopure water (green), and restart the measurement with 20 ppb Cr(VI) added (blue); (b) the effect of other ions, like Cr(III), As(V) and Na_2SO_4.

Due to the small active area and short response time for the CNT/printed electrode, these electrodes were determined to be the most promising for Cr(VI) detection in the real water. Compared to the synthetic water samples containing 0.1 M HCl, the real water samples will have many other ionic and dissolved species that may affect the measurement. In order to maintain the same background current, a partially replacing background solution (PRBS) technique was developed so that this electrode could be used for the detection of Cr(VI) in real water. First, concentrated HCl was added to 50 mL of real water to make a 0.1 M solution, which was then exposed to a 0.21 V vs. SCE bias long enough (~ 2 h) so that all of the Cr(VI) in solution was completely reduced to Cr(III), while the other dissolved ions remained unchanged. Then, 25 mL of fully reduced solution was replaced with 25 mL of fresh solution (the same real water with 0.1 M HCl). During this whole process, the electrodes were immersed in the solution at all times, so that the electric double layer on the surface of the electrodes would not be perturbed and there would be no current change due to the capacitance effect. Because of the small active area and thin electrode connection wires (Fig. 5.8c), the capacitance change was very small during the PRBS process. However, for the CNT/filter paper large electrode, even with the active area immersed in the solution all the time, due to the large PVDF coated conducting area, the capacitance between the PVDF covered CNT and the solution would change significantly enough to cause big current change. For this reason, the small CNT/printed electrode is preferred for testing Cr(VI) concentrationa in real water with the PRBS techniques.

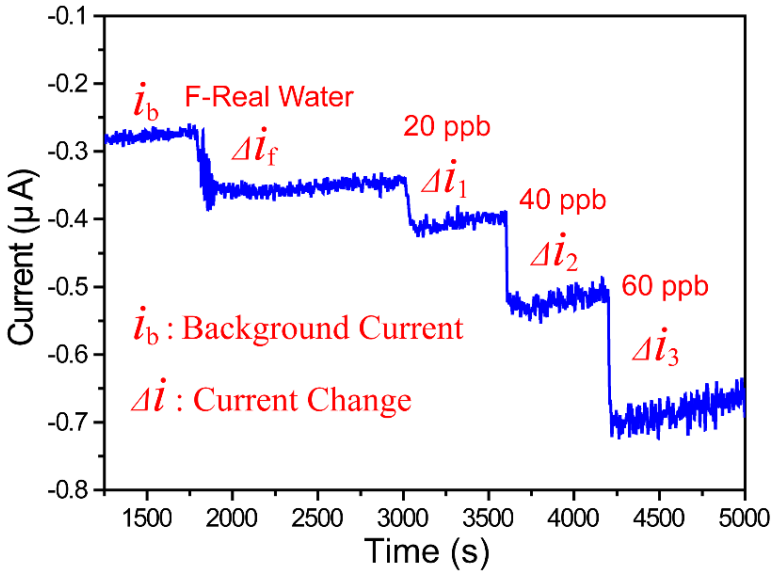

Figure 5.10 Amperometric response of CNT/printed electrode at 0.21 V vs. SCE when half of the reduced F real water was replaced with original one and different concentrations of Cr(VI) were injected into 0.1 M HCl sample F real water.

As an example, the sample F real water was used to test with this technique. As shown in Fig. 5.10, the background current when applying 0.21 V vs. SCE onto the CNT/printed electrode in 50 mL of reduced sample F real water with 0.1 M HCl is i_b. Since the Cr(VI) was reduced from the solution, this background current is due to the adsorption of other ions or potentially even side reactions with other constituents in the water. Then 25 mL of reduced background solution was replaced with 25 mL of fresh solution, which contains the unknown amount of Cr(VI). The addition of the fresh solution at ~30 min, caused a current drop Δi_f that corresponds to half of the concentration Cr(VI) in the sample F real water. After the current stabilized at new equilibrium value, standard additions of 20 ppb, 40 ppb, and 60 ppb Cr(VI) were conducted continuously so that the current changes, Δi_1, Δi_2, and Δi_3, could be used for calibration. Based on the calibration current changes, the

Cr(VI) concentration in sample F water corresponded to 2 Δi_f and was calculated to be ~52 ppb, which is very close to the value measured by UV-Vis spectroscopy of 52.8 ppb. It was noted that the Cr(VI) levels in the site F water are not typically this high, but due to the long time between the sampling and testing, there could have been water evaporation that led to the concentration of Cr(VI). These tests show that this method can be successfully used to determine the amount of Cr(VI) in the cooling tower blowdown using the CNT-based electrodes.

5.6 Flow Detection System with CNT/Printed Electrodes and H_2O_2 Reduction Method

A flow system for Cr(VI) detection was further developed using the CNT/printed electrodes (Fig. 5.11b). Specifically, the CNT modified printed electrode was placed between two pieces of glasses, which were spaced by two small pieces of glass to form a channel. Then the glass and electrodes were sealed and bonded together with epoxy. Meanwhile, the thin plastic tubes were also sealed inside the channel to enable the solution to flow in and out (Fig. 5.11b). During the measurement, the solution was pumped through the channel with a peristaltic pump or syringe pump. Fig. 5.11a shows the test results with this system. Initially, the background solution, 0.1 M HCl nanopure water in this case, was flowing through the channel until the background current was stable at i_b. Then, different concentrations of Cr(VI) were added into the solution and caused the corresponding current changes Δi, with the current changing linearly with the addition of Cr(VI). The final current was stable at i_f.

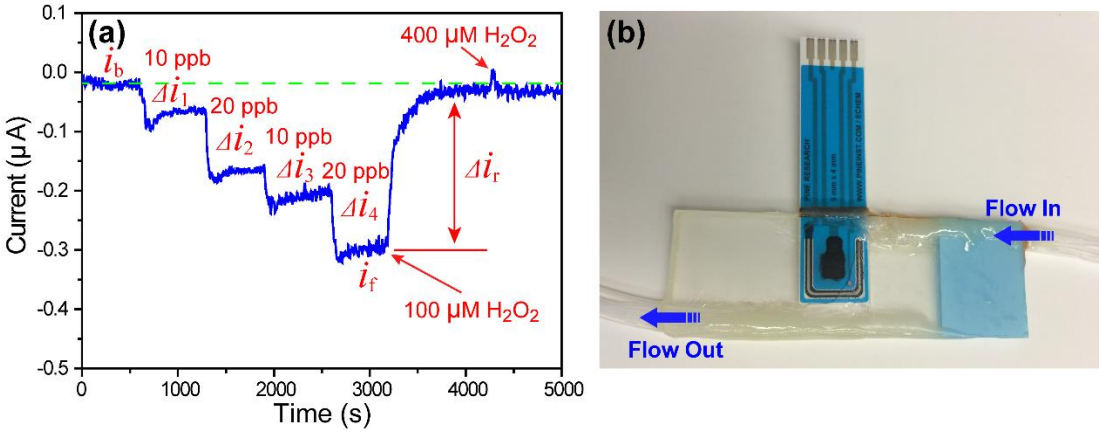

Figure 5.11 (a) Amperometric response of CNT/printed electrode at 0.21 V when different concentrations of Cr(VI) or H_2O_2 were injected into 0.1 M HCl with the flow system. (b) The picture of corresponding CNT coated printed electrode flow detection system.

In a measurement where an unknown amount of Cr(VI) is to be quantified, the background current must first be established. After the current is stable for the background solution, the test solution could be switched in (i.e. with a valve) and flowed through the system. The corresponding current change could then be used for calculating the unknown Cr(VI) concentration. Since Cr(VI) can be reduced by hydrogen peroxide with follow reaction:[190]

$$2HCrO_4^- + 3\ H_2O_2 + 8\ H^+ \rightarrow 2\ Cr^{3+} + 8\ H_2O + 3\ O_2$$

a H_2O_2 reduction technique was developed. In this technique, H_2O_2 does not just act as a normal reducing agent. Unlike other reducing agents for Cr(VI), H_2O_2 can form an unstable compound with Cr(VI), chromium peroxide, which will further decompose to Cr(III).[190] This unique reaction makes H_2O_2 very selective to Cr(VI) reduction.

The H_2O_2 was integrated into our flow detection system. As Fig. 5.11a shows, after standard additions of different concentrations of Cr(VI), the final current was stable at i_f,

then 100 μM H_2O_2, about 100 times of total Cr(VI), was added into the system. Then the current increased Δi_r, back to the original background value, since Cr(VI) was reduced to Cr(III) that is nonactive to our electrodes. After the current reached the equilibrium value, further addition of 400 μM H_2O_2 did not cause any more current change, which meant H_2O_2 itself is not active to the electrodes. So, for the real test, after the current is stable at i_f in the sample solution, H_2O_2 is added to reduce Cr(VI) and cause current change Δi_r, which then could be used to calculate the concentration of Cr(VI) in the sample solution.

The data in Fig. 5.11a demonstrate the proof-of-concept, but since the background solution (0.1 M HCl) did not contain Cr(VI), additional tests were performed using the H_2O_2 reduction technique with the flow system for F real water, which contains the unknown amount of Cr(VI) (Fig. 5.12). Since the electrode was the same one used in 0.1 M HCl pure water and not stabilized in the F real water condition, the initial current baseline kept increasing due to the equilibrium process of the electrodes in the high ionic concentration real water solution. When 20 ppb Cr(VI) was added to the system, a current drop Δi_1 = ~81 nA was achieved, which will be used as the calibration. Then, when 100 μM H_2O_2 was added to the system, the current increased toward to positive value and stabilized at i_b. By linear fitting the baseline current to eliminate the capacitance current caused by the adsorption of ions in the electric double layer, the current change due to Cr(VI) reduction in the original F real water, Δi_r, was calculated to be ~250 nA. With the calibration current change Δi_1 = ~81 nA for 20 ppb Cr(VI), the Cr(VI) concentration in F real water was determined to be $\Delta i_r/\Delta i_1$*20 ppb = 61.7 ppb, which is higher than the values obtained with PRBS and UV-Vis techniques, 52 ppb and 52.8 ppb, respectively. This discrepancy is likely due to the unstable baseline current. If the electrodes were pre-stabilized in the F real water

solution first before the test, the results should be more accurate, which will be studied further for future work to make this technique more stable for practical applications.

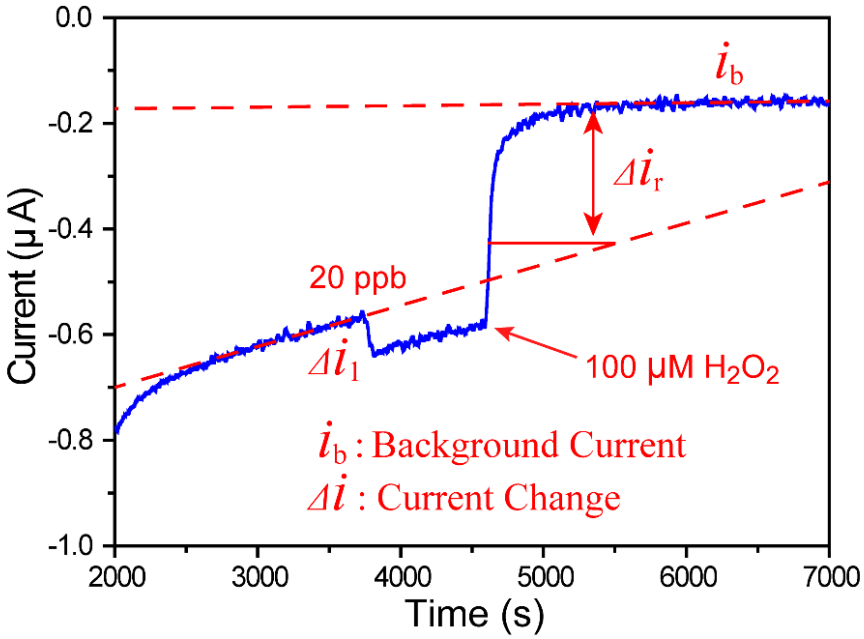

Figure 5.12 Amperometric response of CNT/printed electrode at 0.21 V when 20 ppb Cr(VI) or H_2O_2 were injected into 0.1 M HCl F real water with the flow system.

To summarize, Fig. 5.13 shows the evolution of the electrodes developed in this project. For each iteration, one or more problems were solved and the technique was improved. Finally, a commercial printed electrodes based flow test system was developed, which is very promising for practical application. In the future, the system and the technique will be improved further. And a microfluidic-like system would be developed so that the test could be more stable, faster and more accurate.

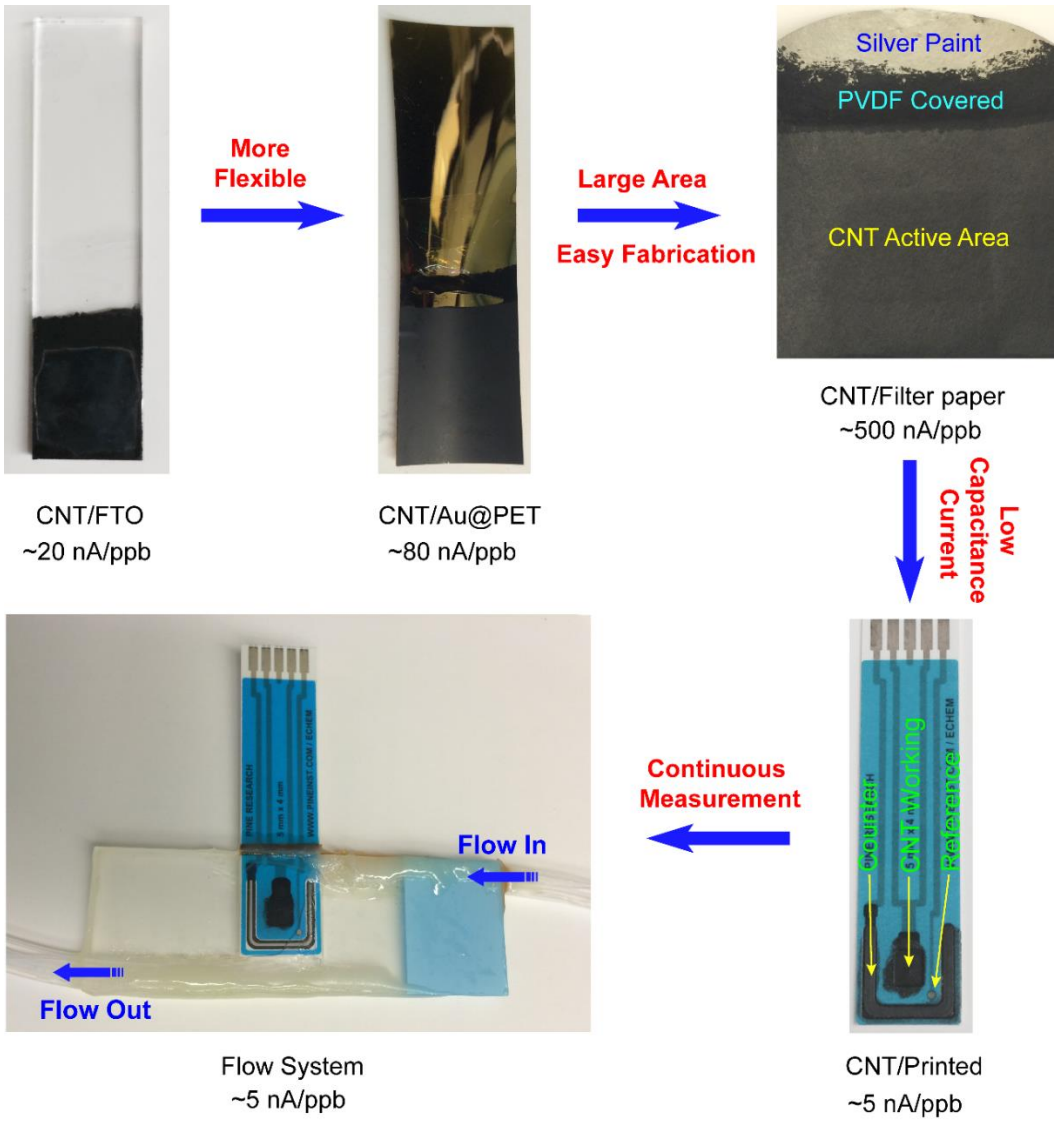

Figure 5.13 The summary of the electrodes evolution in this work.

5. 7 Conclusion

In summary, a very facile and sensitive Cr(VI) detection technique has been demonstrated, which shows much higher sensitivity to Cr(VI) than former reported carbon electrodes and even noble metal electrodes. A flexible electrode was successfully demonstrated. CNT modified commercial available printed electrodes was also developed, which is very promising for practical, cheap, facile-made electrodes of Cr(VI) detection.

The H_2O_2 reduction technique was also demonstrated, which could also be combined with the normal amperometric method. The flow system based on the printed electrodes makes the detection even suitable for real-time monitoring.

6 REFERENCES

(1) Kroto, H. W.; Heath, J. R.; O'Brien, S. C.; Curl, R. F.; Smalley, R. E. C60: Buckminsterfullerene. *Nature* **1985**, *318*, 162–163.

(2) Plume, A. Buckyballs, Nanotubes and Graphene: On the Hunt for the next Big Thing. *Res. trends* **2010**, 6–7.

(3) Nguyen, K. T.; Zhao, Y. Integrated Graphene/nanoparticle Hybrids for Biological and Electronic Applications. *Nanoscale* **2014**, *6*, 6245–6266.

(4) Zhu, Y.; Murali, S.; Stoller, M. D.; Ganesh, K. J.; Cai, W.; Ferreira, P. J.; Pirkle, A.; Wallace, R. M.; Cychosz, K. a; Thommes, M.; *et al.* Carbon-Based Supercapacitors Produced by Activation of Graphene. *Science* **2011**, *332*, 1537–1541.

(5) Yoo, J. J.; Balakrishnan, K.; Huang, J.; Meunier, V.; Sumpter, B. G.; Srivastava, A.; Conway, M.; Reddy, A. L. M.; Yu, J.; Vajtai, R.; *et al.* Ultrathin Planar Graphene Supercapacitors. *Nano Lett.* **2011**, *11*, 1423–1427.

(6) Lin, J.; Zhang, C.; Yan, Z.; Zhu, Y.; Peng, Z.; Hauge, R. H.; Natelson, D.; Tour, J. M. 3-Dimensional Graphene Carbon Nanotube Carpet-Based Microsupercapacitors with High Electrochemical Performance. *Nano Lett.* **2013**, *13*, 72–78.

(7) Luo, J.; Jang, H. D.; Huang, J. Effect of Sheet Morphology on the Scalability of Graphene-Based Ultracapacitors. *ACS Nano* **2013**, *7*, 1464–1471.

(8) Simon, P.; Gogotsi, Y. Materials for Electrochemical Capacitors. *Nat. Mater.* **2008**, *7*, 845–854.

(9) Wang, C.; Waje, M.; Wang, X.; Tang, J. M.; Haddon, R. C. Proton Exchange Membrane Fuel Cells with Carbon Nanotube Based Electrodes. *Nano Lett.* **2004**, *4*, 345–348.

(10) Gong, K.; Du, F.; Xia, Z.; Durstock, M.; Dai, L. Nitrogen-Doped Carbon Nanotube Arrays with High Electrocatalytic Activity for Oxygen Reduction. *Science* **2009**, *323*, 760–764.

(11) Wang, H.; Yang, Y.; Liang, Y.; Robinson, J. T.; Li, Y.; Jackson, A.; Cui, Y.; Dai, H. Graphene-Wrapped Sulfur Particles as a Rechargeable Lithium-Sulfur Battery Cathode Material with High Capacity and Cycling Stability. *Nano Lett.* **2011**, *11*, 2644–2647.

(12) Hu, L.; Wu, H.; La Mantia, F.; Yang, Y.; Cui, Y. Thin, Flexible Secondary Li-Ion Paper Batteries. *ACS Nano* **2010**, *4*, 5843–5848.

(13) Kongkanand, A.; Dom ńguez, R. M.; Kamat, P. V. Single Wall Carbon Nanotube Scaffolds for Photoelectrochemical Solar Cells. Capture and Transport of Photogenerated Electrons. *Nano Lett.* **2007**, *7*, 676–680.

(14) Ostojic, G. N.; Liang, Y. T.; Hersam, M. C. Catalytically Active Nanocomposites of Electronically Coupled Carbon Nanotubes and Platinum Nanoparticles Formed via Vacuum Filtration. *Nanotechnology* **2009**, *20*, 434019.

(15) Huang, J.; Ng, A. L.; Piao, Y.; Chen, C.-F.; Green, A. a; Sun, C.-F.; Hersam, M. C.; Lee, C. S.; Wang, Y. Covalently Functionalized Double-Walled Carbon Nanotubes Combine High Sensitivity and Selectivity in the Electrical Detection of Small Molecules. *J. Am. Chem. Soc.* **2013**, *135*, 2306–2312.

(16) Jariwala, D.; Sangwan, V. K.; Lauhon, L. J.; Marks, T. J.; Hersam, M. C. Carbon Nanomaterials for Electronics, Optoelectronics, Photovoltaics, and Sensing. *Chem. Soc. Rev.* **2013**, *42*, 2824–2860.

(17) Sohn, K.; Joo Na, Y.; Chang, H.; Roh, K.-M.; Dong Jang, H.; Huang, J. Oil Absorbing Graphene Capsules by Capillary Molding. *Chem. Commun.* **2012**, *48*.

(18) Sun, H.; Xu, Z.; Gao, C. Multifunctional, Ultra-Flyweight, Synergistically Assembled Carbon Aerogels. *Adv. Mater.* **2013**, *25*, 2554–2560.

(19) Peigney, A.; Laurent, C.; Flahaut, E.; Bacsa, R. R.; Rousset, A. Specific Surface Area of Carbon Nanotubes and Bundles of Carbon Nanotubes. *Carbon* **2001**, *39*, 507–514.

(20) Liang, Y. T.; Hersam, M. C. Highly Concentrated Graphene Solutions via Polymer Enhanced Solvent Exfoliation and Iterative Solvent Exchange. *J. Am. Chem. Soc.* **2010**, *132*, 17661–17663.

(21) Strubel, P.; Thieme, S.; Biemelt, T.; Helmer, A.; Oschatz, M.; Br ückner, J.; Althues, H.; Kaskel, S. ZnO Hard Templating for Synthesis of Hierarchical Porous Carbons with Tailored Porosity and High Performance in Lithium-Sulfur Battery. *Adv. Funct. Mater.* **2015**, *25*, 287–297.

(22) Sevilla, M.; Fuertes, A. B. A. Direct Synthesis of Highly Porous Interconnected Carbon Nanosheets and Their Application as High-Performance Supercapacitors. *ACS Nano* **2014**, *8*, 5069–5078.

(23) Fan, X.; Yu, C.; Yang, J.; Ling, Z.; Hu, C.; Zhang, M.; Qiu, J. A Layered-Nanospace-Confinement Strategy for the Synthesis of Two-Dimensional Porous Carbon Nanosheets for High-Rate Performance Supercapacitors. *Adv. Energy Mater.* **2014**, *5*, DOI: 10.1002/aenm.201401761.

(24) Xing, W.; Huang, C. C.; Zhuo, S. P.; Yuan, X.; Wang, G. Q.; Hulicova-Jurcakova, D.; Yan, Z. F.; Lu, G. Q. Hierarchical Porous Carbons with High Performance for Supercapacitor Electrodes. *Carbon* **2009**, *47*, 1715–1722.

(25) Wang, D.-W.; Li, F.; Liu, M.; Lu, G. Q.; Cheng, H.-M. 3D Aperiodic Hierarchical Porous Graphitic Carbon Material for High-Rate Electrochemical Capacitive Energy Storage. *Angew. Chem. Int. Ed. Engl.* **2008**, *47*, 373–376.

(26) Hampsey, J. E.; Hu, Q.; Wu, Z.; Rice, L.; Pang, J.; Lu, Y. Templating Synthesis of Ordered Mesoporous Carbon Particles. *Carbon* **2005**, *43*, 2977–2982.

(27) Xia, Y.; Xiao, Z.; Dou, X.; Huang, H.; Lu, X.; Yan, R.; Gan, Y.; Zhu, W.; Tu, J.; Zhang, W.; *et al.* Green and Facile Fabrication of Hollow Porous MnO/C Microspheres from Microalgaes for Lithium-Ion Batteries. *ACS Nano* **2013**, *7*, 7083–7092.

(28) Han, F.-D.; Bai, Y.-J.; Liu, R.; Yao, B.; Qi, Y.-X.; Lun, N.; Zhang, J.-X. Template-Free Synthesis of Interconnected Hollow Carbon Nanospheres for High-Performance Anode Material in Lithium-Ion Batteries. *Adv. Energy Mater.* **2011**, *1*, 798–801.

(29) Wang, X.; Zhang, Y.; Zhi, C.; Wang, X.; Tang, D.; Xu, Y.; Weng, Q.; Jiang, X.; Mitome, M.; Golberg, D.; *et al.* Three-Dimensional Strutted Graphene Grown by Substrate-Free Sugar Blowing for High-Power-Density Supercapacitors. *Nat. Commun.* **2013**, *4*, 2905.

(30) Wang, Q.; Yan, J.; Wang, Y.; Ning, G.; Fan, Z.; Wei, T.; Cheng, J.; Zhang, M.; Jing, X. Template Synthesis of Hollow Carbon Spheres Anchored on Carbon Nanotubes for High Rate Performance Supercapacitors. *Carbon* **2013**, *52*, 209–218.

(31) Ma, F.; Zhao, H.; Sun, L.; Li, Q.; Huo, L.; Xia, T.; Gao, S.; Pang, G.; Shi, Z.; Feng, S. A Facile Route for Nitrogen-Doped Hollow Graphitic Carbon Spheres with Superior Performance in Supercapacitors. *J. Mater. Chem.* **2012**, *22*, 13464–13468.

(32) Pech, D.; Brunet, M.; Durou, H.; Huang, P.; Mochalin, V.; Gogotsi, Y.; Taberna, P.-L.; Simon, P. Ultrahigh-Power Micrometre-Sized Supercapacitors Based on Onion-like Carbon. *Nat. Nanotechnol.* **2010**, *5*, 651–654.

(33) Wu, Z.-Y.; Li, C.; Liang, H.-W.; Zhang, Y.-N.; Wang, X.; Chen, J.-F.; Yu, S.-H. Carbon Nanofiber Aerogels for Emergent Cleanup of Oil Spillage and Chemical Leakage under Harsh Conditions. *Sci. Rep.* **2014**, *4*, 4079.

(34) Sun, S.; Jaouen, F.; Dodelet, J.-P. Controlled Growth of Pt Nanowires on Carbon Nanospheres and Their Enhanced Performance as Electrocatalysts in PEM Fuel Cells. *Adv. Mater.* **2008**, *20*, 3900–3904.

(35) Su, F.; Tian, Z.; Poh, C. K.; Wang, Z.; Lim, S. H.; Liu, Z.; Lin, J. Pt Nanoparticles Supported on Nitrogen-Doped Porous Carbon Nanospheres as an Electrocatalyst for Fuel Cells †. *Chem. Mater.* **2010**, *22*, 832–839.

(36) Yang, S.-T.; Cao, L.; Luo, P. G.; Lu, F.; Wang, X.; Wang, H.; Meziani, M. J.; Liu, Y.; Qi, G.; Sun, Y.-P. Carbon Dots for Optical Imaging in Vivo. *J. Am. Chem. Soc.* **2009**, *131*, 11308–11309.

(37) Joo, J. B.; Kim, P.; Kim, W.; Kim, J.; Kim, N. D.; Yi, J. Simple Preparation of Hollow Carbon Sphere via Templating Method. *Curr. Appl. Phys.* **2008**, *8*, 814–817.

(38) Titirici, M.-M.; Thomas, a.; Antonietti, M. Replication and Coating of Silica Templates by Hydrothermal Carbonization. *Adv. Funct. Mater.* **2007**, *17*, 1010–1018.

(39) Yan, Y.; Zhang, F.; Meng, Y.; Tu, B.; Zhao, D. One-Step Synthesis of Ordered Mesoporous Carbonaceous Spheres by an Aerosol-Assisted Self-Assembly. *Chem. Commun.* **2007**, *1*, 2867–2869.

(40) Sun, Y.-P.; Zhou, B.; Lin, Y.; Wang, W.; Fernando, K. a S.; Pathak, P.; Meziani, M. J.; Harruff, B. a; Wang, X.; Wang, H.; *et al.* Quantum-Sized Carbon Dots for Bright and Colorful Photoluminescence. *J. Am. Chem. Soc.* **2006**, *128*, 7756–7757.

(41) Zou, Q.; Wang, M. Z.; Li, Y. G.; Lu, B. High-Resolution Transmission-Electron Microscope Characterization of Onionlike Carbon Transformed from Nanodiamond. *J. Vac. Sci. Technol. B Microelectron. Nanom. Struct.* **2010**, *28*, 935.

(42) N. Sano, H. Wang, M. Chhowalla, I. Alexandrou, G. A. J. A. Nanotechnology: Synthesis of Carbon'onions' in Water. *Nature* **2001**, *414*, 506–507.

(43) Choucair, M.; Stride, J. A. The Gram-Scale Synthesis of Carbon Onions. *Carbon* **2012**, *50*, 1109–1115.

(44) Tang, K.; Fu, L.; White, R. J.; Yu, L.; Titirici, M.-M.; Antonietti, M.; Maier, J. Hollow Carbon Nanospheres with Superior Rate Capability for Sodium-Based Batteries. *Adv. Energy Mater.* **2012**, *2*, 873–877.

(45) Yao, C.; Shin, Y.; Wang, L.; Windisch, C. F.; Samuels, W. D.; Arey, B. W.; Wang, C.; Risen, W. M.; Exarhos, G. J. Hydrothermal Dehydration of Aqueous Fructose Solutions in a Closed System. *J. Phys. Chem. C* **2007**, 15141–15145.

(46) Liu, H.; Ye, T.; Mao, C. Fluorescent Carbon Nanoparticles Derived from Candle Soot. *Angew. Chemie Int. Ed.* **2007**, *46*, 6473–6475.

(47) Lee, J.-S.; Kim, S.-I.; Yoon, J.-C.; Jang, J.-H. Chemical Vapor Deposition of Mesoporous Graphene Nanoballs for Supercapacitor. *ACS Nano* **2013**, *7*, 6047–6055.

(48) Fang, B.; Binder, L. A Modified Activated Carbon Aerogel for High-Energy Storage in Electric Double Layer Capacitors. *J. Power Sources* **2006**, *163*, 616–622.

(49) Lukens, W. W.; Stucky, G. D. Synthesis of Mesoporous Carbon Foams Templated by Organic Colloids. *Chem. Mater.* **2002**, *14*, 1665–1670.

(50) Al-Muhtaseb, S. a.; Ritter, J. a. Preparation and Properties of Resorcinol-Formaldehyde Organic and Carbon Gels. *Adv. Mater.* **2003**, *15*, 101–114.

(51) Fechler, N.; Wohlgemuth, S.-A.; Jäker, P.; Antonietti, M. Salt and Sugar: Direct Synthesis of High Surface Area Carbon Materials at Low Temperatures via Hydrothermal Carbonization of Glucose under Hypersaline Conditions. *J. Mater. Chem. A* **2013**, *1*, 9418.

(52) Wei, L.; Nitta, N.; Yushin, G. Lithographically Patterned Thin Activated Carbon Films as a New Technology Platform for on-Chip Devices. *ACS Nano* **2013**, *7*, 6498–6506.

(53) Chu, W. Dye Removal from Textile Dye Wastewater Using Recycled Alum Sludge. *Water Res.* **2001**, *35*, 3147–3152.

(54) Wang, S.; Li, H.; Xu, L. Application of Zeolite MCM-22 for Basic Dye Removal from Wastewater. *J. Colloid Interface Sci.* **2006**, *295*, 71–78.

(55) Malik, P. K. Dye Removal from Wastewater Using Activated Carbon Developed from Sawdust: Adsorption Equilibrium and Kinetics. *J. Hazard. Mater.* **2004**, *113*, 81–88.

(56) Wang, S.; Li, H.; Xie, S.; Liu, S.; Xu, L. Physical and Chemical Regeneration of Zeolitic Adsorbents for Dye Removal in Wastewater Treatment. *Chemosphere* **2006**, *65*, 82–87.

(57) Crini, G. Non-Conventional Low-Cost Adsorbents for Dye Removal: A Review. *Bioresour. Technol.* **2006**, *97*, 1061–1085.

(58) Tchounwou, P. B.; Patlolla, A. K.; Centeno, J. A. Invited Reviews: Carcinogenic and Systemic Health Effects Associated with Arsenic Exposure—a Critical Review. *Toxicol. Pathol.* **2003**, *31*, 575–588.

(59) Mohan, D.; Pittman Jr., C. U. Arsenic Removal from Water/wastewater Using adsorbents—A Critical Review. *J. Hazard. Mater.* **2007**, *142*, 1–53.

(60) Lemly, A. D. Aquatic Selenium Pollution Is a Global Environmental Safety Issue. *Ecotoxicol. Environ. Saf.* **2004**, *59*, 44–56.

(61) Li, L.; Quinlivan, P. A.; Knappe, D. R. U. Effects of Activated Carbon Surface Chemistry and Pore Structure on the Adsorption of Organic Contaminants from Aqueous Solution. *Carbon* **2002**, *40*, 2085–2100.

(62) Daifullah, A. A. M.; Girgis, B. S. Removal of Some Substituted Phenols by Activated Carbon Obtained from Agricultural Waste. *Water Res.* **1998**, *32*, 1169–1177.

(63) Huang, C. P.; Wu, M. H. The Removal of chromium(VI) from Dilute Aqueous Solution by Activated Carbon. *Water Res.* **1977**, *11*, 673–679.

(64) Monser, L.; Adhoum, N. Modified Activated Carbon for the Removal of Copper, Zinc, Chromium and Cyanide from Wastewater. *Sep. Purif. Technol.* **2002**, *26*, 137–146.

(65) Rivera-Utrilla, J.; Sánchez-Polo, M.; Gómez-Serrano, V.; Álvarez, P. M.; Alvim-Ferraz, M. C. M.; Dias, J. M. Activated Carbon Modifications to Enhance Its Water Treatment Applications. An Overview. *J. Hazard. Mater.* **2011**, *187*, 1–23.

(66) Asadullah, M.; Jahan, I.; Ahmed, M. B.; Adawiyah, P.; Malek, N. H.; Rahman, M. S. Preparation of Microporous Activated Carbon and Its Modification for Arsenic Removal from Water. *J. Ind. Eng. Chem.* **2014**, *20*, 887–896.

(67) Hu, Z.; Lei, L.; Li, Y.; Ni, Y. Chromium Adsorption on High-Performance Activated Carbons from Aqueous Solution. *Sep. Purif. Technol.* **2003**, *31*, 13–18.

(68) Chan, C. One-Dimensional Nanostructured Materials for Li-Ion Battery and Supercapacitor Electrodes. **2009**.

(69) Stoller, M. D.; Ruoff, R. S. Best Practice Methods for Determining an Electrode Material's Performance for Ultracapacitors. *Energy Environ. Sci.* **2010**, *3*, 1294–1301.

(70) Wang, C.; Wang, Y.; Graser, J.; Zhao, R.; Gao, F.; O'Connell, M. J. Solution-Based Carbohydrate Synthesis of Individual Solid, Hollow, and Porous Carbon Nanospheres Using Spray Pyrolysis. *ACS Nano* **2013**, *7*, 11156–11165.

(71) Demaine, E. D.; O'Rourke, J. A Survey of Folding and Unfolding in Computational Geometry. *Comb. Comput. Geom.* **2005**, *52*, 167–211.

(72) Demaine, E. D.; O'Rourke, J. *Geometric Folding Algorithms*; Cambridge university press Cambridge, **2007**.

(73) Stellman, P.; Buchner, T.; Arora, W. J.; Barbastathis, G. Dynamics of Nanostructured Origami. *Microelectromechanical Syst. J.* **2007**, *16*, 932–949.

(74) Landi, B. J.; Raffaelle, R. P.; Heben, M. J.; Alleman, J. L.; VanDerveer, W.; Gennett, T. Single Wall Carbon Nanotube-Nafion Composite Actuators. *Nano Lett.* **2002**, *2*, 1329–1332.

(75) Baughman, R. H.; Cui, C.; Zakhidov, A. A.; Iqbal, Z.; Barisci, J. N.; Spinks, G. M.; Wallace, G. G.; Mazzoldi, A.; De Rossi, D.; Rinzler, A. G.; *et al.* Carbon Nanotube Actuators. *Science* **1999**, *284*, 1340–1344.

(76) Meng, H.; Jinlian Hu. A Brief Review of Stimulus-Active Polymers Responsive to Thermal, Light, Magnetic, Electric, and Water/Solvent Stimuli. *J. Intell. Mater. Syst. Struct.* **2010**, *21*, 859–885.

(77) Liu, Y.; Flood, A. H.; Bonvallet, P. A.; Vignon, S. A.; Northrop, B. H.; Tseng, H. R.; Jeppesen, J. O.; Huang, T. J.; Brough, B.; Baller, M.; *et al.* Linear Artificial Molecular Muscles. *J. Am. Chem. Soc.* **2005**, *127*, 9745–9759.

(78) Juluri, B. K.; Kumar, A. S.; Liu, Y.; Ye, T.; Yang, Y. W.; Flood, A. H.; Fang, L.; Stoddart, J. F.; Weiss, P. S.; Huang, T. J. A Mechanical Actuator Driven Electrochemically by Artificial Molecular Muscles. *ACS Nano* **2009**, *3*, 291–300.

(79) Pelrine, R. High-Speed Electrically Actuated Elastomers with Strain Greater Than 100%. *Science*, **2000**, *287*, 836–839.

(80) Karpelson, M.; Wei, G. Y.; Wood, R. J. Driving High Voltage Piezoelectric Actuators in Microrobotic Applications. *Sensors Actuators, A Phys.* **2012**, *176*, 78–89.

(81) Shepherd, R. F.; Ilievski, F.; Choi, W.; Morin, S. A.; Stokes, A. A.; Mazzeo, A. D.; Chen, X.; Wang, M.; Whitesides, G. M. From the Cover: Multigait Soft Robot. *Proceedings of the National Academy of Sciences*, **2011**, *108*, 20400–20403.

(82) Timoshenko, S. Analysis of Bi-Metal Thermostats. *Journal of the Optical Society of America*, **1925**, *11*, 233.

(83) Riethmuller, W.; Benecke, W. Thermally Excited Silicon Microactuators. *IEEE Trans. Electron Devices* **1988**, *35*, 758–763.

(84) Sellinger, A. T.; Wang, D. H.; Tan, L. S.; Vaia, R. a. Electrothermal Polymer Nanocomposite Actuators. *Adv. Mater.* **2010**, *22*, 3430–3435.

(85) Hu, Y.; Chen, W.; Lu, L.; Liu, J.; Chang, C. Electromechanical Actuation with Controllable Motion Based on a Single-Walled Carbon Nanotube and Natural Biopolymer Composite. *ACS Nano* **2010**, *4*, 3498–3502.

(86) Chen, L.; Liu, C.; Liu, K.; Meng, C.; Hu, C.; Wang, J.; Fan, S. High-Performance, Low-Voltage, and Easy-Operable Bending Actuator Based on Aligned Carbon Nanotube/polymer Composites. *ACS Nano* **2011**, *5*, 1588–1593.

(87) Hawkes, E.; An, B.; Benbernou, N. M.; Tanaka, H.; Kim, S.; Demaine, E. D.; Rus, D.; Wood, R. J. Programmable Matter by Folding. *Proc. Natl. Acad. Sci.* **2010**, *107*, 12441–12445.

(88) Onal, C. D.; Wood, R. J.; Rus, D. An Origami-Inspired Approach to Worm Robots. *IEEE/ASME Trans. Mechatronics* **2013**, *18*, 430–438.

(89) Welch, C. M.; Nekrassova, O.; Compton, R. G. Reduction of Hexavalent Chromium at Solid Electrodes in Acidic Media: Reaction Mechanism and Analytical Applications. *Talanta* **2005**, *65*, 74–80.

(90) Zhang, L.; Xu, C.; Li, B. Simple and Sensitive Detection Method for chromium(VI) in Water Using Glutathione—capped CdTe Quantum Dots as Fluorescent Probes. *Microchim. Acta* **2009**, *166*, 61–68.

(91) JUNG, G. Y.; KIM, Y. S.; LIM, H. B. Simultaneous Determination of Chromium(III) and Chromium(VI) in Aqueous Solution by Capillary Electrophoresis with On-Column UV-VIS Detection. *Anal. Sci.* **1997**, *13*, 463–467.

(92) Posta, J.; Alimonti, A.; Petrucci, F.; Caroli, S. On-Line Separation and Preconcentration of Chromium Species in Seawater. *Anal. Chim. Acta* **1996**, *325*, 185–193.

(93) Zhang, H.; Liu, Q.; Wang, T.; Yun, Z.; Li, G.; Liu, J.; Jiang, G. Facile Preparation of Glutathione-Stabilized Gold Nanoclusters for Selective Determination of Chromium (III) and Chromium (VI) in Environmental Water Samples. *Anal. Chim. Acta* **2013**, *770*, 140–146.

(94) Hallam, P. M.; Kampouris, D. K.; Kadara, R. O.; Banks, C. E. Graphite Screen Printed Electrodes for the Electrochemical Sensing of chromium(VI). *Analyst* **2010**, *135*, 1947–1952.

(95) Jena, B. K.; Raj, C. R. Highly Sensitive and Selective Electrochemical Detection of Sub-Ppb Level chromium(VI) Using Nano-Sized Gold Particle. *Talanta* **2008**, *76*, 161–165.

(96) Jin, W.; Wu, G.; Chen, A. Sensitive and Selective Electrochemical Detection of chromium(VI) Based on Gold Nanoparticle-Decorated Titania Nanotube Arrays. *Analyst* **2014**, *139*, 235–241.

(97) Xu, H.; Zheng, Q.; Yang, P.; Liu, J.; Xing, S.; Jin, L. Electrochemical Synthesis of Silver Nanoparticles-Coated Gold Nanoporous Film Electrode and Its Application to Amperometric Detection for Trace Cr(VI). *Sci. China Chem.* **2011**, *54*, 1004–1010.

(98) Williams, D. B.; Carter, C. B. *The Transmission Electron Microscope*; Springer, **1996**.

(99) Goldstein, J.; Newbury, D. E.; Echlin, P.; Joy, D. C.; Romig Jr, A. D.; Lyman, C. E.; Fiori, C.; Lifshin, E. *Scanning Electron Microscopy and X-Ray Microanalysis: A Text for Biologists, Materials Scientists, and Geologists*; Springer Science & Business Media, **2012**.

(100) Warren, B. E. *X-Ray Diffraction*; Courier Corporation, **1969**.

(101) Watts, J. F. X-Ray Photoelectron Spectroscopy. *Vacuum* **1994**, *45*, 653–671.

(102) Long, D. A. Raman Spectroscopy. *New York* **1977**, 1–12.

(103) Pimenta, M. a; Dresselhaus, G.; Dresselhaus, M. S.; Cançado, L. G.; Jorio, a; Saito, R. Studying Disorder in Graphite-Based Systems by Raman Spectroscopy. *Phys. Chem. Chem. Phys.* **2007**, *9*, 1276–1291.

(104) Malard, L. M.; Pimenta, M. a.; Dresselhaus, G.; Dresselhaus, M. S. Raman Spectroscopy in Graphene. *Phys. Rep.* **2009**, *473*, 51–87.

(105) Ferrari, a. C.; Meyer, J. C.; Scardaci, V.; Casiraghi, C.; Lazzeri, M.; Mauri, F.; Piscanec, S.; Jiang, D.; Novoselov, K. S.; Roth, S.; *et al.* Raman Spectrum of Graphene and Graphene Layers. *Phys. Rev. Lett.* **2006**, *97*, 187401.

(106) Sing, K. S. W.; Everett, D. H.; Haul, R. a. W.; Moscou, L.; Pierotti, R. a.; Rouquérol, J.; Siemieniewska, T. Reporting Physisorption Data for Gas/solid Systems with Special Reference to the Determination of Surface Area and Porosity (Recommendations 1984). *Pure Appl. Chem.* **1985**, *57*, 603–619.

(107) Alhamami, M.; Doan, H.; Cheng, C.-H. A Review on Breathing Behaviors of Metal-Organic-Frameworks (MOFs) for Gas Adsorption. *Materials (Basel).* **2014**, *7*, 3198–3250.

(108) Rouquerol, J.; Rouquerol, F.; Llewellyn, P.; Maurin, G.; Sing, K. S. W. *Adsorption by Powders and Porous Solids: Principles, Methodology and Applications*; Academic press, **2013**.

(109) Brunauer, S.; Emmett, P. H.; Teller, E. Adsorption of Gases in Multimolecular Layers. **1936**, *407*.

(110) Barrett, E. P.; Joyner, L. G.; Halenda, P. P. The Determination of Pore Volume and Area Distributions in Porous Substances. I. Computations from Nitrogen Isotherms. *J. Am. Chem. Soc.* **1951**, *73*, 373–380.

(111) Kruk, M.; Jaroniec, M.; Sayari, A. Application of Large Pore MCM-41 Molecular Sieves To Improve Pore Size Analysis Using Nitrogen Adsorption Measurements. *Langmuir* **1997**, *13*, 6267–6273.

(112) Seaton, N. A.; Walton, J. P. R. B.; quirke, N. A New Analysis Method for the Determination of the Pore Size Distribution of Porous Carbons from Nitrogen Adsorption Measurements. *Carbon* **1989**, *27*, 853–861.

(113) Landers, J.; Gor, G. Y.; Neimark, A. V. Density Functional Theory Methods for Characterization of Porous Materials. *Colloids Surfaces A Physicochem. Eng. Asp.* **2013**, *437*, 3–32.

(114) Ravikovitch, P. I.; Haller, G. L.; Neimark, A. V. Density Functional Theory Model for Calculating Pore Size Distributions: Pore Structure of Nanoporous Catalysts. *Adv. Colloid Interface Sci.* **1998**, *76–77*, 203–226.

(115) Suh, W. H.; Suslick, K. S. Magnetic and Porous Nanospheres from Ultrasonic Spray Pyrolysis. *J. Am. Chem. Soc.* **2005**, *127*, 12007–12010.

(116) Bang, J. H.; Helmich, R. J.; Suslick, K. S. Nanostructured ZnS:Ni 2+ Photocatalysts Prepared by Ultrasonic Spray Pyrolysis. *Adv. Mater.* **2008**, *20*, 2599–2603.

(117) Okuyama, K.; Wuled Lenggoro, I. Preparation of Nanoparticles via Spray Route. *Chem. Eng. Sci.* **2003**, *58*, 537–547.

(118) Jin, Y. Z.; Gao, C.; Hsu, W. K.; Zhu, Y.; Huczko, A.; Bystrzejewski, M.; Roe, M.; Lee, C. Y.; Acquah, S.; Kroto, H.; *et al.* Large-Scale Synthesis and Characterization of Carbon Spheres Prepared by Direct Pyrolysis of Hydrocarbons. *Carbon* **2005**, *43*, 1944–1953.

(119) Chen, H.-K. Kinetic Study on the Carbothermic Reduction of Zinc Oxide. *Scand. J. Metall.* **2001**, *30*, 292–296.

(120) Qiu, J.; Li, Y.; Wang, Y.; Liang, C.; Wang, T.; Wang, D. A Novel Form of Carbon Micro-Balls from Coal. *Carbon* **2003**, *41*, 767–772.

(121) Qian, J.; Pantea, C.; Huang, J.; Zerda, T. W.; Zhao, Y. Graphitization of Diamond Powders of Different Sizes at High Pressure–high Temperature. *Carbon* **2004**, *42*, 2691–2697.

(122) Jawhari, T.; Roid, A.; Casado, J. Raman Spectroscopic Characterization of Some Commercially Available Carbon Black Materials. *Carbon* **1995**, *33*, 1561–1565.

(123) Hanigan, D.; Zhang, J.; Herckes, P.; Krasner, S. W.; Chen, C.; Westerhoff, P. Adsorption of N-Nitrosodimethylamine Precursors by Powdered and Granular Activated Carbon. *Environ. Sci. Technol.* **2012**, *46*, 12630–12639.

(124) Sing, K. S. W. Reporting Physisorption Data for Gas/solid Systems with Special Reference to the Determination of Surface Area and Porosity (Recommendations 1984). *Pure Appl. Chem.* **1985**, *57*, 603–619.

(125) Corapcioglu, M. O.; Huang, C. P. The Surface Acidity and Characterization of Some Commercial Activated Carbons. *Carbon* **1987**, *25*, 569–578.

(126) Chingombe, P.; Saha, B.; Wakeman, R. J. Surface Modification and Characterisation of a Coal-Based Activated Carbon. *Carbon* **2005**, *43*, 3132–3143.

(127) Torres, J.; Pintos, V.; Dom ńguez, S.; Kremer, C.; Kremer, E. Selenite and Selenate Speciation in Natural Waters: Interaction with Divalent Metal Ions. *J. Solution Chem.* **2010**, *39*, 1–10.

(128) Hu, J.; Chen, C.; Zhu, X.; Wang, X. Removal of Chromium from Aqueous Solution by Using Oxidized Multiwalled Carbon Nanotubes. *J. Hazard. Mater.* **2009**, *162*, 1542–1550.

(129) Mandich, N. V; Lalvani, S. B.; Wiltkowski, T.; Lalvani, L. S. Selective Removal of Chromate Anion by a New Carbon Adsorbent. *Met. Finish.* **1998**, *96*, 39–44.

(130) Eguez, H.; Cho, E. Adsorption of Arsenic on Activated Charcoal. *JOM* **1987**, *39*, 38–41.

(131) Lorenzen, L.; van Deventer, J. S. J.; Landi, W. M. Factors Affecting the Mechanism of the Adsorption of Arsenic Species on Activated Carbon. *Miner. Eng.* **1995**, *8*, 557–569.

(132) Goh, K.-H.; Lim, T.-T. Geochemistry of Inorganic Arsenic and Selenium in a Tropical Soil: Effect of Reaction Time, pH, and Competitive Anions on Arsenic and Selenium Adsorption. *Chemosphere* **2004**, *55*, 849–859.

(133) Gonzalez, C. M.; Hernandez, J.; Parsons, J. G.; Gardea-Torresdey, J. L. A Study of the Removal of Selenite and Selenate from Aqueous Solutions Using a Magnetic Iron/manganese Oxide Nanomaterial and ICP-MS. *Microchem. J.* **2010**, *96*, 324–329.

(134) Jegadeesan, G.; Mondal, K.; Lalvani. Selenate Removal from Sulfate Containing Aqueous Solutions. *Environ. Technol.* **2005**, *26*, 1181–1188.

(135) Zhang, L. L.; Zhao, X. S. Carbon-Based Materials as Supercapacitor Electrodes. *Chem. Soc. Rev.* **2009**, *38*, 2520–2531.

(136) Wang, Y.; Shi, Z.; Huang, Y.; Ma, Y.; Wang, C.; Chen, M.; Chen, Y. Supercapacitor Devices Based on Graphene Materials. *J. Phys. Chem. C* **2009**, *113*, 13103–13107.

(137) Ferrari, A. C.; Meyer, J. C.; Scardaci, V.; Casiraghi, C.; Lazzeri, M.; Mauri, F.; Piscanec, S.; Jiang, D.; Novoselov, K. S.; Roth, S.; *et al.* Raman Spectrum of Graphene and Graphene Layers. *Phys. Rev. Lett.* **2006**, *97*, 187401.

(138) Sano, N.; Wang, H.; Chhowalla, M.; Alexandrou, I.; Amaratunga, G. A. J. Nanotechnology: Synthesis of Carbon “Onions” in Water. *Nature* **2001**, *414*, 506–507.

(139) Pech, D.; Brunet, M.; Durou, H.; Huang, P.; Mochalin, V.; Gogotsi, Y.; Taberna, P.-L.; Simon, P. Ultrahigh-Power Micrometre-Sized Supercapacitors Based on Onion-like Carbon. *Nat Nano* **2010**, *5*, 651–654.

(140) Endo, M.; Nishimura, Y.; Takahashi, T.; Takeuchi, K.; Dresselhaus, M. S. Lithium Storage Behavior for Various Kinds of Carbon Anodes in Li Ion Secondary Battery. *J. Phys. Chem. Solids* **1996**, *57*, 725–728.

(141) Zheng, T.; Dahn, J. R. The Effect of Turbostratic Disorder on the Staging Transitions in Lithium Intercalated Graphite. *Synth. Met.* **1995**, *73*, 1–7.

(142) Fujimoto, H. Development of Efficient Carbon Anode Material for a High-Power and Long-Life Lithium Ion Battery. *J. Power Sources* **2010**, *195*, 5019–5024.

(143) Han, F. D.; Yao, B.; Bai, Y. J. Preparation of Carbon Nano-Onions and Their Application as Anode Materials for Rechargeable Lithium-Ion Batteries. *J. Phys. Chem. C* **2011**, *115*, 8923–8927.

(144) Han, F.-D.; Bai, Y.-J.; Liu, R.; Yao, B.; Qi, Y.-X.; Lun, N.; Zhang, J.-X. Template-Free Synthesis of Interconnected Hollow Carbon Nanospheres for High-Performance Anode Material in Lithium-Ion Batteries. *Adv. Energy Mater.* **2011**, *1*, 798–801.

(145) Wang, Q.; Sun, X.; He, D.; Zhang, J. Preparation and Study of Carbon Nano-Onion for Lithium Storage. *Mater. Chem. Phys.* **2013**, *139*, 333–337.

(146) Tian, W.-Q.; Wu, X.-Y.; Wang, K.-X.; Jiang, Y.-M.; Wang, J.-F.; Chen, J.-S. Hierarchical Porous Carbon Spheres as an Anode Material for Lithium Ion Batteries. *RSC Adv.* **2013**, *3*, 10823–10827.

(147) Lee, K. T.; Lytle, J. C.; Ergang, N. S.; Oh, S. M.; Stein, A. Synthesis and Rate Performance of Monolithic Macroporous Carbon Electrodes for Lithium-Ion Secondary Batteries. *Adv. Funct. Mater.* **2005**, *15*, 547–556.

(148) Wang, H.; Abe, T.; Maruyama, S.; Iriyama, Y.; Ogumi, Z.; Yoshikawa, K. Graphitized Carbon Nanobeads with an Onion Texture as a Lithium-Ion Battery Negative Electrode for High-Rate Use. *Adv. Mater.* **2005**, *17*, 2857–2860.

(149) Wang, Q.; Li, H.; Chen, L.; Huang, X. Novel Spherical Microporous Carbon as Anode Material for Li-Ion Batteries. *Solid State Ionics* **2002**, *152–153*, 43–50.

(150) Buqa, H.; Goers, D.; Holzapfel, M.; Spahr, M. E.; Novák, P. High Rate Capability of Graphite Negative Electrodes for Lithium-Ion Batteries. *J. Electrochem. Soc.* **2005**, *152*, A474.

(151) Fujimoto, H.; Tokumitsu, K.; Mabuchi, A.; Chinnasamy, N.; Kasuh, T. The Anode Performance of the Hard Carbon for the Lithium Ion Battery Derived from the Oxygen-Containing Aromatic Precursors. *J. Power Sources* **2010**, *195*, 7452–7456.

(152) Zheng, T.; Xing, W.; Dahn, J. R. Carbons Prepared from Coals for Anodes of Lithium-Ion Cells. *Carbon* **1996**, *34*, 1501–1507.

(153) Ren, Z. F.; Huang, Z. P.; Xu, J. W.; Wang, J. H.; Bush, P.; Siegal, M. P.; Provencio, P. N. Synthesis of Large Arrays of Well-Aligned Carbon Nanotubes on Glass. *Science* **1998**, *282*, 1105–1107.

(154) Iijima, S.; Ichihashi, T. Single-Shell Carbon Nanotubes of 1-Nm Diameter. *Nature* **1993**, *363*, 603–605.

(155) Armandi, M.; Bonelli, B.; Geobaldo, F.; Garrone, E. Nanoporous Carbon Materials Obtained by Sucrose Carbonization in the Presence of KOH. *Microporous Mesoporous Mater.* **2010**, *132*, 414–420.

(156) Ravikovitch, P. I.; Neimark, A. V. Characterization of Nanoporous Materials from Adsorption and Desorption Isotherms. *Colloids Surfaces A Physicochem. Eng. Asp.* **2001**, *187-188*, 11–21.

(157) Liu, B.; Shioyama, H.; Jiang, H.; Zhang, X.; Xu, Q. Metal-Organic Framework (MOF) as a Template for Syntheses of Nanoporous Carbons as Electrode Materials for Supercapacitor. *Carbon* **2010**, *48*, 456–463.

(158) Ruiz, V.; Blanco, C.; Raymundo-Piñero, E.; Khomenko, V.; Béguin, F.; Santamaría, R. Effects of Thermal Treatment of Activated Carbon on the Electrochemical Behaviour in Supercapacitors. *Electrochim. Acta* **2007**, *52*, 4969–4973.

(159) Adinaveen, T.; John Kennedy, L.; Judith Vijaya, J.; Sekaran, G. Surface and Porous Characterization of Activated Carbon Prepared from Pyrolysis of Biomass (rice Straw) by Two-Stage Procedure and Its Applications in Supercapacitor Electrodes. *J. Mater. Cycles Waste Manag.* **2014**, 1–12.

(160) Sánchez-González, J.; Stoeckli, F.; Centeno, T. A. The Role of the Electric Conductivity of Carbons in the Electrochemical Capacitor Performance. *J. Electroanal. Chem.* **2011**, *657*, 176–180.

(161) Pandolfo, a. G.; Hollenkamp, a. F. Carbon Properties and Their Role in Supercapacitors. *J. Power Sources* **2006**, *157*, 11–27.

(162) Kennedy, L. J.; Vijaya, J. J.; Sekaran, G. Electrical Conductivity Study of Porous Carbon Composite Derived from Rice Husk. *Mater. Chem. Phys.* **2005**, *91*, 471–476.

(163) Darmstadt, H.; Roy, C.; Kaliaguine, S.; Choi, S. .; Ryoo, R. Surface Chemistry of Ordered Mesoporous Carbons. *Carbon* **2002**, *40*, 2673–2683.

(164) Zhao, L.; Fan, L.-Z.; Zhou, M.-Q.; Guan, H.; Qiao, S.; Antonietti, M.; Titirici, M.-M. Nitrogen-Containing Hydrothermal Carbons with Superior Performance in Supercapacitors. *Adv. Mater.* **2010**, *22*, 5202–5206.

(165) Dresselhaus, M. S.; Dresselhaus, G.; Charlier, J. C.; Hernández, E. Electronic, Thermal and Mechanical Properties of Carbon Nanotubes. *Philos. Trans. A. Math. Phys. Eng. Sci.* **2004**, *362*, 2065–2098.

(166) Shahinpoor, M.; Bar-Cohen, Y.; Simpson, J. O.; Smith, J. Ionic Polymer-Metal Composites (IPMCs) as Biomimetic Sensors, Actuators and Artificial Muscles-a Review. *Smart Mater. Struct.* **1998**, *7*, R15.

(167) Kataura, H.; Kumazawa, Y.; Maniwa, Y.; Umezu, I.; Suzuki, S.; Ohtsuka, Y.; Achiba, Y. Optical Properties of Single-Wall Carbon Nanotubes. *Synth. Met.* **1999**, *103*, 2555–2558.

(168) Wu, Z.; Chen, Z.; Du, X.; Logan, J. M.; Sippel, J.; Nikolou, M.; Kamaras, K.; Reynolds, J. R.; Tanner, D. B.; Hebard, A. F.; *et al.* Transparent, Conductive Carbon Nanotube Films. *Science* **2004**, *305*, 1273–1276.

(169) Rinzler, A. G.; Liu, J.; Dai, H.; Nikolaev, P.; Huffman, C. B.; Rodriguez-Macias, F. J.; Boul, P. J.; Lu, A. H.; Heymann, D.; Colbert, D. T.; *et al.* Large-Scale Purification of Single-Wall Carbon Nanotubes: Process, Product, and Characterization. *Applied Physics A: Materials Science & Processing*, 1998, *67*, 29–37.

(170) O'Connell, M. J.; Boul, P.; Ericson, L. M.; Huffman, C.; Wang, Y.; Haroz, E.; Kuper, C.; Tour, J.; Ausman, K. D.; Smalley, R. E. Reversible Water-Solubilization of Single-Walled Carbon Nanotubes by Polymer Wrapping. *Chem. Phys. Lett.* **2001**, *342*, 265–271.

(171) O'Connell, M. J.; Bachilo, S. M.; Huffman, C. B.; Moore, V. C.; Strano, M. S.; Haroz, E. H.; Rialon, K. L.; Boul, P. J.; Noon, W. H.; Kittrell, C.; *et al.* Band Gap Fluorescence from Individual Single-Walled Carbon Nanotubes. *Science* **2002**, *297*, 593–596.

(172) Kim, J.; Kang, Y.; Yun, S. Blocked Force Measurement of Electro-Active Paper Actuator by Micro-Balance. *Sensors Actuators, A Phys.* **2007**, *133*, 401–406.

(173) Chalopin, Y.; Volz, S.; Mingo, N. Upper Bound to the Thermal Conductivity of Carbon Nanotube Pellets. *J. Appl. Phys.* **2009**, *105*.

(174) Prasher, R. S.; Hu, X. J.; Chalopin, Y.; Mingo, N.; Lofgreen, K.; Volz, S.; Cleri, F.; Keblinski, P. Turning Carbon Nanotubes from Exceptional Heat Conductors into Insulators. *Phys. Rev. Lett.* **2009**, *102*.

(175) Jiang, H.; Liu, B.; Huang, Y.; Hwang, K. C. Thermal Expansion of Single Wall Carbon Nanotubes. *J. Eng. Mater. Technol.* **2004**, *126*, 265–270.

(176) Maniwa, Y.; Fujiwara, R.; Kira, H.; Tou, H.; Kataura, H.; Suzuki, S.; Achiba, Y.; Nishibori, E.; Takata, M.; Sakata, M.; *et al.* Thermal Expansion of Single-Walled Carbon nanotube(SWNT) Bundles : X-Ray Diffraction Studies. *Phys. Rev. B* **2001**, *64*, 10–12.

(177) Lendlein, A.; Kelch, S. Shape-Memory Polymers. *Angew. Chemie Int. Ed.* **2002**, *41*, 2034–2057.

(178) Otero, T. F. Reactive Conducting Polymers as Actuating Sensors and Tactile Muscles. *Bioinspir. Biomim.* **2008**, *3*, 035004.

(179) Xiao, L.; Chen, Z.; Feng, C.; Liu, L.; Bai, Z. Q.; Wang, Y.; Qian, L.; Zhang, Y.; Li, Q.; Jiang, K.; *et al.* Flexible, Stretchable, Transparent Carbon Nanotube Thin Film Loudspeakers. *Nano Lett.* **2008**, *8*, 4539–4545.

(180) Lu, S.; Panchapakesan, B. Optically Driven Nanotube Actuators. *Nanotechnology*, 2005, *16*, 2548–2554.

(181) Kim, B.; Kim, D.-H.; Jung, J.; Park, J.-O. A Biomimetic Undulatory Tadpole Robot Using Ionic Polymer–metal Composite Actuators. *Smart Mater. Struct.* **2005**, *14*, 1579.

(182) Shahinpoor, M.; Kim, K. J. Ionic Polymer-Metal Composites: I. Fundamentals. *Smart Mater. Struct.* **2001**, *10*, 819.

(183) Sutar, D.; Aswal, D. K.; Gupta, S. K.; Yakhmi, J. V. Electrochemical Actuator from Conductive Electroactive Polymer Polypyrrole Deposited on Gold. *Indian J. Pure Appl. Phys.* **2007**, *45*, 354–357.

(184) Lang, X.; Hirata, A.; Fujita, T.; Chen, M. Nanoporous Metal/oxide Hybrid Electrodes for Electrochemical Supercapacitors. *Nat. Nanotechnol.* **2011**, *6*, 232–236.

(185) Jiang, H.; Li, C.; Sun, T.; Ma, J. High-Performance Supercapacitor Material Based on Ni(OH)2 Nanowire-MnO2 Nanoflakes Core–shell Nanostructures. *Chem. Commun.* **2012**, *48*, 2606.

(186) Wei, W.; Cui, X.; Chen, W.; Ivey, D. G. Manganese Oxide-Based Materials as Electrochemical Supercapacitor Electrodes. *Chem. Soc. Rev.* **2011**, *40*, 1697–1721.

(187) Xu, C.; Shin, P.; Cao, L.; Gao, D. Preferential Growth of Long ZnO Nanowire Array and Its Application in Dye-Sensitized Solar Cells. *J. Phys. Chem. C* **2009**, *114*, 125–129.

(188) Greene, L. E.; Law, M.; Goldberger, J.; Kim, F.; Johnson, J. C.; Zhang, Y.; Saykally, R. J.; Yang, P. Low-temperature Wafer-scale Production of ZnO Nanowire Arrays. *Angew. Chemie Int. Ed.* **2003**, *42*, 3031–3034.

(189) Hu, L.; Chen, W.; Xie, X.; Liu, N.; Yang, Y.; Wu, H.; Yao, Y.; Pasta, M.; Alshareef, H. N.; Cui, Y. Symmetrical MnO2–carbon Nanotube–textile Nanostructures for Wearable Pseudocapacitors with High Mass Loading. *ACS Nano* **2011**, *5*, 8904–8913.

(190) Niekerk, W. Van; Lachmann, G.; Eldik, R. Van; Hamza, M. A Kinetic and Mechanistic Study of the Chromium (VI) Reduction by Hydrogen Peroxide in Acidic Aqueous Solutions. *Water SA* **2007**, *33*, 619–626.